

# **NERC Scientific Facilities and Technology Ion Microprobe Facility**



**University of Edinburgh  
NERC Ion Microprobe Facility**

**2012 Annual Science Report**

Ion Microprobe Facility  
School of Geosciences  
Kings Buildings  
West Mains Road  
Edinburgh  
EH9 3JW

<http://www.geos.ed.ac.uk/facilities/>



## Contents

### Ion Microprobe Projects

No	Authors	Project Title	p.
1	T. Dunkley Jones, K. Prentice	Surface ocean productivity through the Eocene/Oligocene transition using the Sr/Ca composition of coccolith calcite	1
2	L.C. Foster, F. Ragazzola, M. Wall, A. Foram & D.N Schmidt	$\delta^{11}\text{B}$ analysis of <i>Lophelia pertusa</i> cultured under high $\text{CO}_2$	3
3	M. Fowler, E. Bruand & C. Storey	Accessory minerals and the evolution of plate tectonics: opening the archive	5
4	M.E. Hartley, J. Maclennan, M. Edmonds, D.J. Morgan & T. Thordarson	Laki revisited: New quantitative constraints on deep degassing prior to large basaltic fissure eruptions	7
5	M. Hiscock & G. Bromiley	Diffusion of volatiles in Earth's mantle – Is it all about grain boundaries?	9
6	M.E. Hodson, E.A.A. Versteegh, S. Black, P.F. Schofield, M.R. Lee	Constructing a new terrestrial palaeo-environment thermometer - earthworm secreted calcite granules	11
7	M.C.S. Humphreys & R. Brooker	Volatiles and Fe oxidation state in hydrous rhyolite	13
8	E.S. Jennings, S.A. Gibson, J. Maclennan	Compositional heterogeneity of the Earth's mantle: constraints from olivine-hosted melt inclusions from a continental flood basalt setting	15
9	R.Jones, L.Kirstein, R.Hinton, S.Kasemann, & T.Elliott	Cenozoic arc magmatism along the active Andean margin	17
10	A. Kaye (now: de Joux), T.Thordarson, M.Denny, R.Hinton & A.J. de Joux	U-Pb dating of the felsic and intermediate volcanic sequence of the nickelsulphide bearing Cosmos succession, Agnew-Wiluna greenstone belt, Yilgarn Craton, Western Australia	19
11	T. Kobayashi, S. L. Harley, Y. Hiroi & T. Hirajima	Metamorphic history of garnet-rich gneiss in Moldanubian Zone of the southern Bohemian Massif, inferred from inclusions and compositional zoning of garnet	21
12	C.J. Lissenberg	The evolution of mid-ocean ridge magma chambers and the growth of slowspreading oceanic crust	23
13	E. Llewellyn, I. McIntosh, M. Humphreys, A. Burgisser & C.I. Schipper	Quantifying the dynamics of bubble growth in magma using SIMS profiling of water content in glass	25
14	E.A. McMillan & P. Bonnand	Organogenic dolomite and Neoproterozoic chemostratigraphy	27
15	Andrew Miles, Colin Graham, Martin Gillespie, Chris Hawkesworth and Richard Hinton	The hydrothermal history of British Devonian granites: Insights from zircon, quartz and whole-rock oxygen isotope compositions	29

16	Yves Moussallam,, Clive Oppenheimer,, Bruno Scaillet, Phil Kyle	Megacrysts and conduit dynamics at Erebus volcano	31
17	D. D. Muir, J. D. Blundy & A. C. Rust	Constraining magma storage conditions at Uturuncu volcano, SW Bolivia	33
18	D.A. Neave, J. Maclennan, M. Edmonds & T. Thordarson	Skuggafjöll: A window into deep crystallisation, degassing and mixing in the Eastern Volcanic Zone of Iceland	37
19	G. Pennacchioni, G. D. Bromiley & F. Nestola	Constraining shear heating in mylonites using the Ti in quartz geothermometer	39
20	M.K. Reichow, T.R. Knott, & M.J. Branney	Timing and sources of voluminous low- $\delta^{18}\text{O}$ rhyolite magmas in the Snake River (Columbia River-Yellowstone LIP), USA: a combined oxygen isotope and U/Pb dating study on zircon	41
21	J. Riker, J. Blundy & A. Rust	Interpreting degassing paths in crystallising magmas: constraints from experiments on Mount St. Helens rhyodacite	43
22	S. Skora, J. Blundy & L. Carter,	Melting of natural MORB at subduction zone conditions	45
23	C.C.Stamper, J.D.Blundy, E.Melekhova & R.J.Arculus	Magma storage and differentiation beneath Grenada (Lesser Antilles)	47
24	A. Thomson, M. Walter, S. Kohn, G. Bulanova, C. Smith & D. Araujo	Superdeep diamonds preserve record of ancient carbon subduction	49
25	D.Thorpe & R. Wood	Quantifying the dynamics of calcite cement growth with oil emplacement and the evolution of pore chemistry	51
26	J.R. Wheeley, M.P. Smith, & I. Boomer	Constraining conodont $\delta^{18}\text{O}$ for Palaeozoic marine palaeothermometry	53

# Surface ocean productivity through the Eocene/Oligocene transition using the Sr/Ca composition of coccolith calcite

Tom Dunkley Jones<sup>1</sup>, Katy Prentice<sup>2</sup>

<sup>1</sup>School of Geography, Earth and Environmental Sciences, University of Birmingham, B15 2TT, UK

<sup>2</sup>Department of Earth Science and Engineering, Imperial College, London, SW7 2AZ, UK

## Rationale

The Eocene/Oligocene transition (E/OT; ~34 Ma) is the largest climate transition of the past 65 million years. In less than 500 kyr Antarctic ice sheets grew to continental extent for the first time in the Cenozoic. This climate transition had major impacts on the marine carbon cycle, patterns of surface ocean nutrient distribution and biological productivity, which may, in turn, have led to a series of extinctions in the calcareous phyto- and zooplankton.

Here, we used a novel geochemical approach, the measurement of Sr/Ca ratios of fossil coccoliths using Secondary Ionization Mass Spectroscopy (SIMS), as a direct means of quantifying changes in surface-water nutrient availability at the time of coccolith formation. This study focused on coccolith material recovered through the E/OT from Integrated Ocean Drilling Program (IODP) Expedition 320 in the equatorial Pacific. This region has been an upwelling zone of planetary importance throughout the Cenozoic and has yielded the most detailed climate records of the E/OT available to date.

## Methods

Samples were taken from IODP Expedition 320 (March-May 2009) across the E/OT from IODP Site U1334 (present location 8.0°N 132.0°W), across the interval ~305 to 290m CCSF-A, equivalent in time to ~34.6 to 33.4 Ma. This site is reconstructed to be at ~1°N during the E/OT, beneath or close to the zone of peak equatorial upwelling. Prior to SIMS analysis, samples were prepared using the microfiltration technique. Once prepared, sub-samples of the coccolith size-fractions were taken for SEM and light microscope observation to assess their taxonomic composition at the species level. Appropriate size splits were then chosen for SIMS analysis, diluted in distilled water and flooded onto indium coated ion probe stubs. Stubs were then gold coated and subjected to SEM examination to locate, identify and image individual nannofossil specimens suitable for SIMS analysis. Microprobe analyses were undertaken during June 2012 at the NERC Ion Microprobe Facility at Edinburgh University, which built upon and extended analyses undertaken in November 2011. Analyses targeted five key species (*Coccolithus pelagicus*, *Coccolithus formosus*, *Discoaster tanii*, *Reticulofenestra bisecta* and *Reticulofenestra dictyoda*) with between 5 and 15 individual coccoliths analyzed from within each sample interval. Trace element distributions, especially Mg and Al, were monitored on and around the specimen during analysis to check for clay contamination.

## Results

The greater number of specimens analysed from key species across the E/O transition has allowed us to interpret the fossil coccolith data more rigorously and begin to undertake informative comparisons with Sr/Ca ratios of modern cultured coccoliths (Figures 1 & 2; Bown et al. in prep; Prentice et al. in prep). First, it is now clear that, as with the modern cultured coccoliths, where primary fossil coccolith calcite is being analysed as opposed to diagenetic overgrowths, it is characterised by very low Mg/Ca ratios. Occasionally, during analysis cycles, a drift in values occurred with a decline in Mg/Ca and increase in Sr/Ca ratios through the analysis cycles (Figure 1). Plotting the path of these analysis cycles in Sr/Ca versus Mg/Ca space and with data from cultured placoliths, clearly show that “clean” fossil samples are located in the same low Mg/Ca space as modern specimens, whereas overgrown samples track back to these values as analysis progresses (Figure 1).

The second advance of the extra data collected is the more robust plotting of the Sr/Ca values for given species – i.e. mapping out the biological, species-specific patterns of Sr/Ca ratios in this fossil material. This is a first step towards understanding the species-specific “vital effects” on fossil coccolith Sr/Ca (Figure 2). From this extended dataset it is also clear that the great majority of fossil coccolith calcite from the E/O transition has Mg/Ca ratios of less than 1 mmol mol<sup>-1</sup> (Figure 2).

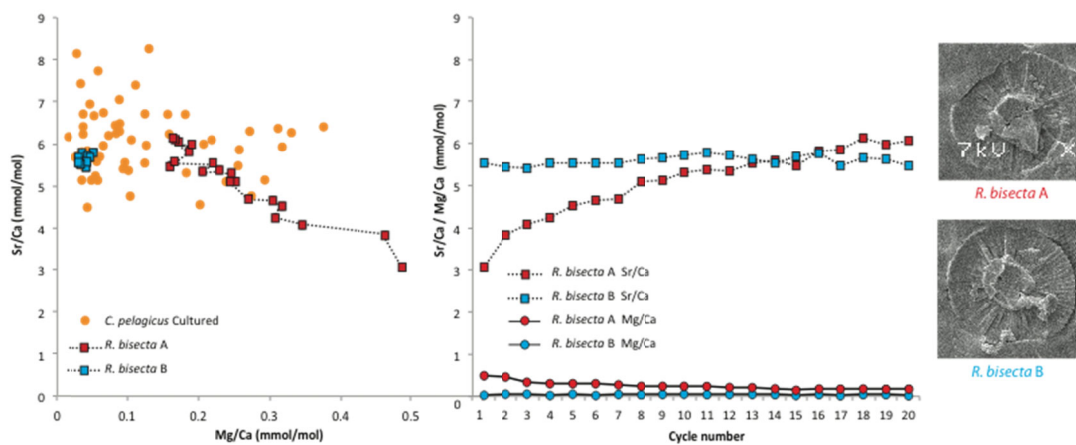


**Figure 1:** Sr/Ca and Mg/Ca ratios for two fossil coccoliths of *Reticulofenestra bisecta* showing changes in trace element concentrations through twenty analysis cycles. Sr/Ca versus Mg/Ca (left) and with cycle number (centre). SEMs of specimens analysed also shown (right). For slightly overgrown specimen (A) Mg/Ca values start relatively high and then decline during the analysis, until at the end values are within the population of Sr/Ca – Mg/Ca values determined for a population of modern culture *Coccolithus pelagicus* (left).

### Further Work

Coccolith Sr/Ca data collected to date provide a unique record of coccolith Sr/Ca variability across the E/O transition. These data are the main focus of Katy Prentice's PhD studies (Sept. 2011 – 2014). They will be published together with fine fraction bulk trace element (Sr/Ca) analyses that are currently underway by ICP-OES.

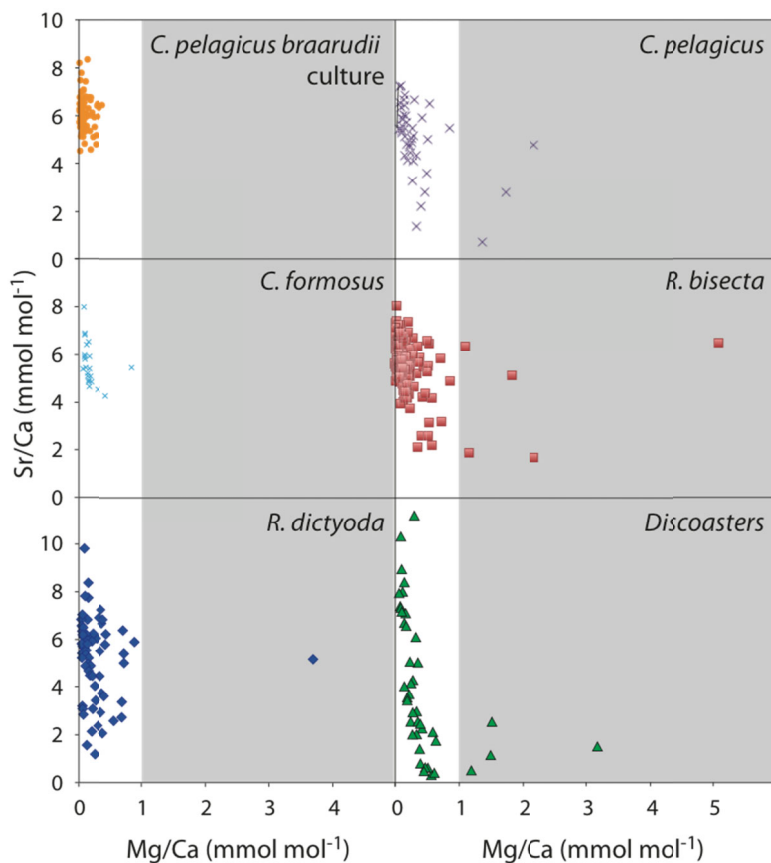


**Figure 2.** Sr/Ca versus Mg/Ca ratios for the five key fossil taxa analysed across the E/O transition and cultured specimens of *Coccolithus pelagicus braarudii* (culture data from Bown et al. in prep). Distinct species show subtly different Sr/Ca ranges, most notably the large range of values observed for specimens of *Discoaster*. Also notable is that fossil specimens show lower values of Sr/Ca ( $<4 \text{ mmol mol}^{-1}$ ) than culture specimens that were not subject to nutrient limitation.

# $\delta^{11}\text{B}$ analysis of *Lophelia pertusa* cultured under high $\text{CO}_2$

L.C. Foster<sup>1</sup>, F. Ragazzola<sup>1</sup>, M. Wall<sup>2,3</sup>, A. Foram<sup>2</sup> & D.N Schmidt<sup>1</sup>

<sup>1</sup>Department of Earth Sciences, University of Bristol, UK

<sup>2</sup>Helmholtz Centre for Ocean Research Kiel (Geomar), Germany

<sup>3</sup>Helmholtz Alfred Wegener Institute for Polar and Marine Research, Bremerhaven, Germany

## Project background

The modern ocean is absorbing  $\text{CO}_2$  from anthropogenic emissions resulting in a drop in carbonate saturation and ocean pH. Cold waters take up and store more  $\text{CO}_2$  and thus the high latitudes will be amongst the first to experience undersaturated conditions [1]. Cold water corals are important habitat formers in deep-water ecosystems and at high latitudes, with *Lophelia pertusa* being the most common species of cold water corals. The impact of changes in seawater saturation have however been found to be less than predicted, with *L. pertusa* able to sustain growth even in undersaturated conditions [2]. However, it is important to know whether such acclimatisation modifies the skeleton and thus its effect ecosystem functionality. By using specimens cultured under known laboratory conditions under elevated  $\text{CO}_2$ , we can examine the potential impact of high  $\text{CO}_2$  on *L. pertusa*. We analysed  $\delta^{11}\text{B}$  by Secondary Ionisation Mass Spectrometry (SIMS) to determine if there is any change the recorded pH.

## Samples

We analysed two *L. pertusa* samples to examine  $\delta^{11}\text{B}$  variability within natural growth and under that cultured under high  $\text{CO}_2$  (605  $\mu\text{atm}$ ). Analyses were performed using Cameca-ims-1270. The sections were gold-coated with  $\text{O}_2^-$  primary beam were used with a primary beam energy of 12.2 keV and secondary ion energy of 10keV. The net primary impact energy was 22 keV. The beam diameter at the end of the analysis was ~25 by 40  $\mu\text{m}$ .

## Results

Material which was deposited along the same growth band has the same  $\delta^{11}\text{B}$  but there is a large degree of heterogeneity in  $\delta^{11}\text{B}$  with the naturally grown coral branch varying from ~20.5-29‰ with a mean of  $25.4 \pm 2.8\%$  (1SD) with the lowest values occurring at the Early Mineralized Zone. When the  $\delta^{11}\text{B}$ -pH proxy is applied, reconstructed pH is elevated compared to the ambient seawater pH. While the degree of heterogeneity with respect to boron isotopes in our samples is roughly equivalent to that of [3] and the absolute values disagree with an offset of ~10‰. It is important to note that our data agrees well with the bulk measurements of [4] done by TIMS (Thermal Ionization Mass Spectrometer).

## Further work

Our data will be combined with existing Synchrotron X-Ray Tomography and Raman data to examine for changes in skeleton morphology and skeletal fiber orientation associated with changes in  $\delta^{11}\text{B}$ .

## References

- [1] J. C. Orr et al. (2005) Nature **437(7059)**, 681-686.
- [2] A. U. Form and U. Riebesell (2012) Global Change Biology **18(3)**, 843-853.
- [3] D. Blamart et al. (2007) Geochemistry, Geophysics, Geosystems **8**, Q12001.
- [4] M. McCulloch et al. (2012) Geochimica et Cosmochimica Acta **87**, 21-34.

PAGE INTENTIONALLY LEFT BLANK

# Accessory minerals and the evolution of plate tectonics: opening the archive

M. Fowler, E. Bruand & C. Storey

<sup>1</sup>School of Earth and Environmental Sciences, University of Portsmouth, Burnaby Building, Burnaby Road, Portsmouth PO1 3QL

## Introduction

Sanukitoids represent a key marker in the evolution of plate tectonics, since their genesis in the Neoproterozoic is understood to signal the initiation of a supra-subduction mantle wedge. The precursors of sanukitoids are Archaean TTG (tonalite-trondhjemite-granodiorite) magmas, and their successors in modern tectonic regime are BADR (basalt-andesite-dacite-rhyolite) plus intrusive equivalents. Phanerozoic high Ba-Sr granites such as those of the Caledonian province in northern Britain have recently been recognised as modern equivalents of sanukitoids [1]. The purpose of the EIMF analytical work was to test this comparison further, and begin the characterisation of sanukitoid accessory minerals in rocks that have not been affected by later reworking, such that they might be recognised in the detrital heavy mineral record and thus be used to constrain sanukitoid generation through geological time. The specific petrogenetic hypothesis to be tested was “that there are small but variable sedimentary contributions to the parental magmas of high Ba-Sr granites and sanukitoids”, using a combination of oxygen isotopes (EIMF) and Hf isotopes (University of Southampton), plus complementary data on trace elements and other radiogenic isotope systems analysed at Portsmouth and elsewhere.

## Results

**Oxygen Isotopes.** Figure 1 (a and b) shows the zircon oxygen data for the high Ba-Sr suite, alongside comparative published data for sanukitoids and associated rocks from Finland [2]. In both high Ba-Sr plutons (Strontian and Rogart, thought to be from depleted and enriched sources respectively) there is a clear maximum between  $\delta^{18}\text{O} +5.5$  and  $+6.5\%$ , with a very few analyses below this range and several  $> +7.5\%$  in the Rogart dataset, corresponding to xenocrystic cores. This completely overlaps the published sanukitoid data (Fig. 1), and is therefore consistent with the petrogenetic comparison established on the basis of whole-rock elemental and isotopic data [3]. A substantial dataset of  $\delta^{18}\text{O}$  values in titanite and apatite has been assembled. Figure 1 (c and d) shows that titanite data form a well-constrained distribution centred on  $+5.5\%$ , whereas apatite data hint at bimodality, with the major peak at  $+5.5\%$  but a smaller one in excess of  $+10\%$ .

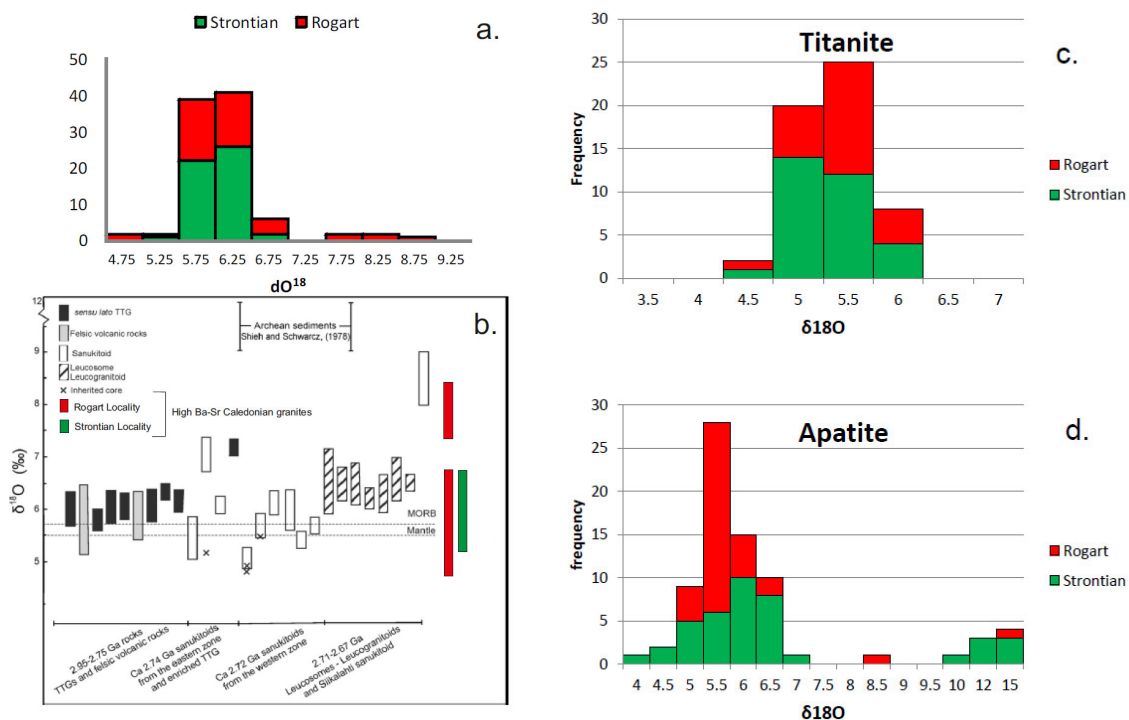
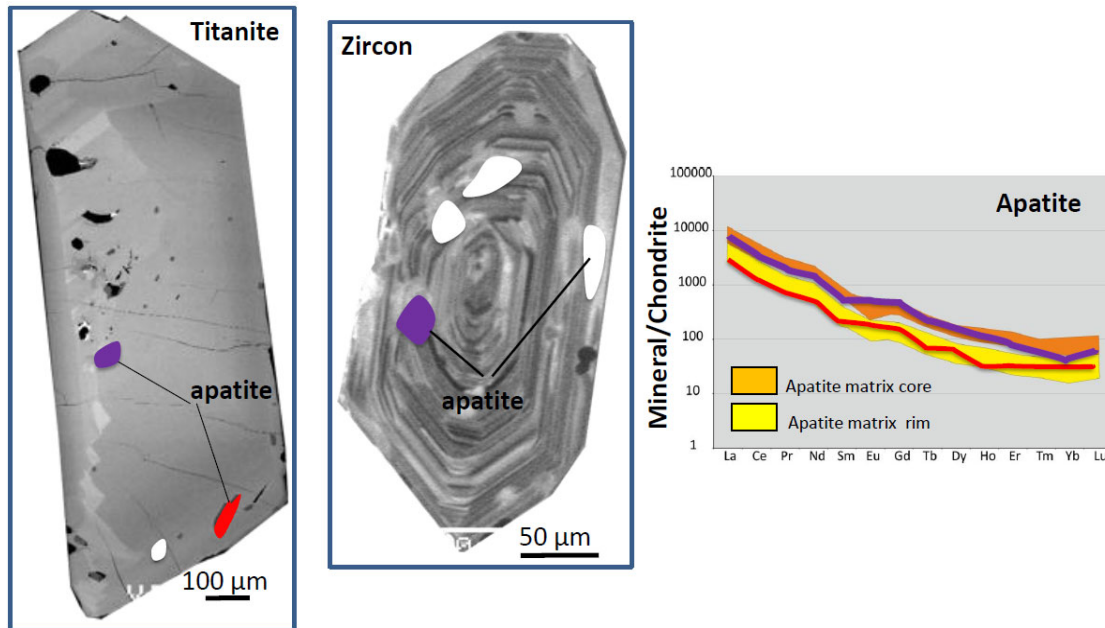


Figure 1. Oxygen isotope data for zircon (a and b) , titanite (c) and apatite (d) from high Ba-Sr granites.

Apart from the latter, these ranges are consistent with expectations from the zircon and whole-rock  $\delta^{18}\text{O}$  constraints, and will form the basis for detailed petrogenetic interpretation in due course. Very interestingly, there is no clear distinction between the two high Ba-Sr plutons, as was expected given the clear disparity in whole-rock radiogenic isotope systematics [3].

This requires further work (e.g. Hf isotopes in zircon) and awaits an explanation. Similarly, the high  $\delta^{18}\text{O}$  in apatite analyses are somewhat enigmatic, possibly the result of a crystallographic control, or the influence of micro-inclusions.



**Figure 2.** BSE and cathodoluminescence images with REE data for apatite inclusions in titanite and zircon.

*Trace elements.* During our research into the potential of detrital minerals to record sanukitoid (and other magma types) abundance through time, it has become apparent that apatites armoured within zircon might be a robust target provided that they faithfully record the composition of the magma from which they crystallised [4]. Figure 2 shows some results from the Cameca ims-4f that test this requirement. The red and purple coloured lines correspond to the apatite inclusions in titanite and zircon, overlay onto the ranges of LA-ICP-MS data for apatite crystals from the matrix of the same sample. The core-rim zonation of the latter is faithfully recorded in the inclusions data. Therefore, inclusion-bearing zircons such as these recovered from carefully-selected detrital sequences could furnish detailed chronological *and* magma-type information to inform our understanding of crustal evolution.

### Future work

The ion probe data briefly described above now form part of the NERC-funded project “When on Earth did modern plate tectonics begin?” (NE/I025573/1). They will be used in conjunction with whole-rock and mineral chemistry and isotope systematics to further constrain petrogenesis. They will then support the critical next challenge of the project, which is to establish elemental and/or isotopic fingerprints that adequately distinguish between TTG, sanukitoid and BADR parentage. When completed, a proof-of-concept source attribution study of detrital minerals from well-constrained river catchments will follow.

### References

- [1] M. Fowler and H. Rollinson (2012) *Geology* **40**, 1079-1082.
- [2] E. Heilimo, J. Halla, T. Andersen and H. Huhma (2012) *Precambrian Research* **In press**.
- [3] M.B. Fowler, H. Kocks, D.P.F. Darbyshire and P.B. Greenwood (2008) *Lithos* **105**, 129-148.
- [4] E.S. Jennings, H.R. Marschall, C.J. Hawkesworth and C.D. Storey (2011) *Geology* **39**, 863-866.

# Laki revisited: New quantitative constraints on deep degassing prior to large basaltic fissure eruptions

M.E. Hartley<sup>1</sup>, J. Maclennan<sup>1</sup>, M. Edmonds<sup>1</sup>, D.J. Morgan<sup>2</sup> & T. Thordarson<sup>3</sup>

<sup>1</sup>Department of Earth Sciences, University of Cambridge, Cambridge CB2 3EQ, UK

<sup>2</sup>School of Earth and Environment, University of Leeds, Leeds LS2 9JT, UK

<sup>3</sup>School of GeoSciences, University of Edinburgh, Edinburgh EH9 3JW, UK

## Background and Objectives

The AD 1783-84 Laki fissure eruption on Iceland's Eastern Volcanic Zone (EVZ) is the largest known historic eruption by volume, and produced  $>15 \text{ km}^3$  of basaltic lava and tephra [1]. Iceland's EVZ has been the source of a number of large basaltic fissure eruptions over the past 1200 years, and it is likely that another large volcanic eruption will occur on the EVZ in the next few decades to centuries. The Laki eruption is therefore an ideal case study for improving our understanding of the degassing processes that lead-up to large eruptions on the EVZ.

We used melt inclusions to quantify primary  $\text{CO}_2$  concentrations in the Laki magma. Melt inclusions from Laki commonly contain fluid bubbles, which form when post-entrapment crystallisation within an inclusion causes  $\text{CO}_2$  to exsolve from the melt. Previous studies using melt inclusions to quantify  $\text{CO}_2$  degassing have assumed that the amount of  $\text{CO}_2$  in fluid bubbles is negligible; however, it is possible to characterise the compositions of these fluid bubbles by Raman spectroscopy [2]. We therefore used a combination of Raman and SIMS data to reconstruct Laki's pre-eruptive degassing history.

The aim of this study was to address the following questions: How much  $\text{CO}_2$  was released from the Laki melt prior to eruption? At what depth did this  $\text{CO}_2$  release occur? How is  $\text{CO}_2$  degassing coupled to other magmatic processes?

## Results

We analysed  $\text{CO}_2$ ,  $\text{H}_2\text{O}$  and selected trace and rare earth elements in naturally-quenched, glassy, olivine-hosted melt inclusions from Laki. We also determined the  $\text{CO}_2$  content of fluid bubbles in melt inclusions by Raman spectroscopy, and then added the  $\text{CO}_2$  contained in the fluid bubble to the  $\text{CO}_2$  contained in the glass, to obtain the total  $\text{CO}_2$  content for each melt inclusion. Fluid bubbles typically comprise  $<5 \text{ vol.}\%$  of the melt inclusions, but contain  $\sim 90\%$  of the total  $\text{CO}_2$  in the melt inclusions. Melt inclusion  $\text{CO}_2$  and  $\text{H}_2\text{O}$  contents were used in the VolatileCalc volatile saturation model [3] to determine entrapment pressures for the melt inclusions. The entrapment pressures range from  $<0.1$  to  $>7 \text{ kbar}$  (Fig. 1).

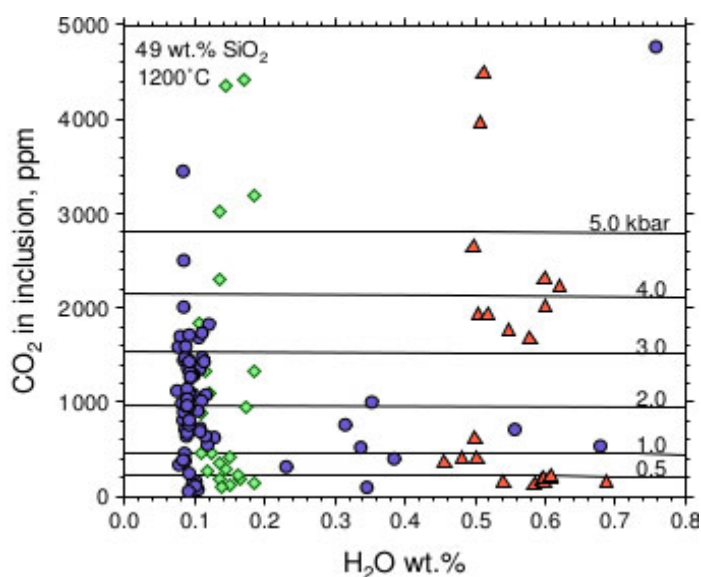


**Fig. 1.** Saturation pressures of Laki melt inclusions. Isobars calculated using [3]. Blue circles are lava samples; red triangles are tephra samples; green diamonds are data from [4].

Carbon is expected to behave as an incompatible trace element similar to Nb in a  $\text{CO}_2$ -undersaturated melt [5]. Therefore,  $\text{CO}_2/\text{Nb}$  ratios can be used to deconvolve the effects of crystallisation and degassing. Solubility models for  $\text{CO}_2$  in basaltic melt [3,6] can then be used to predict the degassing path of the Laki magma for different crystallisation models (Fig. 2). The Laki melt inclusions appear to record concurrent degassing and crystallisation, with most melt inclusions being trapped at shallower levels from a partially- or fully-degassed magma (Fig. 3).

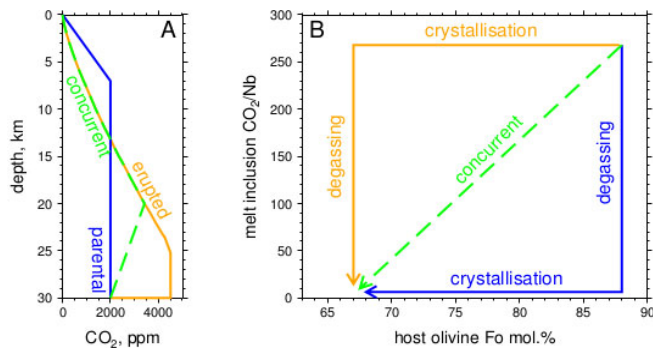


**Fig. 2.** Predicted dissolved CO<sub>2</sub> concentrations as a function of depth for basaltic melts. The blue ‘parental’ path corresponds to a situation where mantle melts rise to shallow levels in the crust and start to degas at ~7 km depth before crystallising. The orange ‘erupted’ path is where crystallisation occurs in the lower crust prior to magma ascent, and CO<sub>2</sub> loss commences at ~25 km depth. The green dashed line shows an example of concurrent crystallisation and degassing. (b) The same predicted paths on a plot of melt inclusion composition against host olivine composition.

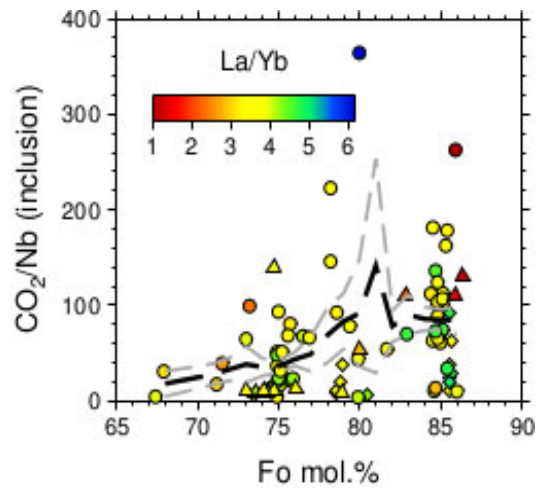


**Fig. 3.** Black dashed lines show the running average CO<sub>2</sub>/Nb ratio calculated using a boxcar filter with a bandwidth of 2 mol.% Fo; grey dashed lines show the standard error of estimate (SEE) of the filtered data.

The predicted CO<sub>2</sub> content of each melt inclusion if there were no degassing can be calculated using the Nb content of the melt inclusion and estimating the CO<sub>2</sub>/Nb of the mantle source. We used a CO<sub>2</sub>/Nb ratio of 314±125, as measured for melt inclusions from Borgarhraun in North Iceland [7]. MIs trapped at the highest pressures have lost the least CO<sub>2</sub> prior to entrapment (Fig. 4), as would be expected from solubility models. The most depleted MIs have lost the least CO<sub>2</sub>, and therefore depleted melt inclusions are not very useful for constraining deep degassing processes since they remain CO<sub>2</sub>-undersaturated to very shallow levels.

We calculated the total CO<sub>2</sub> mass release from the Laki magma, by associating each melt inclusion with a representative mass of melt. Our calculated CO<sub>2</sub> mass release is ~370 Mt. In comparison to previous estimates, this is very similar to an estimated CO<sub>2</sub> mass release of 348.7 Mt, calculated using the petrologic method and assuming a pre-eruptive CO<sub>2</sub> content of 8530 ppm [1]. However, if the pre-eruptive CO<sub>2</sub> content is assumed to be on the order of 300 ppm (i.e. the CO<sub>2</sub> content of the melt inclusion glass only) then the calculated mass release is just 8.3 Mt [4]. This highlights the importance of using both SIMS and Raman data to accurately calculate CO<sub>2</sub> budgets using petrologic methods.

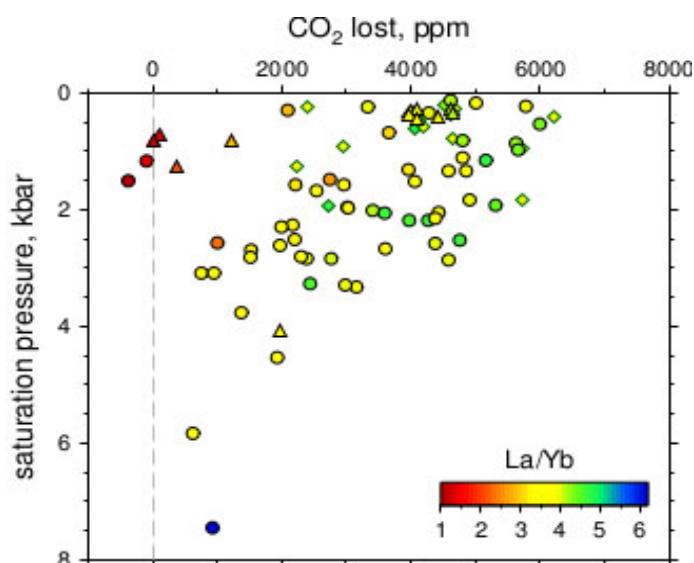


**Fig. 4.** Predicted CO<sub>2</sub> loss from each melt inclusion as a function of saturation pressure.

#### References

- [1] T. Thordarson et al. (1996) *Bull. Volcanol.*, **58**, 205-225
- [2] Y. Kawakami et al. (2003) *Applied Spectroscopy*, **57**, 1333-1339
- [3] S. Newman & J.B. Lowenstern (2002) *Computers & Geosciences*, **28**, 597-604
- [4] E. Passmore (2009) PhD thesis, University of Edinburgh
- [5] A.E. Saal et al. (2002) *Nature*, **419**, 451-455
- [6] T.A. Shishkina et al. (2010) *Chem. Geol.*, **277**, 115-125
- [7] E. Hauri et al. (2002) AGU Spring Meeting, V51D-03 (abstract)

# Diffusion of Volatiles in Earth's Mantle – Is it all about grain boundaries?

M. Hiscock & G. Bromiley

School of GeoSciences, University of Edinburgh, Edinburgh EH9 3JW, UK

## Abstract

Earth's mantle contains a considerable volume of 'water' stored as interstitial H defects in mantle minerals. To constrain the important influence that H has on mantle properties and processes we have previously conducted experiments to determine grain boundary diffusivity of H as it is believed that grain boundaries may potentially provide fast pathways for diffusion. These experiments found that H diffusion proceeded at a similar rate in both lattice and grain boundary diffusion settings. It was hypothesised that this may be due to the extremely small radii of H<sup>+</sup> ions. To test this hypothesis a further set of experiments was conducted with a larger radius diffusant, Li. Results from a very limited data set indicate that Li grain boundary diffusion is significantly faster than its lattice equivalent suggesting that our hypothesis may indeed be true.

## Grain boundary Diffusion within the Earth

Diffusion of atomic species in Earth's mantle can occur via one of two mechanisms: (1) Through mineral grains; *lattice diffusion* or (2) Along the boundaries between grains; *grain boundary diffusion*. Research in materials science and solid-state chemistry has demonstrated that grain boundary diffusion may be the dominant process under certain conditions. However, to date the relative importance of grain boundary diffusion under high-PT conditions of Earth's deep interior remains poorly constrained. Grain boundary diffusion has been suggested to play an important role in mobilising highly incompatible elements in the mantle, for example in providing an efficient mechanism for mixing highly siderophile elements from the core into the lower mantle [1]. It has previously been assumed (without any real justification!) that lattice diffusion of H is dominant, although the relative efficiency of grain boundary diffusion of H under high PT conditions of the mantle remains unknown. Previous work utilising the SIMS facilities at EMMAC found that there was little difference between lattice and grain boundary diffusivities of H. Here we used a novel experimental design and SIMS analysis to test the hypothesis that this observation is due to the very small ionic radius of H. This was done by conducting a series of grain boundary diffusion experiments with Li (which has a much larger ionic radius) as the diffusant.

Grain boundary diffusion coefficients for Li under similar conditions to the original investigation into H were determined from experiments conducted at high temperature (800°C - 1100°C) and pressure (3GPa) using a novel capsule design (Figure 1.). Whilst the experimental design was unable to preclude lattice diffusion, this was not problematic as lattice diffusion of Li in olivine has previously been characterised [2]. Li-orthosilicate was chosen as a source of diffusant and released its Li as experiments were heated. By measuring Li contents of the olivine grains and determining the distance of analysis points from the interface of the Li-orthosilicate and olivine (by subsequent SEM analysis) a grain boundary diffusion coefficient could be determined. A grain size of approx. 100µm was used to ensure that the sectioned capsule presented grains of a suitably large area for analysis with a beam size of approx. 20 x 25µm (the actual section and so individual grains which are exposed when the capsule is cut in half is essentially random) (see Figure 2). A 5nA beam current was used and Li & Si contents were measured.

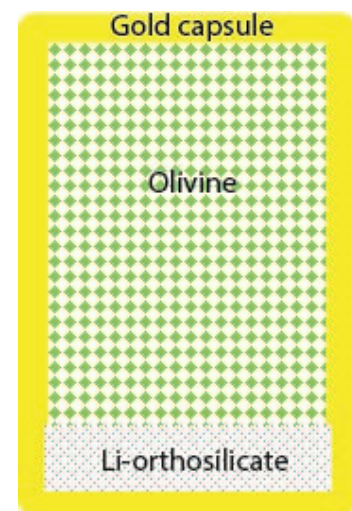
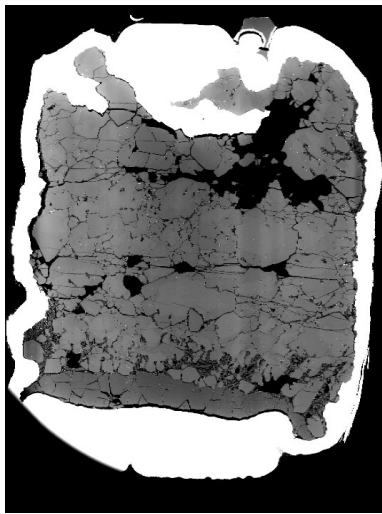


Figure 1. Capsule design.

Compiled results (see Fig. 3 for example data) indicate that grain boundary diffusion coefficients of Li under the experimental conditions are significantly quicker than those obtained from measured measurements in a single crystal diffusion scenario [2]. Only a very limited amount of data was able to be obtained in this experimental program but the data suggests that a combination of ionic radii and

temperature are likely to control bulk diffusive transport mechanisms in the Earth. This work specifically builds towards a greater understanding of the mechanisms of diffusion of light elements under the conditions of the Earth's interior (Fig. 4).



**Figure 2.** SEM image of sectioned capsule. Large grain sizes allow for the easy positioning of an ion probe beam on the sample. Distances for the calculation of diffusion coefficients are subsequently measured using an SEM.

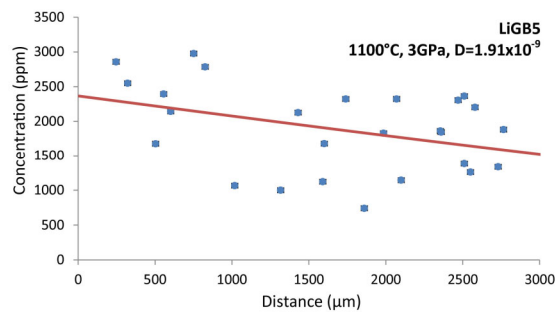


**Figure 3.** Example diffusion law fit from experiment analysed by SIMS this year.

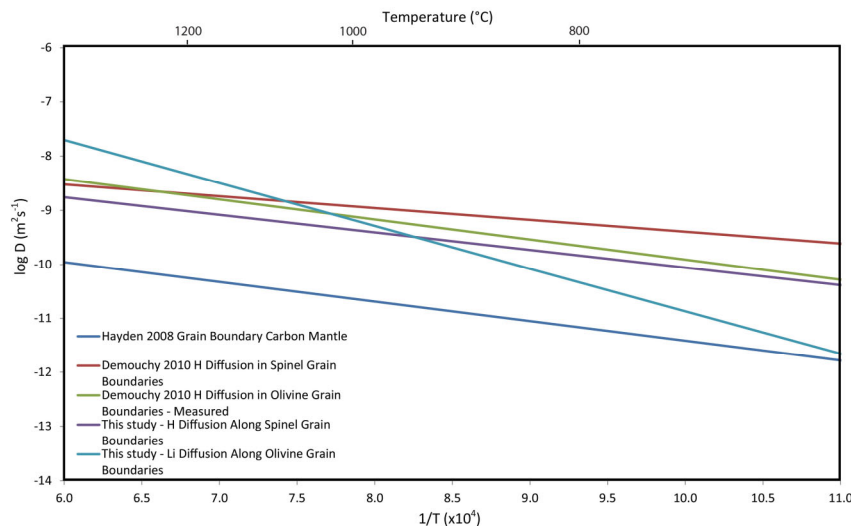


**Figure 4.** Arrhenius plot showing measured diffusivities of various light elements obtained both in this investigation and by other workers. Varying gradients show temperature to be a controlling factor and the vertical positioning of lines suggests ionic radii may also play a significant role. Includes data from [3–5].

## References

- [1] L. A. Hayden and E. B. Watson, "A diffusion mechanism for core-mantle interaction," *Nature*, vol. 450, no. 7170, pp. 709–711, Nov. 2007.
- [2] R. Dohmen, S. A. Kasemann, L. Coogan, and S. Chakraborty, "Diffusion of Li in olivine. Part I: Experimental observations and a multi species diffusion model," *Geochimica et Cosmochimica Acta*, vol. 74, no. 1, pp. 274–292, Jan. 2010.
- [3] S. Demouchy, "Hydrogen diffusion in spinel grain boundaries and consequences for chemical homogenization in hydrous peridotite," *Contributions to Mineralogy and Petrology*.
- [4] S. Demouchy, "Diffusion of hydrogen in olivine grain boundaries and implications for the survival of water-rich zones in the Earth's mantle," *Earth and Planetary Science Letters*, vol. 295, no. 1–2, pp. 305–313, Jun. 2010.
- [5] L. A. Hayden and E. B. Watson, "Grain boundary mobility of carbon in Earth's mantle: A possible carbon flux from the core," *Proceedings of the National Academy of Sciences*, vol. 105, no. 25, pp. 8537–8541, Jun. 2008.

# Constructing a new terrestrial palaeo-environment thermometer - earthworm secreted calcite granules

M.E. Hodson<sup>1</sup>, E.A.A. Versteegh<sup>2</sup>, S. Black<sup>2</sup>, P.F. Schofield<sup>3</sup>, M.R. Lee<sup>4</sup>

<sup>1</sup>Environment department, University of York, York, YO10 5DD, UK

<sup>2</sup>School of Human and Environmental Sciences, University of Reading, Reading, RG6 6AB, UK

<sup>3</sup>Department of Earth Science, Natural History Museum, London, SW7 5BD, UK

<sup>4</sup>School of Geographical and Earth Sciences, University of Glasgow, Glasgow, G12 8QQ, UK

Earthworms secrete granules of calcium carbonate that are up to 2 mm in diameter and consist predominantly of calcite (Fig. 1) [1, 2].

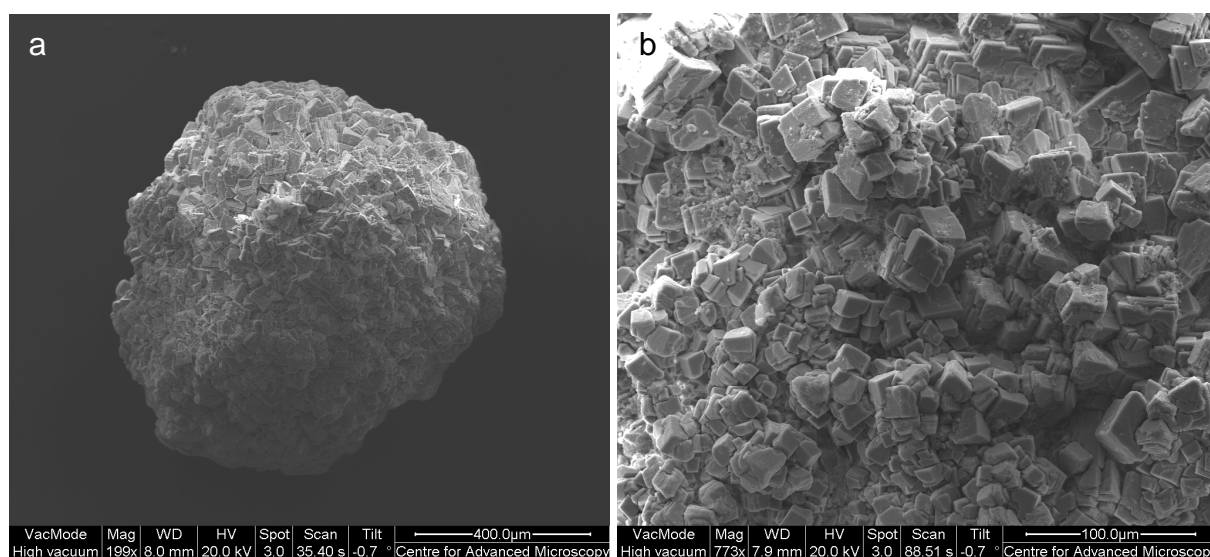


Fig. 1. Earthworm calcium carbonate granules, secondary electron images. a) Individual granule showing the agglomeration of calcite rhombs that make up a granule. Scale bar is 400  $\mu\text{m}$ . b) Close up of (a). Scale bar is 100  $\mu\text{m}$ .

They are produced in specialised calciferous glands [3]. Experiments suggest that individual granules take a few hours up to a day to form [4,5]. Granules are commonly recovered from soils and sediments of Quaternary age [4, 6]. They have been found, amongst other sites, at Silbury Hill (c. 4300 BP) and Boxgrove (middle Pleistocene and the site of the discovery of Boxgrove Man). Even the clay quarry Russel-Tiglia in the Netherlands yielded well-preserved granules that are about 2 million years old. However, it has also been shown that earthworm calcite granule assemblages from an individual sample of soil can be of a mixed age [5] and thus granules need to be treated on an individual basis if they are to be used in palaeo-environmental reconstruction. We have shown in preliminary work that individual granules contain sufficient U and Th for them to be dated by the U-Th method. After dating, sufficient material remains for C and O isotopic determinations by stable isotope ratio mass spectrometry (SIRMS) (Fig. 2).

We have hypothesised that there will be a systematic variation in O isotope fractionation into the granules with differences in temperature, as is observed in other carbonate systems [8]. Given that  $\delta^{18}\text{O}$  values of soil pore water in temperate climates generally reflect that of precipitation, seasonal ranges of (palaeo-) temperatures may be calculated using earthworm granules collected in the field. This, combined with the longevity of the granules in soils, and the widespread distribution of granule producing earthworms, will provide the palaeoclimate community with a new, widely applicable and much needed, terrestrial palaeothermometer to complement other proxies, such as tree rings and speleothems.

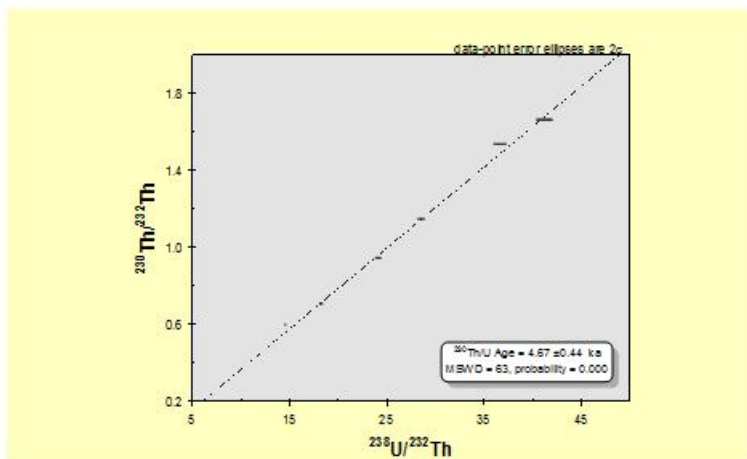


Fig. 2. U-series isochron plot of multiple analyses of earthworm granules recovered from a buried soil horizon in Silbury Hill. The horizontal lines running across the dot-dash isochron are actually error ellipses for individual U-Th measurements. The earliest date for the buried soil in Silbury Hill is circa 4400 ca. BP which is consistent with the U-Series age for the carbonate granules, indicating they are contemporaneous with the soil formation.

Results of our experiments to date have enabled us to derive an equation showing the relationship between granule oxygen isotope composition, temperature and oxygen isotope composition of soil pore water [7]. However, both modern and palaeo-granules show composition zoning indicating chemical heterogeneity (Fig. 3). If this heterogeneity is also present in the oxygen isotope composition of the granules, using their bulk oxygen isotope signatures to reconstruct past temperatures might be called into question. Thus the aim of the measurements reported here were twofold: 1. to determine whether  $\delta^{18}\text{O}$  values of granules vary with their trace element composition and, 2. to determine whether granules are sufficiently isotopically homogenous so that bulk  $\delta^{18}\text{O}$  values potentially retain a temperature signature.

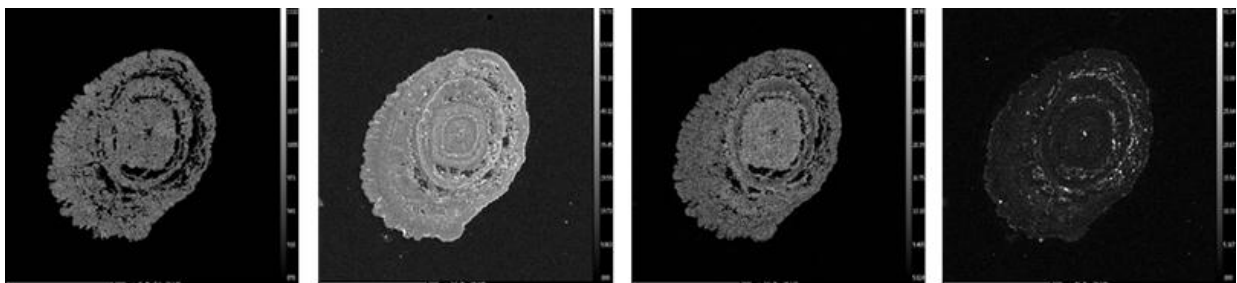


Fig. 3. Element distribution maps of a “recent” granule section showing concentric zoning of (from left to right) Ca, Mg, Mn and Na running across the radial distribution of calcite crystals.

Oxygen isotope analysis was carried out on linear transects through sections of one recent and two palaeo-granules. Subsequently trace element analysis was carried out on parallel transects. Oxygen isotope variation within transects was within the levels of uncertainty associated with the analysis (0.3 per mil) and therefore it was not possible to demonstrate variation in oxygen isotope values with trace element chemistry. The granules can therefore be considered isotopically homogeneous. This supports our use of granule bulk oxygen isotopic composition for palaeotemperature reconstructions.

## References

- [1] M.R. Lee, M.E. Hodson and G. Langworthy (2008) *Geology* **36**, 943–946.
- [2] L. Gago-Duport, M.J.I. Briones, J.B. Rodríguez and B. Coveló (2008) *Journal of Structural Biology* **162**, 422–435.
- [3] T.G. Pearce (1972) *Journal of Animal Ecology* **41**, 167–188.
- [4] M.G. Canti (2007) *Journal of Quaternary Science* **22**, 111–118.
- [5] M.G. Canti (2007) Unpub. Thesis, Royal Holloway and Bedford New College.
- [6] M.G. Canti (1998) *Boreas* **27**, 275–288.
- [7] E.A.A. Versteegh, S. Black, M.G. Canti and M.E. Hodson (submitted) *Geochimica et Cosmochimica Acta*

# Volatiles and Fe oxidation state in hydrous rhyolite

M.C.S. Humphreys<sup>1</sup> & R. Brooker<sup>2</sup>

<sup>1</sup>Department of Earth Sciences, University of Oxford, South Parks Road, Oxford, OX1 3AN, UK

<sup>2</sup>Department of Earth Sciences, University of Bristol, Wills Memorial Building, Queen's Road, Bristol, BS8 1RJ

## Introduction

*In situ* measurements of  $\text{Fe}^{3+}/\Sigma\text{Fe}$  (made using XANES) in primitive basaltic melt inclusions have recently been used to make interpretations about the oxidation state of the mantle wedge at subduction zones. Increased Fe oxidation state with increasing  $\text{H}_2\text{O}$  concentration and other tracers of slab-derived fluids (e.g. Ba/La) suggests that a hydrous 'slab component' may be the source of this oxidation signature [1]. This work demonstrates that *in situ* spectroscopy of melt inclusions can provide valuable information about the oxidation state of the magmas from which they are trapped. However, in many volcanic systems, melt inclusions are trapped at varying stages of magma ascent, during degassing and crystallisation [2,3]. It is therefore essential to understand how low-pressure magmatic processes such as degassing may affect melt oxidation state, in particular for more evolved melts such as rhyolites, and also to quantify any effect of  $\text{H}_2\text{O}$ , as a chemical constituent of the melt, on  $\text{Fe}^{3+}/\Sigma\text{Fe}$ .

## Approach

We analysed the  $\text{H}_2\text{O}$  contents of hydrous rhyolite glasses from decompression experiments [4] to complement synchrotron micro-XANES data ( $\text{Fe}^{3+}/\Sigma\text{Fe}$ ) already collected for the same samples at the Diamond Light Source, with the aim of quantifying changes in  $\text{Fe}^{3+}/\Sigma\text{Fe}$  due to degassing of hydrous rhyolite at relatively oxidising conditions. We also analysed the  $\text{H}_2\text{O}$  contents of partially hydrated rhyolite (both natural and high-temperature examples) to evaluate whether the mechanisms of hydration and dehydration have different controls on oxidation state. The  $\text{H}_2\text{O}$  data were combined with back-scattered electron SEM images of the samples to give maps of  $\text{H}_2\text{O}$  concentration, and plotted against  $\text{Fe}^{3+}/\Sigma\text{Fe}$  (Figures 1 and 2).

## Preliminary results and conclusions

For the dehydrated rhyolites,  $\text{Fe}^{3+}/\Sigma\text{Fe}$  increases slightly with decreasing  $\text{H}_2\text{O}$  content (Figure 1). The occurrence of oxidation during dehydration of rhyolites is consistent with previous modelled predictions [5], although the degree of oxidation is lower than that expected from theoretical models. The reason for this is not yet clear but may be related to the presence of large volumes of exsolved vapour in the capsule. Oxidation is thought to result from degassing of  $\text{H}_2$  from the sample together with  $\text{H}_2\text{O}$ , according to:

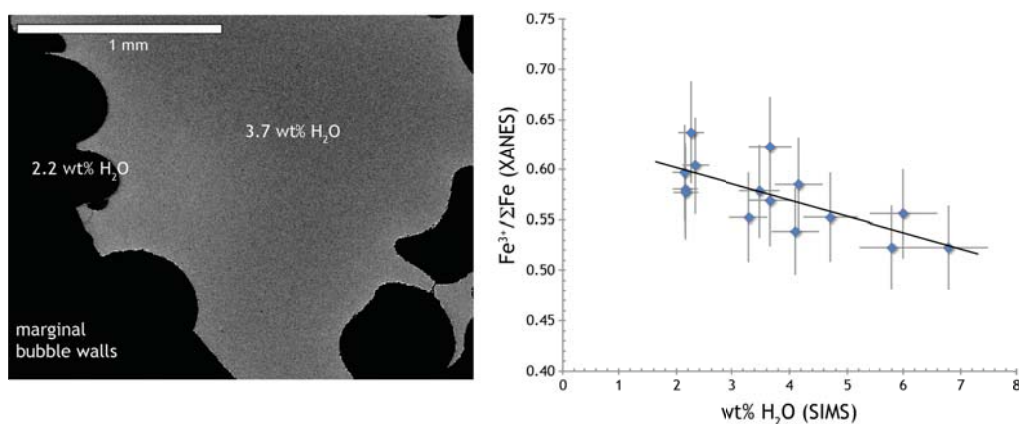
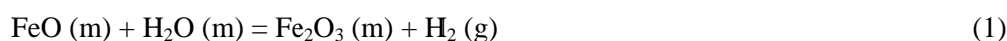


**Figure 1:** *Left:* Typical experimentally decompressed rhyolite chip with greyscale gradient indicating loss of  $\text{H}_2\text{O}$  from centre to margin. *Right:*  $\text{Fe}^{3+}/\Sigma\text{Fe}$  increases with decreasing  $\text{H}_2\text{O}$  content for the experimental samples of Mangan & Sisson (2000).

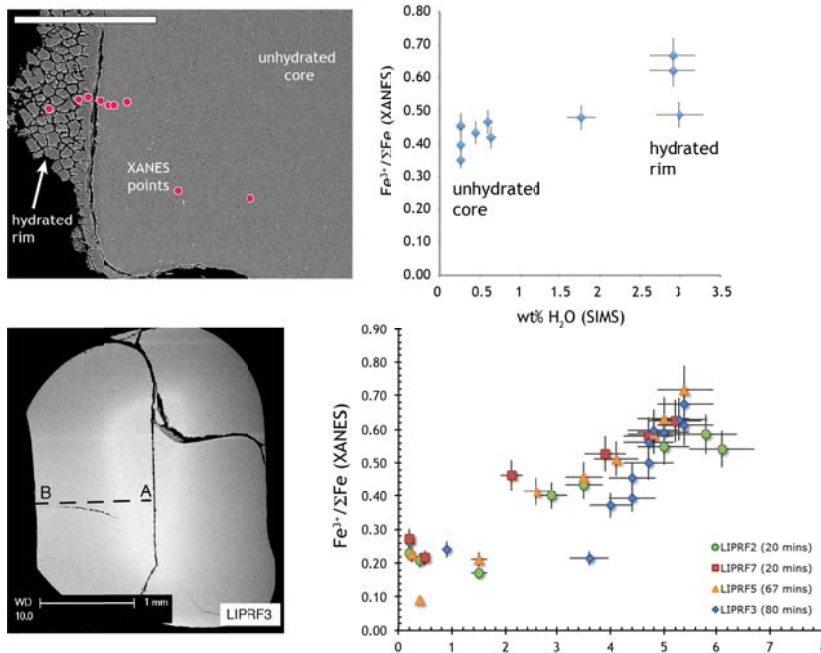


**Figure 2:** Left panel: Back-scattered electron SEM images of low-temperature (top) and high-temperature (bottom) hydrated obsidians. Right panel: raw datasets for both hydrated samples show increasing Fe oxidation state with increasing H<sub>2</sub>O content.

In contrast, for both high-temperature and low-temperature hydrated rhyolites  $\text{Fe}^{3+}/\Sigma\text{Fe}$  increases substantially with increasing H<sub>2</sub>O content (Figure 2). This result is in part due to variations of  $X_{\text{H}_2\text{O}}$  within the samples (H<sub>2</sub>O-undersaturated conditions result in lower  $f_{\text{O}_2}$  at constant  $f_{\text{H}_2}$ ) but after correcting for this there is still a slight positive dependence of  $\text{Fe}^{3+}/\Sigma\text{Fe}$  with H<sub>2</sub>O content (Figure 3). Preliminary analysis indicates that this may be related to the influence of H<sub>2</sub>O on the activity of the FeO and Fe<sub>2</sub>O<sub>3</sub> components in the melt [6]. This is consistent with the concept of addition of H<sub>2</sub>O changing acid-base equilibria within the melt and causing adjustments of  $\text{Fe}^{3+}/\text{Fe}^{2+}$  [7]. This concept has further implications for the influence of other volatile anions (e.g. Cl) on Fe oxidation state in magmas, as well as the solubility of volatiles (e.g. CO<sub>2</sub>) in highly basic melts.

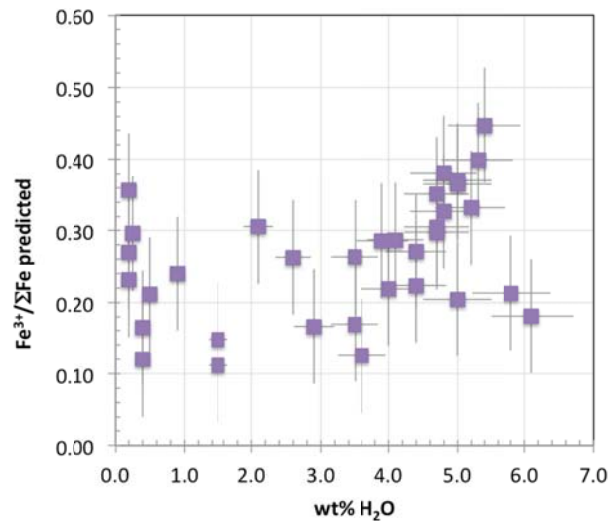


**Figure 3:** After correction for variations in  $X_{\text{H}_2\text{O}}$  in the partially hydrated samples there remains a positive dependence of  $\text{Fe}^{3+}/\Sigma\text{Fe}$  on H<sub>2</sub>O content.

## References

- [1] Kelley & Cottrell (2009) *Science* **325**, 605-607
- [2] Blundy & Cashman (2005) *Geology* **33**, 793-796
- [3] Johnson et al. (2008) *EPSL* **269**, 478-487
- [4] Mangan & Sisson (2000) *EPSL* **183**, 441-455
- [5] Burgisser & Scaillet (2007) *Nature* **445**, 194-197
- [6] Gaillard et al. (2003) *GCA* **67**, 4389-4409
- [7] Fraser (2005) *Ann Geophys* **48**, 549-559

# Compositional heterogeneity of the Earth's mantle: constraints from olivine-hosted melt inclusions from a continental flood basalt setting

E.S. Jennings, S.A. Gibson & J. Maclennan

Department of Earth Sciences, University of Cambridge, Cambridge, CB2 3EQ

## Background

Low-volume, high-Mg mantle-derived melts from the Etendeka continental flood basalt (CFB) province in Namibia accompany the main CFB flows and provide a rare opportunity to study the mantle-plume source of such regions. These picrites are primitive, olivine-rich, and derived from high temperature melting of peridotite in the head of the upwelling mantle plume [1]. In contrast, rare ferropicrite melts are thought to be derived from the higher pressure, lower degree melting of a non-peridotite lithology such as garnet pyroxenite [2,3] in the plume head. This pyroxenite is ultimately sourced from lithospheric recycling. This study explores further the origin of these picrites: what they can tell us about the composition of mantle present in upwelling plumes, as well as the crustal storage conditions and degree and style of contamination experienced by this globally-rare magma type as it ascends to the surface.

Previous studies have focussed on whole-rock geochemistry, isotopic work and the experimental investigation of ferropicrite genesis; this project aims to extend this work in order to gain a detailed petrogenetic history of these rocks using the trace-element geochemistry of rehomogenised olivine-hosted melt inclusions (MIs). Olivine-hosted melt inclusions in primitive, mantle-derived melts provide a 'snapshot' of melt compositions shortly after leaving the mantle source, preserving information on melting conditions and source heterogeneity prior to the combined lithospheric contamination, fractionation and mixing processes which ultimately serve to destroy this detailed information. Melt-inclusion compositions from ferropicrite olivines in particular will help constrain the trace-element composition of recycled components in the mantle.

## Results

Although this project is still in progress, a summary of findings so far are listed:

### 1) Lithospheric contamination and crustal storage conditions

Interestingly, melt inclusions in both sample sets generally show at least the same level of contamination as their respective whole-rock samples, implying a very short timescale for assimilation. This may be due to the high temperatures when the magmas are first emplaced, or to sample bias; inclusions are more likely to be trapped during melt-wall-rock reaction (c.f. [4]). Specifically, MIs from ferropicrites reflect the same lower crustal signature as the whole rocks, contaminated to the same or even greater extents (fig. 1b and 1c). This lower crustal signature implies storage near the Moho.

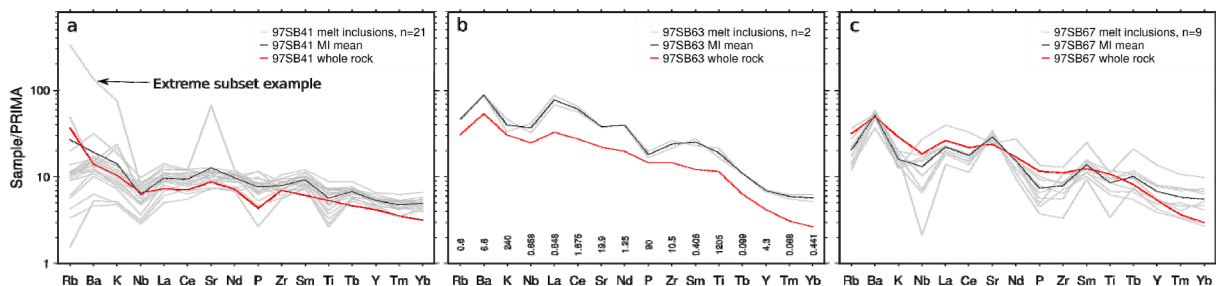


**Figure 1** Multi-element plots showing trace element distribution in MIs and their respective host rock. a) One picrite representative sample, showing both normal inclusions and an extremely contaminated one; b) most forsteritic (primitive) ferropicrite sample; c) least forsteritic ferropicrite sample.

This is also indicated by the presence of high-pressure clinopyroxene phenocrysts and may reflect the high density of the iron-rich melts relative to the surrounding crust. Picrite MIs bear a generic ‘spiky’ incompatible trace element signature which may relate to middle/upper crustal storage; the majority are similar to whole-rock samples, whereas a small subset bears an ‘extreme’ pattern, likely due to localised wall-rock reaction (fig. 1a).

## 2) Mantle source characteristics

Characterising the mantle source of the two suites of picrites is at present made more difficult by lithospheric contamination, and the varying effect of lithospheric thickness and temperature as well as source composition in the melting region. In addition, melt inclusions in the ferropicrite olivines were very rare; only 18 suitable melt inclusions were found, spanning a host olivine forsterite range from 0.63 to 0.83. It is, however, clear that the ferropicrite melt is very different to the picrite; the two cannot be related by fractionation. A very low Sc/Zr ratio in the most primitive ferropicrite inclusions relative to the picrites is striking, and could indicate a high modal proportion of cpx and/or garnet in the source (fig. 2). Combined with a low relative Y/Nb and high La/Lu indicating residual garnet, this is consistent with a garnet-clinopyroxenite source. Unfortunately, similar trends would be expected purely as a result of a thicker lithosphere and more restricted melting, so planned further modelling will explore this further. An interesting, unexplained feature of the ferropicrite MIs is the increasing Sc/Zr with decreasing Fo of the host olivine (fig. 2), as cpx fractionation would result in the converse trend.

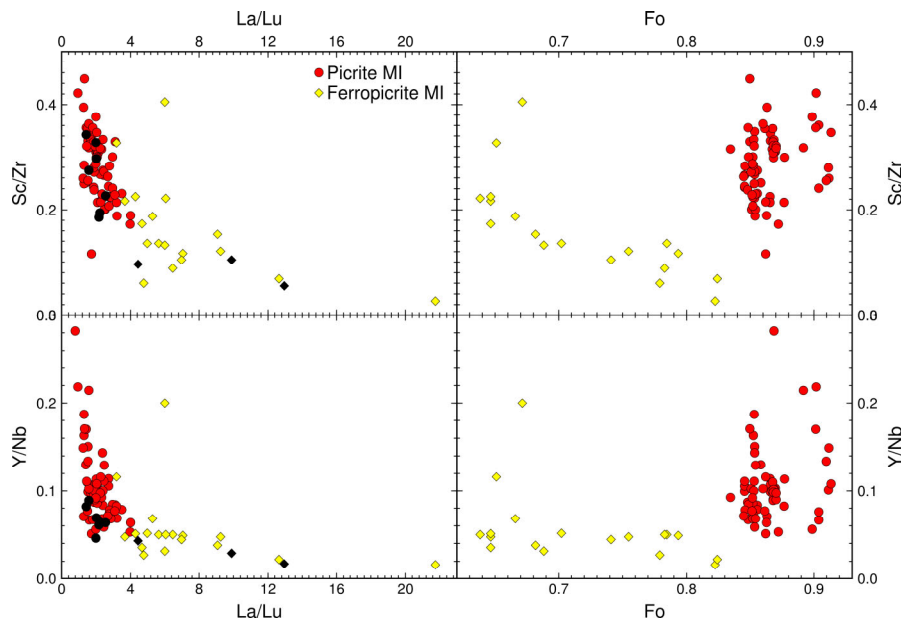


**Figure 2** Various trace element ratios of picrite (red circles) and ferropicrite (yellow diamonds) MIs and their respective whole-rock hosts (filled black symbols) plotted against MI or whole-rock La/Lu and host olivine forsterite (Fo) content.

## 3) Major element vs. trace element compositions in re-homogenised melt inclusions

EPMA measurements of the melt inclusions prior to SIMS analysis has revealed the unreliability of the major-element compositions of experimentally re-homogenised melt inclusions, due to diffusive exchange and direct melting of olivine into the inclusions. This cannot be corrected for, but luckily should not affect the relative concentrations of trace elements. This highlights the importance of trace element data in these samples, as it must compensate for another lost form of data. Since all global reported ferropicrite olivine-hosted MIs are crystalline, this will always be a problem.

## References

- [1] Thompson R. N., et al. (2001) *J Petrol* **42**, 2049-2081
- [2] Gibson S. A. (2002) *Earth Planet Sc Lett* **195**, 59-74
- [3] Tuff J., et al. (2005) *J Petrol* **46** 2023-2058
- [4] Danyushevsky L. V., et al. (2004) *J Petrol* **45**, 2531-2553

# Cenozoic arc magmatism along the active Andean margin

R.Jones<sup>1</sup>, L.Kirstein<sup>1</sup>, R.Hinton<sup>1</sup>, S.Kasemann<sup>2</sup>, & T.Elliott<sup>3</sup>

<sup>1</sup>School of GeoSciences, University of Edinburgh, Edinburgh, EH9 3JW, UK

<sup>2</sup>Department of Geosciences, University of Bremen, Germany

<sup>3</sup>Department of Earth Sciences, University of Bristol, BS8 1RJ, UK

## Introduction

Subduction zones, such as the Andean convergent margin, are the main producers of new continental crust via arc magmatism and active sites for crustal recycling. Arc magmas and hence new continental crust are composed of variable contributions from mantle, crustal and subducted reservoirs. The aim of this study is to investigate how the contamination of arc magmas in the southern Central Andes has varied during the Cenozoic, specifically in relation to changing subduction zone geodynamics.

The study area lies within the currently volcanically inactive Pampean flat slab segment (~27°-33°S) of the Southern Central Andes. During the Miocene the angle of the subducting Nazca plate shallowed, leading to the eastward migration of the magmatic arc and eventual termination of arc magmatism in the Late Miocene [1]. Subduction erosion, tectonic erosion, and crustal contamination have all been highlighted as important processes in the region [2, 3, 4].

Due to the limited number of reliable age determinations the onset and duration of magmatic activity in the southern Central Andes is poorly constrained. In order to better constrain the timing of southern Central Andean arc magmatism in-situ U-Pb dating was carried out on ~400 zircons (including those analysed in 2011) separated from series of strategically collected samples, using the Cameca IMS-1270. In order to critically evaluate the source of the melt and how it may have evolved, oxygen isotope ratios have been measured on the dated zircons, using the Cameca IMS-1270. These results have been combined with Hf isotope ratios (LA-ICPMS, University of Bristol) in order to assess the varying roles of crustal and mantle components in the magmatic evolution of the southern Central Andes.

## Results

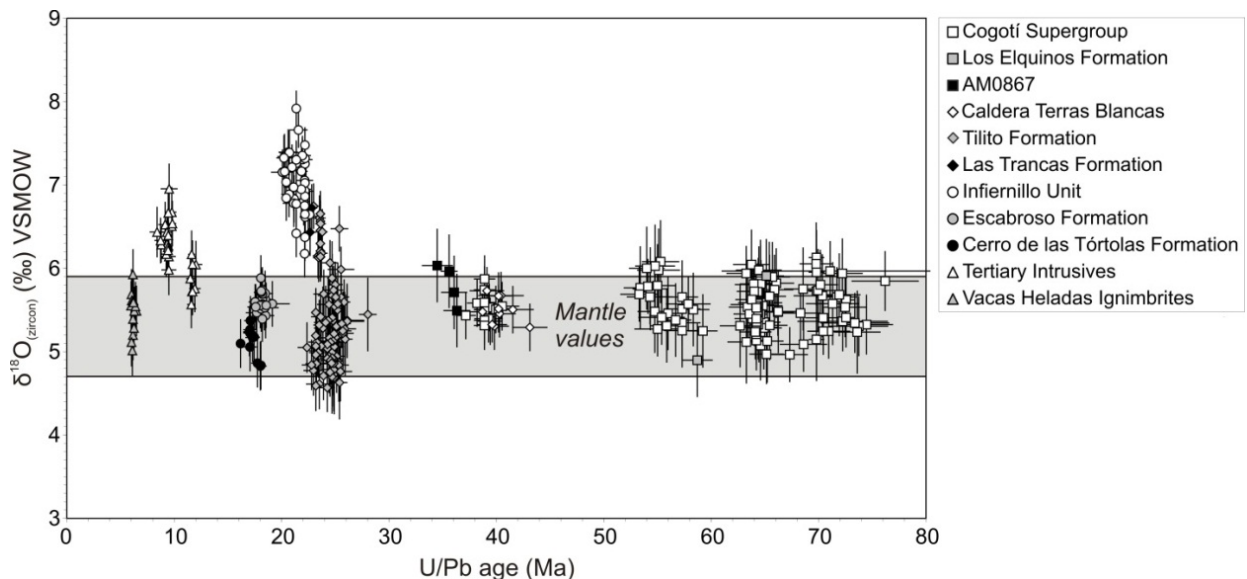


**Figure 1.**  $\delta^{18}\text{O}_{(\text{zircon})}$  values plotted against  $^{206}\text{Pb}/^{238}\text{U}$  ages for un-inherited zircon grains from the Late Cretaceous – Late Miocene aged samples. Intrusive samples are shown as open symbols and extrusive samples as filled symbols. The grey bar highlights the  $\delta^{18}\text{O}_{(\text{zircon})}$  values for zircon in isotopic equilibrium with mantle derived melts ( $5.3\text{‰} \pm 0.6$ ) [5]. Errors bars represent  $2\sigma$ .

The majority of  $\delta^{18}\text{O}_{(\text{zircon})}$  values lie within the range of values expected for zircon crystallising in isotopic equilibrium with mantle derived melts ( $5.3\pm 0.6\%$  [5]) (Fig. 1). The higher than ‘mantle like’  $\delta^{18}\text{O}_{(\text{zircon})}$  values obtained for some of the Late Oligocene – Late Miocene magmatics (Fig. 1) suggest the incorporation of a  $^{18}\text{O}$  enriched supracrustal component into the magma from which the zircon crystallised. As oxygen isotopes are sensitive to water-rock interactions and the fractionation of oxygen isotopes increases with decreasing temperature the interaction of magmas with sediments and/or low temperature altered crust leads to elevated  $\delta^{18}\text{O}_{(\text{zircon})}$  values.

The  $^{206}\text{Pb}/^{238}\text{U}$  ages for individual zircon grains range between  $76.2 \pm 3.1$  and  $6.0 \pm 0.1$  Ma (Fig. 1). Inherited zircon cores have been identified in specific Oligocene to Miocene aged samples (Fig. 2) providing further evidence for interaction with older crustal material. The majority of these inherited zircon cores are Permian to Triassic in age with some Proterozoic ages obtained for zircon cores present in samples from the Argentinean Precordillera.

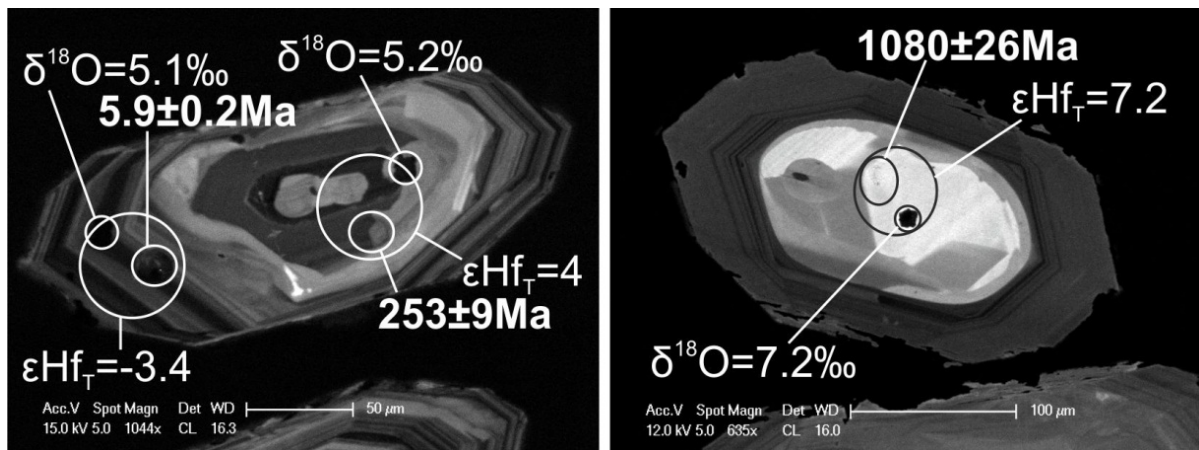


**Figure 2.** Cathodoluminescence (CL) images of select zircon grains highlighting the presence of inherited cores, internal growth zoning, and the locations of in-situ isotopic analysis. The oxygen isotope ratios are expressed in  $\delta^{18}\text{O}$  notation (‰) relative to SMOW, the hafnium isotope values are expressed as initial  $\epsilon\text{Hf}_T$  values (calculated using the  $^{206}\text{Pb}/^{238}\text{U}$  age obtained by SIMS) and the ages (in Ma) are presented as the  $^{206}\text{Pb}/^{238}\text{U}$  ages. Errors are quoted at the 2 sigma level.

## Discussion

Mantle-like  $\delta^{18}\text{O}_{(\text{zircon})}$ , combined with mantle-like  $\epsilon\text{Hf}_{(\text{zircon})}$  values (LA-ICPMS), suggest the Late Cretaceous to Mid Eocene arc magmatics were derived from mantle melts with little contribution from upper crustal material, either from the subduction of continental crust or from crustal assimilation. Oxygen and hafnium isotope values obtained for Late Oligocene to Late Miocene magmatics, combined with the presence of inherited zircon populations, reflects the assimilation of different basement terranes as arc magmatism migrated to the east during the latter part of the Cenozoic.

## Use of results

The results of this work have been presented at two conferences (Goldschmidt 2012 and VMSG 2013) and form the basis of two publications currently in press.

## References

- [1] Pilger, R. H., (1984), *Journal of the Geological Society London*, **141**, 793 - 802.
- [2] Stern, C. R., (1991), *Geology*, **19**, 78 - 81.
- [3] Hildreth, W., and Moorbath, S., (1988), *Contributions to Mineralogy and Petrology*, **98**, 455 - 489.
- [4] Stern, C. R., (2004), *Rev. geol. Chile*, **31**, 161-206.
- [5] Valley, J.W., et al., (1998) *Contributions to Mineralogy and Petrology*, **133**(1-2), 1-11.

# **U-Pb dating of the felsic and intermediate volcanic sequence of the nickel-sulphide bearing Cosmos succession, Agnew-Wiluna greenstone belt, Yilgarn Craton, Western Australia**

A. Kaye (now: de Joux)<sup>1</sup>, T.Thordarson<sup>1</sup>, M.Denny<sup>2</sup>, R.Hinton<sup>1</sup> & A.J. de Joux<sup>2</sup>

<sup>1</sup>School of GeoSciences, University of Edinburgh, Grant Institute, The King's Buildings, Edinburgh, EH9 3JW

<sup>2</sup>Xstrata Nickel Australasia, 24 Outram Street, Level 3, West Perth, Western Australia 6005, Australia

## **Introduction**

Within the Archean Yilgarn Craton of Western Australia, ion-probe analysis of zircons has been used extensively over the last 20 years in an attempt to provide a geological and metamorphic framework for the Yilgarn Craton as a whole and to link individual greenstone terranes [1], which are often endowed with appreciable nickel and gold mineralisation. While current dating for the Yilgarn Craton, in particular the Eastern Goldfields Superterrane (EGS) is wide-ranging and allows for coherent reconstruction of the regional tectonics and large-scale geological evolution of the Yilgarn Craton [1], high-resolution dating of individual successions is currently insufficient for assessing the timing and longevity of volcanism, and accompanying mineralisation, on a terrane by terrane scale.

The purpose of this study is to present new age constraints for the Cosmos volcanic succession, which lies within the Agnew-Wiluna greenstone belt of the EGS and contains several massive and disseminate, komatiite-hosted, nickel sulphide deposits. Nine different zircon-bearing lithologies within the succession were U-Pb dated, including distinct stratigraphic footwall and hangingwall felsic units as well as intrusive felsic porphyries that cross-cut the succession. The results indicate that construction of the Cosmos succession took at least 80 million years, featuring punctuated extrusive volcanism spanning over 50Ma, including three distinct phases of komatiitic eruptions, which has important implications for geological interpretation of this mineralised ultramafic system.

## **Cosmos Mine geology**

The Cosmos mine site lies on the western edge of the Agnew-Wiluna Greenstone Belt, which is part of the EGS, in the eastern part of the Yilgarn Craton. The Belt comprises of several, linear bimodal 'greenstone belt' sequences sandwiched between voluminous granitoid bodies, which were intruded between 2760-2620 Ma [2]. SHRIMP U-Pb zircon dating within the EGS indicates a major peak in volcanism between 2720-2650 Ma, with lesser peaks at 2950 Ma and 2810 Ma [2]. Current data indicates that majority of the ore-hosting komatiites in the eastern part of the Yilgarn Craton were deposited between 2713-2672 Ma, with 2707 Ma being the modal age for komatiite volcanism within the Kalgoorlie Terrane [1]. The mineralised Cosmos volcanic succession consists of a complex succession of three distinct ultramafic formations intercalated with fragmental and coherent extrusive lithologies, ranging from basaltic-andesites to rhyolites, as well as later-formed felsic intrusions [3]. The succession contains several high tenor nickel-sulphide ore bodies within a thick ultramafic package. Prior to this study no dating existed for this mineralised greenstone terrane.

## **U-Pb Dating of the Cosmos Succession**

SIMS U-Pb dating indicates that emplacement of the Cosmos succession took place between ~2736Ma and ~2653Ma, making it significantly older and longer-lived than many greenstone successions within the Kalgoorlie Terrane (Fig.1) [3]. Extrusive volcanism took place between 2736Ma and beyond 2685Ma, spanning ~50Ma, and featured three cycles of bimodal intermediate/felsic and ultramafic activity [3]. Periodic intrusive activity followed for a further ~32Ma (Fig.1) [3]. Thus, the volcanism that constructed this relatively small bi-modal greenstone succession lasted much longer than might be anticipated from stratigraphic considerations alone, an outcome that may have implications for other bi-modal volcanic successions in similar greenstone terranes [3].

In a regional context, the dating undertaken in this study strongly indicates that the Cosmos domain is separate from surrounding terranes, which was already considered to be the case due to the contrasting composition and geochemistry of the volcanic succession, as well as the style and tenor of nickel sulphide mineralisation [3]. The age of the footwall succession at Cosmos at 2736-2724Ma is ~15-25 Ma older than the span of felsic volcanism within the Kalgoorlie Terrane reported by [1] (2710–2665Ma). Therefore, the Cosmos felsic succession is appreciably older than the majority of the felsic rocks within the Kalgoorlie Terrane, particularly those successions in the southern part [3].

Overall the age, composition and geochemistry, in particularly the arc signature and absence of trondhjemite–tonalite–dacite (TTD) affinity [3], in the intermediate–felsic succession at Cosmos contrasts with much of the adjacent Agnew-Wiluna greenstone belt. This implies that the Cosmos succession is a separate, older terrane with a distinct extrusive volcanic succession, which formed in what appears to have been a long-lived, volcanic arc setting [3]. The age determinations obtained from the Cosmos succession demonstrate that high-resolution geochronology within individual greenstone successions can be achieved. It also creates new avenues for understanding and reconstructing Archean volcanic successions, particularly those where primary stratigraphic relationships have been obscured by regional deformation and metamorphism, and thus provides more robust platforms for interpreting the evolution of mineralized greenstone successions.

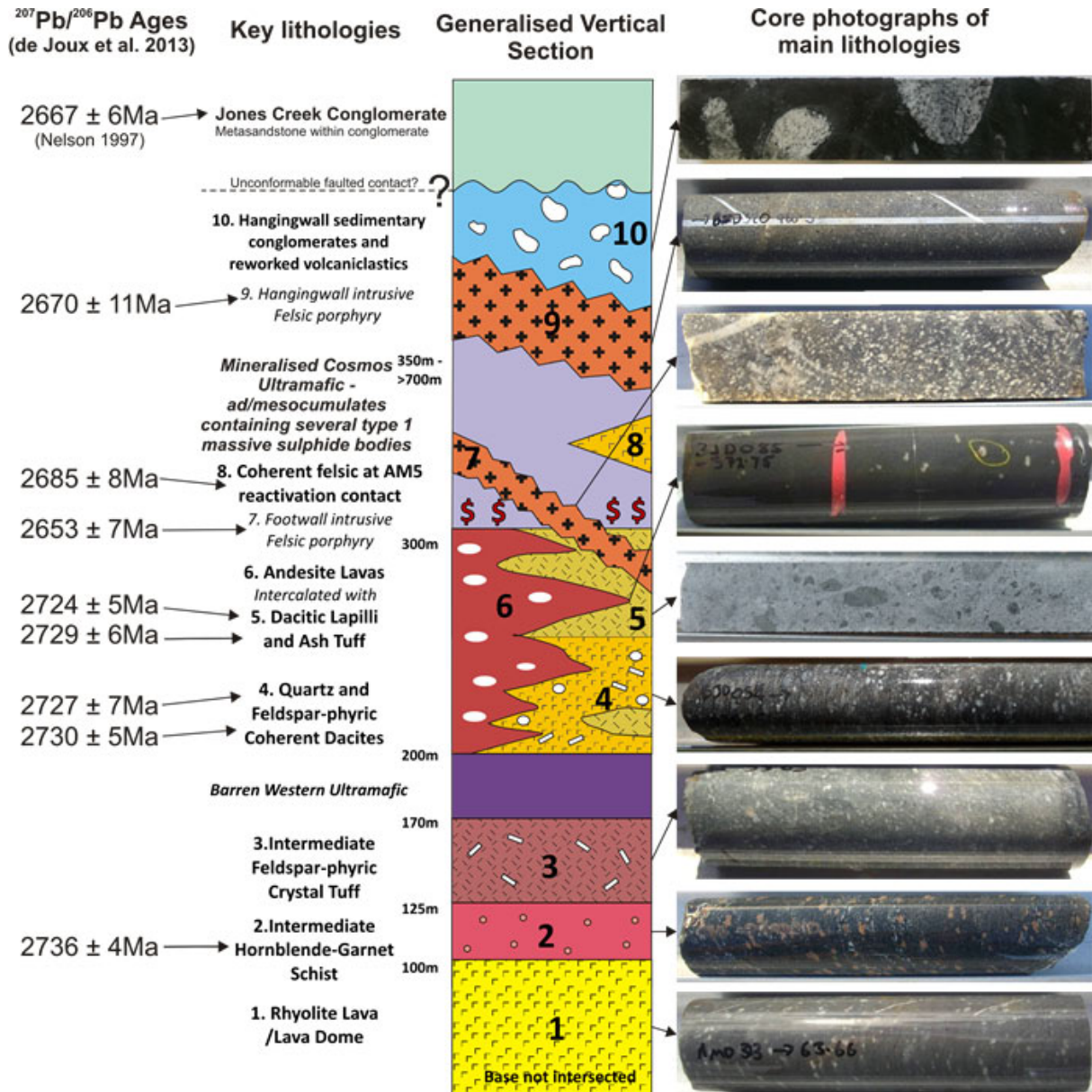


**Figure 1** GVS of the Cosmos Succession showing the key lithologies and their stratigraphic relationships including representative core photos of the main lithologies and the U-Pb dates obtained for several of the felsic lithologies. Ages shown are the average <sup>207</sup>Pb/<sup>206</sup>Pb for each sample [3].

## References

- [1] Kositcin et al. (2008) *Precambrian Research* **161**, 5-33
- [2] Cassidy et al. (2006) *Western Australia Geological Survey, Record* **2006/8**, 8
- [3] de Joux et al. (2013) *Precambrian Research*, in Review

# Metamorphic history of garnet-rich gneiss in Moldanubian Zone of the southern Bohemian Massif, inferred from inclusions and compositional zoning of garnet

T. Kobayashi<sup>1</sup>, S. L. Harley<sup>2</sup>, Y. Hiroi<sup>1</sup> & T. Hirajima<sup>3</sup>

<sup>1</sup>Department of Earth Sciences, Faculty of Science, Chiba University, 1-33, Yayoi-cho, Inage-ku, Chiba, 263-8522, JAPAN

<sup>2</sup>School of GeoSciences, University of Edinburgh, Edinburgh EH9 3JW, UK

<sup>3</sup>Department of Geology and Mineralogy, Graduate School of Science, Kyoto University, Kitashirakawaoiwake-cho, Sakyo-ku, Kyoto-shi, 606-8502, JAPAN

## Scientific Report

The Moldanubian Zone of the Bohemian Massif is a unique metamorphic belt, as both ultrahigh-pressure (UHP) and ultrahigh-temperature (UHT) metamorphic rocks are exposed together. The occurrences of UHP metamorphic rocks have been reported from several areas of the Moldanubian Zone [1-11]. Recently, multiple equilibrium stages were identified from Grt-rich gneiss at Ktiš in the Lhenice shear zone, located along the western margin of the Blanský les massif [12] (Fig 1). The characteristic matrix mineral assemblage of the Grt-rich gneiss is Crd+Sil+Bt+Grt±Spl with Qtz+Kfs+Pl. The coarse-grained Grts are commonly composed of dusty core and clear rim. The dusty core is defined by the alignment of fluid (CO<sub>2</sub>-N<sub>2</sub>) and micro-sized solid inclusions (Qtz, Kfs, Pl, Rt, Ap, Mnz and Zrn) of which outline are hexagonal in shape. Some coarse-grained (> 3 mm) Grts show chemical heterogeneity both in major and minor elements; Grs-content is homogeneous and high (Xgrs = 0.27) in an apparent core of the grain and continuously decreases towards the rim (Xgrs = 0.02). However, Prp-content shows an inverse pattern against Grs-content, i.e., Prp content is low and constant (Xprp = 0.03) in the core and gradually increases towards the rim (up to Xprp = 0.28). The outline of Grs and Prp content contours show symmetrical hexagonal shapes. Phosphorous (P)-content is almost below the detection limit of EPMA in the apparent core but it is high at the margin of the grain with local development of P-poor outermost rim. The outline of P-poor core shows a hexagonal shape, similar to that of Grs and Prp content contours. SIMS REE analyses revealed that P-content is low (17-315 ppm) in core of coarse-grained Grt and dramatically increase in the rim (742-1176 ppm). The geothermobarometry, based on the mode of occurrence of constituent minerals and the zoning pattern of Grt, depicts the following developing history of the host rock, such as a prograde stage defined by the assemblage of Grs-rich Grt core (Grs=27) + Pl (An<sub>11-15</sub>) under 1.5-2.3 GPa at 700-900 °C (Stage 1), a subsequent Grt-rim forming stage represented by Ca-poor Grt (Grs<sub>5</sub>) + Pl (An<sub>{12-19}</sub>) + Ky/Sil at 730-830 °C and 1.0-1.3 GPa (Stage 2), and a following decompression stage by the outermost rim of Grt (Grs<sub>2</sub>) + Sil + Crd ± Spl at 740-850 °C and 0.6-0.8 GPa (Stage 3) [12].

To evaluate ages of multiple equilibrium stages, chemical Th-U-Pb isochron method (CHIME) Mnz age dating was carried out for Grt-rich gneiss. Mnzs included in the core of Grt show bimodal grain size; coarse-grained (1 mm in diameter) and fine-grained (10 micrometer in diameter). Mnzs included in the rim of Grt have fine-middle grained size (10 micrometer to 0.5 mm in diameter). Mnzs in the matrix have middle-coarse grained size (0.5 mm to 3 mm in diameter). Most of middle-coarse grained Mnzs show a chemical zoning; relatively low Th constant in the core and high Th content in the rim. The Mnz grains included in the core of Grt give an average age of 337.2±4.2 Ma. The Mnz grains included in the rim of Grt give that of 336.5±5.1 Ma. The Mnz grains in the matrix give 334.9±3.9 Ma. Similar ages around 340 Ma are reported by U-Pb zircon ages of high-pressure granulite [13], [14] and [15] in the southern part of the Bohemian Massif. Furthermore, in-situ microanalysis (using SIMS U-Pb analyses) of 2-stage zircons within a garnet-kyanite-rutile leucogranulite at the Plešovice locality in the Bohemian Massif is consistent with zircon-garnet REE equilibration. Ti contents of 57-100 ppm in the first-stage oscillatory-sector zoned zircon indicate UHT conditions of 940-1022°C at 340.4±2.6 Ma. Overgrowth rinds have lower Ti contents, 31-38 ppm, that require lower-T but still granulite conditions of 863-887°C by 336.9±3.8 Ma [16] (Fig 2 and 3). These SIMS U-Pb age data are consistent with chemical Th-U-Pb isochron method (CHIME) Mnz age data from Grt-rich gneiss at Ktiš in the Lhenice shear zone.

These results suggest that the studied rock experienced very fast exhumation from stage 1 to stage 3. Furthermore, feldspar inclusions are found from the core and rim of coarse-grained Grt. Feldspar inclusions are composed mainly of micrometre- to submicrometre-scale spherulitic and granophyric intergrowths

of quartz and feldspar (alkali feldspar or plagioclase). These features of the inclusions are similar to those of "nanogranites" which are felsic inclusions enclosed within Grt in high- to ultrahigh-temperature pelitic migmatites and/or granulites as reported by Cesare et al. (2009) and Hiroi et al. (2010) ([17] and [18]). Cesare et al. (2009) ([17]) concluded that nanogranites are the crystallized anatectic melts which were trapped by peritectic minerals growing during partial melting. The felsite inclusions in this study suggest that partial melts formed during early high-pressure metamorphic stage (stage 1) and trapped by garnet have undergone nonequilibrium crystallization under specific conditions of continuous rapid cooling.

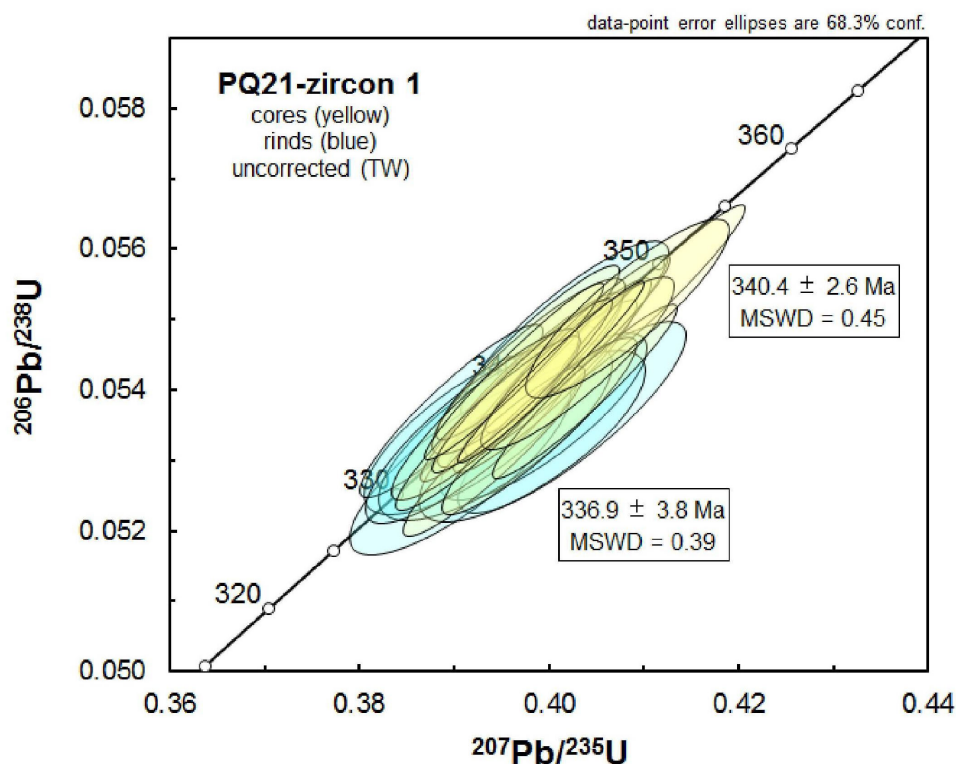


Figure 3. Concordia diagrams showing ion microprobe (CAMECA1270) at the University of Edinburgh analyses of zircons from Plesovice locality, South Bohemia. Error ellipses are depicted at the  $1\sigma$  level.

## References

- [1] H. Becker and R. Altherr (1992) *Nature* **358**, 745-748.
- [2] H. Becker (1996) *Journal of Petrology* **37**, 785-810.
- [3] J. Kotková et al. (1997) *European Journal of Mineralogy* **9**, 1017-1033.
- [4] S. Vrána and J. Fryda (2003) *European Journal of Mineralogy* **15**, 1, 43-54.
- [5] D. Nakamura et al. (2004) *Journal of Metamorphic Geology* **22**, 593-603.
- [6] T. Kobayashi et al. (2008) *Journal of Mineralogical and Petrological Sciences* **103**, 105-111.
- [7] S. W. Faryad (2009) *Lithos* **109**, 193-208.
- [8] K. Naemura et al. (2009a) *Journal of Petrology* **50**, 1795-1827.
- [9] K. Naemura et al. (2009b) *Journal of Mineralogical and Petrological Sciences* **104**, 168-175.
- [10] K. Naemura et al. (2011) *Ultrahigh-Pressure Metamorphism: 25 Years After the Discovery of Coesite and Diamond*, 77-111.
- [11] J. Kotková et al. (2011) *Geology* **39**, 667-670.
- [12] T. Kobayashi et al. (2011) *Lithos* **124**, 46-65.
- [13] M. Aftalion et al. (1989) *Neues Jahrbuch für Mineralogie-Monatshefte* **4**, 145-152.
- [14] A. Kröner et al. (2000) *Contributions to Mineralogy and Petrology* **138**, 127-142.
- [15] J. Sláma et al. (2008) *Chemical Geology* **30**, 1-35.
- [16] T. Kobayashi et al. (2013) *Japan Geosci Union Meeting 2013:SCG07* submitted.
- [17] B. Cesare et al. (2009) *Geology* **37**, 627-630
- [18] Y. Hiroi et al. (2010) *The 30th Symposium on Polar Geosciences, -Solid earth dynamics explored from polar regions- 2010 National Institute of Polar Research, GO016*.

# The evolution of mid-ocean ridge magma chambers and the growth of slow-spreading oceanic crust

C.J. Lissenberg<sup>1</sup>

<sup>1</sup>School of Earth and Ocean Sciences, Cardiff University, Main Building, Park Place, Cardiff CF10 3AT, UK

## Introduction

The generation of oceanic crust plays a significant role in Earth evolution. Melt production in the mantle contributes considerably to planetary differentiation, facilitating transfer of mass from the mantle to the crust. Rising mantle and magma also transport heat from the Earth's interior to the oceans, accounting for a significant part of the Earth's heat loss. This heat drives hydrothermal circulation, which in turn provides energy to sustain complex ecosystems.

Much information about the heat and mass transfer associated with oceanic crustal accretion is contained in the plutonic lower crust. Its gabbroic building blocks record a history of magma emplacement, element fractionation, hydrothermal circulation and crustal cooling. However, reconstructing this record has proven challenging. As a result, several fundamental aspects have remained unclear. Arguably the most important but least well constrained among these is the temporal evolution of magma chambers: How long are magma chambers active? How quickly do they cool? How do they evolve over time? These are key factors controlling the architecture of the oceanic lithosphere, and are critical parameters for the thermal evolution of the ridge axis and the resulting hydrothermal system. This research project is designed to address these questions.

## Approach

Zircon is a common accessory mineral in oceanic gabbroic rocks, forming during late-stage crystallisation in oceanic magma chambers from evolved melts generated by the fractionation of mid-ocean ridge basalt. Studying samples from the Vema Lithospheric Section (11°N, Mid-Atlantic Ridge), we recently found that different zircon grains within the same sample (up to 9 single grains were analysed for each sample) had ages that varied beyond the analytical uncertainty [1]. The rationale behind the project is to exploit the range in dates present within individual samples from the Vema Lithospheric Section to document the temporal evolution of mid-ocean ridge magma chambers. This will be achieved by combining zircon trace element analyses with high-precision single crystal U-Pb geochronology.

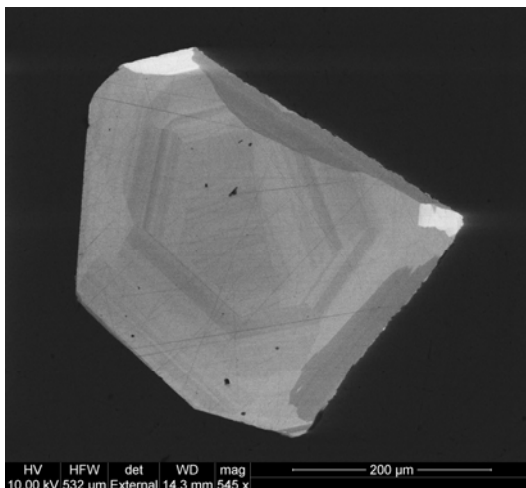


**Figure 1:** CL image of zircon from sample S1904-03, showing sector and oscillatory zoning.

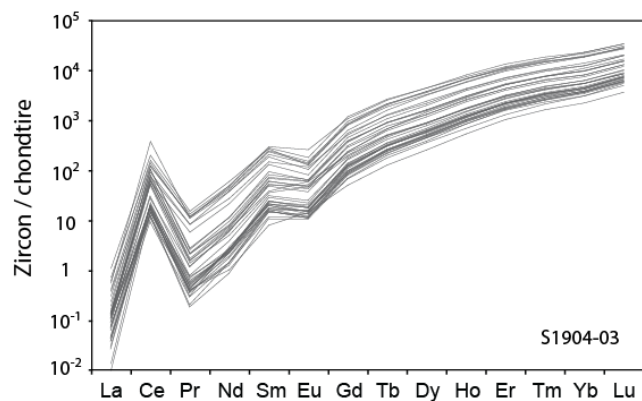


**Figure 2:** Chondrite normalised REE patterns of zircon from sample S1904-03.

## Results

The IMF component of the project comprised analysing the trace element compositions of Vema zircons. In total, 74 Vema zircons from 5 samples were analysed using the ims-4f. The internal textures of the zircons are dominated by sector zoning, with lesser amounts of oscillatory zoning, as is typical for oceanic zircon (Figure 1). They generally preserve a single stage of growth, although some grains contained distinct textural domains. The ion microprobe data revealed trace element patterns typical for igneous zircon (Figure 2). In addition, the U/Yb-Y relationships (Figure 3) are typical for zircons formed in a mid-ocean ridge environment [2]. This argues against the presence of recycled continental zircon in Mid-Atlantic Ridge gabbros, as has been proposed (e.g., [3]). Nonetheless, there was considerable variation in trace element composition between different grains from the same sample; for example, Y concentrations varied by a factor of 29 in sample S1904-03 (Figures 2, 3). These variations correlate with Ti – which is a proxy for temperature - with Ti varying by 20 ppm. This range in Ti corresponds to a range in crystallisation temperatures of the zircon grains of  $\sim 175^{\circ}\text{C}$  [4]. The trace element analyses thus revealed that zircon crystallisation in each of the individual samples spanned a considerable temperature range, and that melt composition varied accordingly. This is in keeping with the prediction of Lissenberg et al. [1], who argued that the range in dates found in the Vema samples represented crystal growth from cooling and evolving melts.

The next step in the project, which is ongoing, is to perform high-precision TIMS dating on selected Vema zircons spanning the full range of trace element concentrations, to establish how the crystallisation temperature and melt chemistry varied over time. The combined data will allow us to resolve a long-standing issue: how oceanic magma chambers evolve over time.

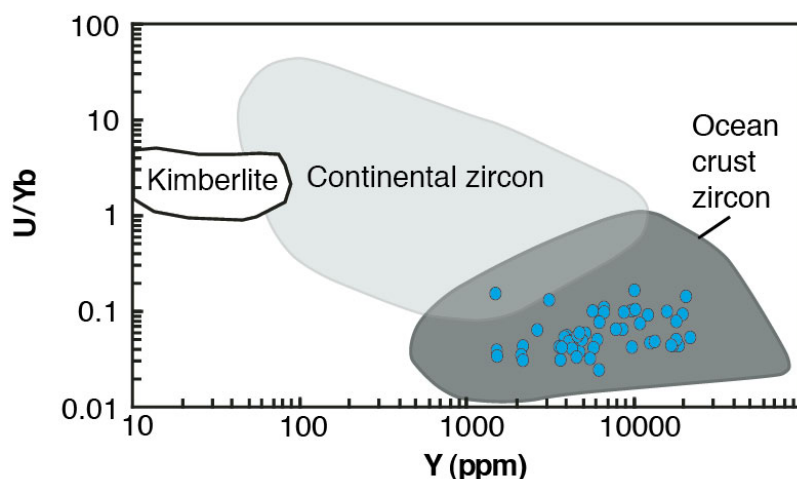


**Figure 3:** U/Yb vs. Y discrimination diagram [2] shows that trace element compositions of zircon grains from sample S1904-03 are typical for oceanic zircon.

## References

- [1] C.J. Lissenberg et al. (2009) *Science* **223**, 1048-1050
- [2] C.B. Grimes et al. (2007) *Geology* **35**, 643-646
- [3] J. Pilot et al. (1998) *Nature* **393**, 676-679
- [4] J.M. Ferry and E.B. Watson (2007) *Contributions to Mineralogy and Petrology* **154**, 429-437.

# Quantifying the dynamics of bubble growth in magma using SIMS profiling of water content in glass

E. Llewellyn<sup>1</sup>, I. McIntosh<sup>1</sup>, M. Humphreys<sup>2</sup>, A. Burgisser<sup>3</sup> & C.I. Schipper<sup>3</sup>

<sup>1</sup>Department of Earth Sciences, Durham University, Durham DH1 3LE, UK

<sup>2</sup>Department of Earth Sciences, University of Oxford, Oxford OX1 3AN, UK

<sup>3</sup>Institut des Sciences de la Terre d'Orléans, CNRS – l'Université d'Orléans, 1A rue de la Férellerie, 45071 Orléans Cedex 2, France.

## Introduction

Volcanic eruptions are driven by the nucleation and growth of bubbles, the rate and extent of which are key controls on the explosivity of the eruption, and thus the volcanic hazard. H<sub>2</sub>O exsolution is particularly important since it is the most abundant volatile and strongly influences melt viscosity. The interplay of H<sub>2</sub>O concentration in the melt, H<sub>2</sub>O diffusivity, and melt viscosity determines bubble growth and modifies the H<sub>2</sub>O concentration profile in the melt surrounding the bubble. This concentration profile is preserved when the melt is quenched to glass, providing a tool for investigating bubble growth dynamics and reconstructing eruption mechanisms.

## Approach

Both experimental and natural samples were analysed. Experimental samples were synthetic vesicular phonolite and rhyolite glasses, created with a range of initial water contents and decompressed under known pressure and temperature conditions. H<sub>2</sub>O was the only volatile phase present; thus bubble growth was governed by the exsolution and diffusion of H<sub>2</sub>O through the melt. Natural samples included basaltic pyroclasts from a submarine eruption and a vesicular glassy rind of a phonolite lava bomb. Secondary Ion Mass Spectrometry (SIMS) measurements were made of the H<sub>2</sub>O concentration along radial profiles extending from bubble walls. These SIMS spot analyses were then used to calibrate greyscale variations in backscatter scanning electron microscope (BSEM) images of the sample using the technique of [1]. Using this technique we extracted quantitative H<sub>2</sub>O concentration profiles at a high spatial resolution (resolution of a pixel, ~0.5µm, cf ~10µm SIMS spot size) (Fig. 1).

## Results and Interpretation

All bubbles in experimental samples were found to have higher H<sub>2</sub>O concentrations adjacent to the vesicle walls than in the far-field. In BSEM images, this effect is seen as dark halos surrounding vesicles (Fig 1). The SIMS-calibrated H<sub>2</sub>O concentration gradients are steepest at the vesicle wall and decay away to the lowest values over the order of tens of microns from the vesicle wall (Fig. 2). Similar concentration profiles were also found around vesicles in naturally erupted samples. These profiles show that the bubbles were resorbing at the time that the concentration profiles were formed.

H<sub>2</sub>O concentration at a bubble wall will be the equilibrium solubility of H<sub>2</sub>O in the melt at the given pressure and temperature conditions. The observed H<sub>2</sub>O concentrations at the bubble wall are as much as 3 wt% higher than expected for the final experimental conditions. H<sub>2</sub>O solubility increases with increasing pressure and/or decreasing temperature. The well-constrained experimental samples allow us to rule out a possible pressure cause; instead the observed profiles were formed as H<sub>2</sub>O solubility increased during quench to ambient temperature.

## Implications

This previously unrecognised bubble resorption during quench has important implications for both experimental studies and the interpretation of naturally erupted products. Final bubble volumes and sample porosities are commonly used to make inferences about degassing processes, yet quench resorption can reduce observed bubble volumes by as much as a factor of two. A recent study of naturally erupted samples interpreted similar H<sub>2</sub>O gradients around vesicles as evidence of repressurisation in the conduit prior to eruption [2]. While this is plausible, such a mechanism would be unusual whereas all samples must cool on eruption. Our observations of resorbing bubbles in both experimental and natural samples highlight the importance of distinguishing between pressure increase and temperature decrease when using such gradients to interpret natural samples.

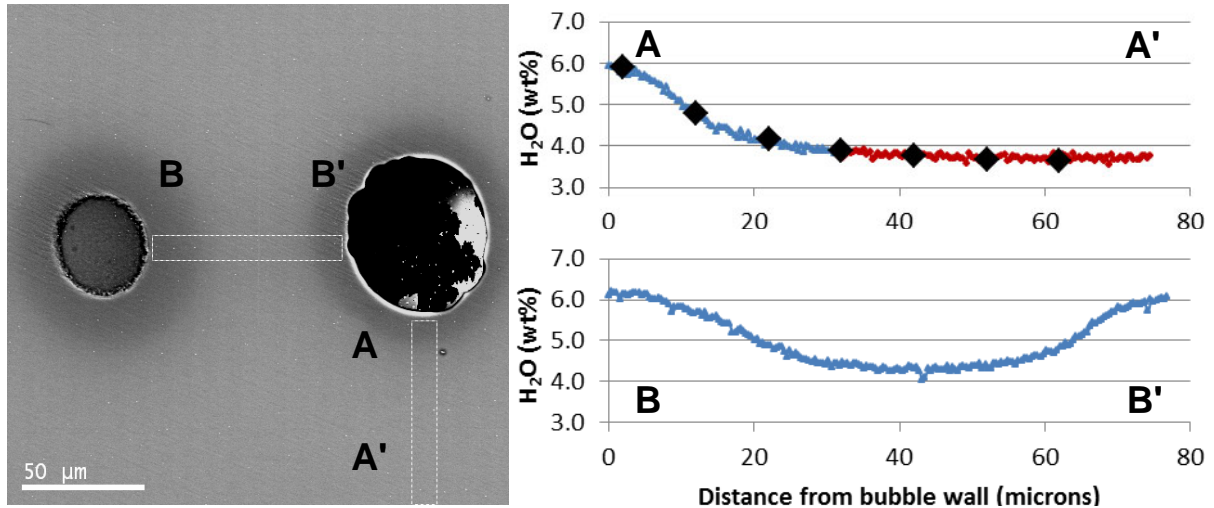


**Figure 1.** *Left:* BSEM image of bubbles in phonolite glass showing analysed profiles A - A' (SIMS and greyscale intensity) and B - B' (greyscale intensity only). Note bright white edge effect at bubble walls. *Right top:* H<sub>2</sub>O concentrations extracted from BSEM greyscale image (blue triangles) along profile A - A' with points measured by SIMS (black diamonds) for comparison. *Right bottom:* H<sub>2</sub>O concentrations extracted from BSEM greyscale image along profile B - B' using the SIMS-calibration of greyscale intensity derived from profile A. Blue sections highlight rehydration during bubble resorption; red sections result from syn-experimental bubble growth.

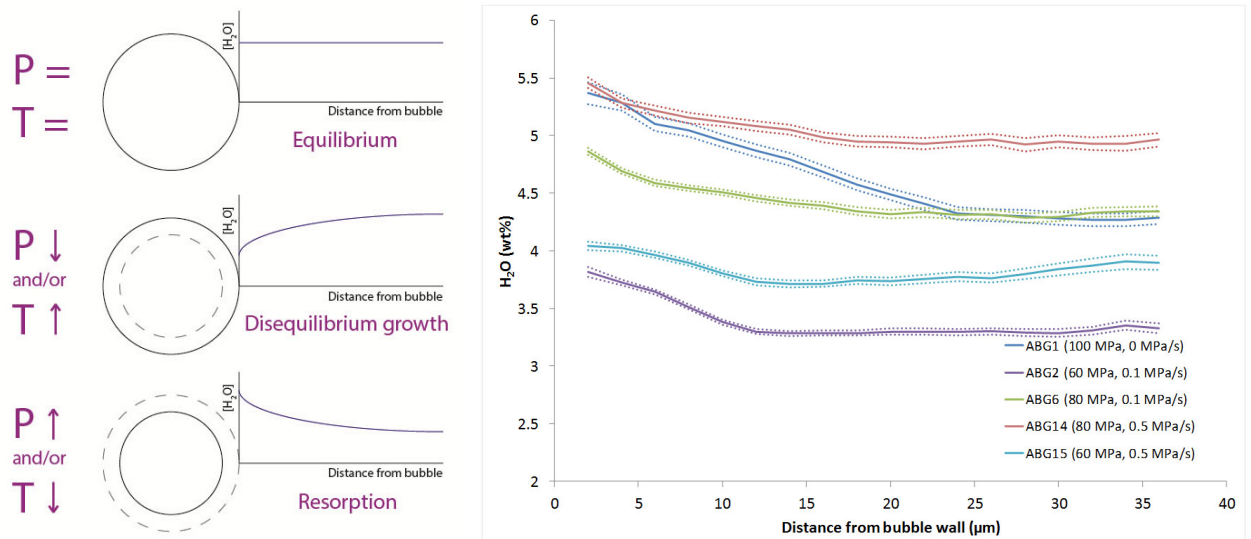


**Figure 2.** *Left:* Relationship between pressure and temperature (P, T) conditions, bubble growth and corresponding concentration profiles. H<sub>2</sub>O concentration at bubble wall is always equilibrium solubility for the given P, T conditions. At constant P and T, bubble is in equilibrium with melt and concentration profile is flat. If P decreases and/or T increases, H<sub>2</sub>O solubility decreases and bubble grows as H<sub>2</sub>O diffuses down concentration gradient towards bubble wall. If P increases and/or T decreases, H<sub>2</sub>O solubility increases and H<sub>2</sub>O re-enters melt at bubble wall and diffuses down gradient back into melt. *Right:* Concentration profiles (averaged from all measured profiles around multiple vesicles) for five experimental rhyolite samples. All show increasing H<sub>2</sub>O towards the vesicle wall.

### Use of Results

I.M. McIntosh et al (2013) (Mis)understanding bubble growth in magma: Evidence from preserved volatile concentration gradients in glass *Volcanic and Magmatic Studies Group* (Jan 2013)

I.M. McIntosh et al (2012) (Mis)understanding bubble growth in magma: Evidence from preserved volatile concentration gradients in glass *European Geosciences Union* (Apr 2012)

### References

- [1] M.C.S. Humphreys et al. (2008) *Earth and Planetary Science Letters*, 270, 25-40
- [2] J.M. Watkins et al (2012) *Geology*, 40, 699-702

# Organogenic dolomite and Neoproterozoic chemostratigraphy

McMillan, E.A<sup>1</sup> & Bonnand, P<sup>2</sup>.

<sup>1</sup>School of Geography, Earth and Environmental Sciences, University of Birmingham, Edgbaston, B15 2TT

<sup>2</sup>Department of Earth Sciences, South parks Road, Oxford, OX1 3AN

**Introduction:** This work formed part of NERC Standard Grant *The Svalbard Exemplar of Neoproterozoic Glaciation* which aimed to develop a robust understanding of the nature of earth surface systems during extreme Neoproterozoic glaciation in NE Svalbard. To date, whole rock analysis has been used to try to understand the diagenetic history of Neoproterozoic dolomites using C and O isotope data [1]. This however does not take into account the chemical zoning within individual dolomite grains. The specific objective was to generate a chemical model for the origin of the dolomite and explore the implications for Neoproterozoic chemostratigraphy. Our aim was to produce paired trace element and  $\delta^{13}\text{C}$  micro-analyses to identify trends corresponding to progressive bacterial reactions. Five samples of Neoproterozoic carbonate from NE Svalbard were selected for trace element analyses. All samples were collected from within the McDonaldryggen Member (E3) of the Elbobreen Formation, which forms part of the Polarisbreen Group at Dracoisen, NE Svalbard. The McDonaldryggen Member is a ~200m thick succession of cyclic dolomitic shale and concretionary dolomite that forms part of a shallowing upwards sequence between two glacial deposits, the Petrovbreen Member (E2) below and the overlying Wilsonbreen Formation (Figure 1).

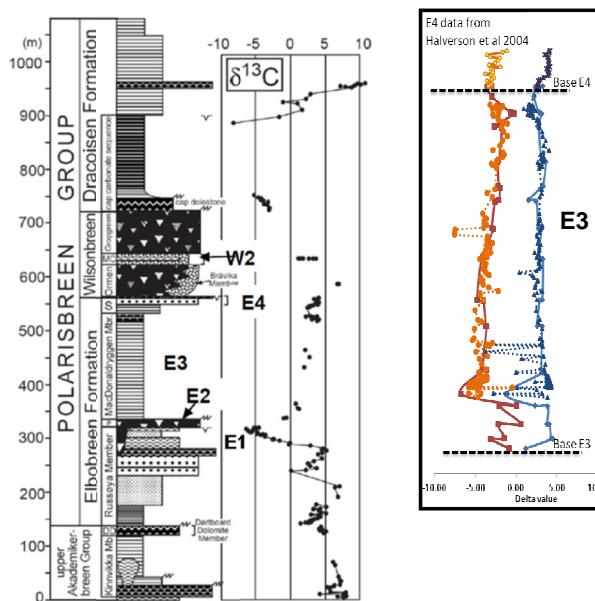


**Figure 1.** Stratigraphic section [1] showing the position of the McDonaldryggen Member (E3) within the Cryogenian of NE Svalbard. Glacial deposits E2 and the Wilsonbreen Formation are indicated. Our unpublished data (inset) indicate relatively consistent, positive  $\delta^{13}\text{C}$  (blue curve) throughout E3.

**Analyses:** Twenty grains were targeted in each of the five samples from E3. This report focuses on two end member samples, F7163 and F7266. These represent concretionary dolomite and dolomitic shale (Figure 2) and are located at 42m and 173m respectively above the base of E3.

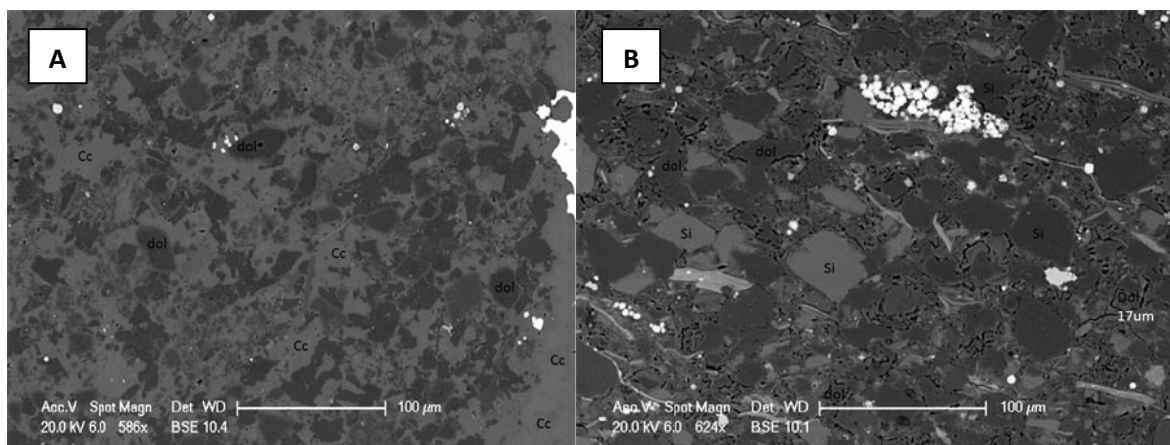


**Figure 2.** Backscatter SEM images of F7163 (A) and F7266 (B) illustrating the textural features of (A) concretionary dolomite and (B) dolomitic shale. Cc - Calcite; dol - Dolomite; Sil - Silicate.

Identification of mineral phases based on shape and backscatter intensity was not straightforward in these samples therefore EDS X-Ray analysis was required to identify the mineral phase of selected grains (Figure 2). The identification of dolomite grains once the samples were in the vacuum chamber was extremely difficult making locating grains of interests as identified using backscatter SEM virtually impossible. As a result areas of dolomite were identified by scanning for Ca - grains that showed low intensity for Ca but high for Mg were selected for analysis. However there was no way of knowing that the targeted grains were zoned at all. At each analysis point 20 steps were done at 5 $\mu$ m intervals into the sample with the aim of generating a trace metal profile through the grain as opposed to laterally across the surface. Based on the crystal size seen in thin section the depth to which the analyses were taken is greater than the thickness of one individual crystal therefore step scan traces will represent inter-crystal chemical variation.

**Results:** Figure 3 provides a summary of Mg concentration variation with depth from the surface of the samples. There does not appear to be any systematic variation that would suggest chemical zoning within the grains. The greater range in Mg concentration in the concretionary dolomite is indicative of the textural nature of the sample. It may also be a result of the beam overlapping between calcite and dolomite grains. No calcite grains were analysed in sample F7266.

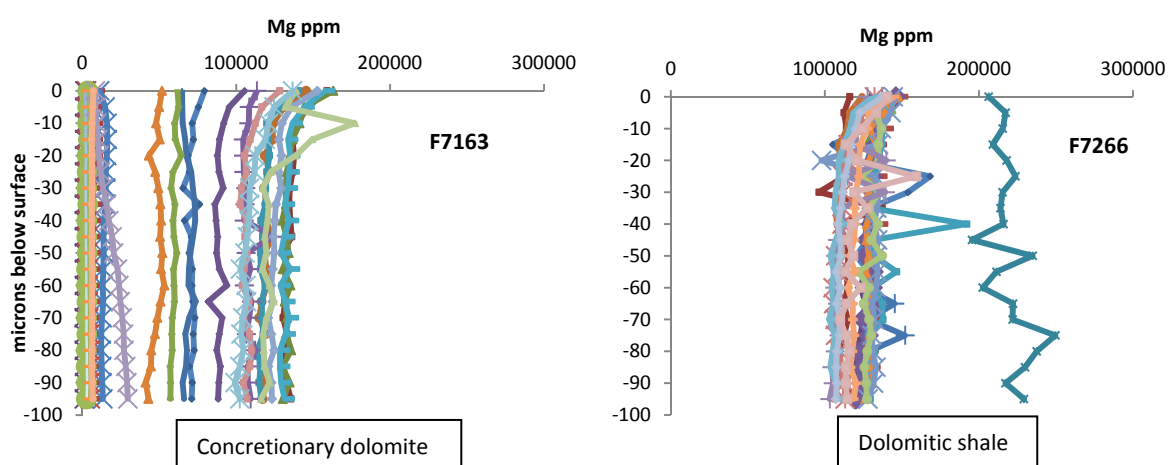


**Figure 3.** Mg ppm variation with depth in each dolomite grain selected in samples F7163 and F7266.

Problems with grain size and spot diameter meant that chemical zoning of dolomite could not be defined using this method and therefore we are unable at present to build a geochemical model for the diagenetic history of these carbonates. Variations in current, spot size etc. were tried but spatial resolution was still a problem. Unfortunately the results of this work mean that the initial aim of using the ion microprobe technique to produce paired  $\delta^{13}\text{C}$  – trace metal analyses to investigate diagenetic history of these carbonates is unfeasible. The small size of the dolomite grains, combined with the presence of impurities within them, mean that these samples are not suitable for  $\delta^{13}\text{C}$  analyses using the Cameca-1270 as intended. This technique requires a beam with diameter 30 $\mu$ m which is too large to reliably target one single, clean dolomite grain.

## References

- [1] G.P. Halverson et al. (2004) Basin Research **16**, 297-324

# The hydrothermal history of British Devonian granites: Insights from zircon, quartz and whole-rock oxygen isotope compositions

Andrew Miles<sup>1</sup>, Colin Graham<sup>1</sup>, Martin Gillespie<sup>2</sup>, Chris Hawkesworth<sup>3</sup> and Richard Hinton<sup>1</sup>

<sup>1</sup>School of GeoSciences, West Mains Road, University of Edinburgh Edinburgh, EH9 3JW, UK

<sup>2</sup>British Geological Survey Murchison House, West Mains Road, Edinburgh, EH9 3LA, UK

<sup>3</sup>School of Geography and Geosciences, University of St Andrews, North Street, St Andrews, KY16 9AL, UK

## Introduction

The oxygen isotope composition ( $\delta^{18}\text{O}$ ) of magmas and their resultant rocks may be controlled by a variety of processes including the compositions of source rocks, fractional crystallisation, water contents, exchange with magmatic fluids and post-solidus hydrothermal alteration [1]. Whole-rock (WR) compositions represent the cumulative effects of some or all of these processes and it has proved difficult to distinguish their individual actions. Zircon provides a robust and reliable archive of magmatic compositions at the time of crystallisation and is largely immune from the effects of post-solidus exchange that modify WR analyses and those of less robust minerals such as feldspar [2]. Integrated studies that combine the  $\delta^{18}\text{O}$  compositions of zircon, WR and coexisting minerals therefore provide a valuable means of examining magmatic equilibration, re-equilibration and post-magmatic alteration. The magmatic and hydrothermal histories of granites from the Devonian Trans-Suture Suite (TSS) in Northern Britain are examined and compared to those from the British Tertiary Igneous Province (BTIP) using the  $\delta^{18}\text{O}$  compositions of zircon, quartz and their respective WR. Their compositions are used to reveal fundamentally different hydrothermal histories and processes that reflect contrasting tectonic environments, source compositions, emplacement depths and assembly times.

## Results and Discussion

Zircon  $\delta^{18}\text{O}$  compositions in two Devonian calc-alkaline TSS granites in Scotland preserve magmatic  $\delta^{18}\text{O}$  compositions that are mostly out of isotopic equilibrium with the  $\delta^{18}\text{O}$  compositions of their whole-rocks and co-existing quartz (Figure 1). The latter two archives have elevated  $\delta^{18}\text{O}$  compositions that suggest hydrothermal alteration and exchange related to the circulation of  $^{18}\text{O}$ -rich magmatic fluids with no detectable input from  $^{18}\text{O}$ -depleted meteoric water. Larger degrees of disequilibrium in the outer zones of the two plutons reflect additional fluid exchange with local  $^{18}\text{O}$ -rich sedimentary rocks. By contrast, the hydrothermal history of the mostly tholeiitic British Tertiary Igneous Province (BTIP) is characterised by low  $\delta^{18}\text{O}$  compositions ( $<5.3\%$ ) related to circulation of meteoric water and assimilation of local  $^{18}\text{O}$ -depleted rocks [3]. These differences result from fundamentally different hydrothermal histories that reflect different tectonic environments, mantle conditions and emplacement depths. Meteoric water circulation (if any) around the TSS plutons is likely to have been limited or excluded by deeper emplacement (4 to 6 km [4]; BTIP: 1 to 2 km), emplacement into metasediments with low permeability and reduced thermal potential related to protracted and incremental pluton assembly. The water-rich magmas of the TSS, that determine their calc-alkaline compositions, reflect derivation in part from previously hydrated mantle.

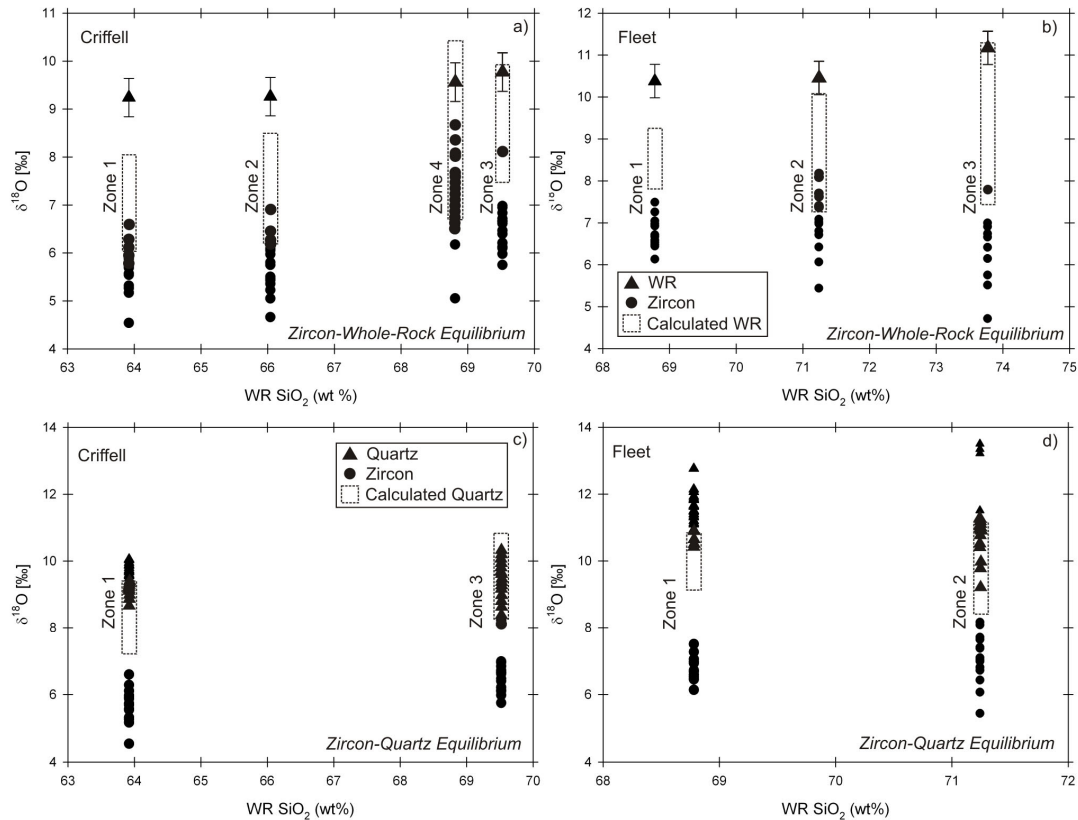


**Figure 1** Assessment of oxygen isotopic equilibrium between zircon, whole-rock (WR) and quartz. ‘Calculated WR’ and ‘calculated quartz’ compositions have been calculated using the equations of [5] and [6] respectively. Temperatures calculated from Ti-in-zircon thermometry [7]. Zircon in zones 1 and 2 of the Criffell pluton and zone 1 of the Fleet pluton are out of oxygen isotope equilibrium with the WR, while in zones 3 and 4 of the Criffell pluton and zones 2 and 3 of the Fleet pluton, only the most  $^{18}\text{O}$ -rich zircon compositions are in isotopic equilibrium with their respective WR. Measured WR compositions appear too high to be in equilibrium with their zircons and may reflect alteration and exchange of the WR related to hydrothermal fluids derived from local  $^{18}\text{O}$ -rich sediments. Similar results are noted for quartz, with only the most  $^{18}\text{O}$ -rich zircons in equilibrium with co-existing quartz. While this may reflect crystallization from different magmas, isotopic heterogeneities within quartz crystals indicate that they may also have been affected by hydrothermal exchange related to fluids exchanged with local  $^{18}\text{O}$ -rich sediments.

## References

- [1] J.M. Eiler (2001) *Reviews in Mineralogy* **43**, 319-364.
- [2] J.W. Valley (2003) *Reviews in Mineralogy* **53**, 343-380.
- [3] J.W. Valley and C.M. Graham (1996) *Contributions to Mineralogy and Petrology* **124**, 225-234.
- [4] A.J. Miles et al. (2013) *Contributions to Mineralogy and Petrology* (in press).
- [5] J.W. Valley (2005) *Contributions to Mineralogy and Petrology* **150**, 561-580
- [6] J.W. Valley et al. (2003) *Geochim Cosmochim Acta* **67**, 3257-3266
- [7] J.M. Ferry and E.B. Watson (2007) *Contributions to Mineralogy and Petrology* **154**, 429-437

# Megacrysts and conduit dynamics at Erebus volcano

Yves Moussallam<sup>1,3</sup>, Clive Oppenheimer<sup>1,3</sup>, Bruno Scaillet<sup>3</sup>, Phil Kyle<sup>2</sup>

<sup>1</sup>Department of Geography, University of Cambridge, Downing Place, Cambridge, CB2 3EN, UK

<sup>2</sup>Department of Earth and Environmental Science, New Mexico Tech., 801 Leroy Place, Socorro, NM 87801, USA

<sup>3</sup>ISTO, UMR 6113 Université d'Orléans-CNRS, 1A rue de la Férollerie, 45071 Orléans cedex 2, France

## Background and objectives

Erebus, the world southernmost active volcano, is the only presently-erupting phonolite volcano. Its long-lived anorthoclase phonolite lava lake and sustained degassing (Giggenbach et al., 1973) provide uncommonly favourable circumstances for direct measurement of the magmatic system. Several features distinguish Erebus: the decadal persistence of the lava lake; episodic Strombolian activity at the lava lake (Aster et al., 2008), which provides samples for analysis; and the abundance of megacrysts (up to 10-cm-long) of anorthoclase feldspar in the lava lake. The longevity of the lava lake implies counterflow of vesicular and degassed magma within the (<10 m) feeder conduit (Oppenheimer et al., 2009). Flow instabilities and diffusional processes allow complex transfers of gas, melt and crystals up and down the conduit (e.g., Witham, 2010). Recent physical modeling of the Erebus plumbing system (Molina et al., 2012) suggests that crystals are predominantly carried with the melt (caught up in the convecting system), and that a large fraction of the crystals define convection cycles within the lava lake (~10 days) and within the magma chamber (~1 day). This raises the question as to whether the strikingly-zoned and melt-inclusion rich anorthoclase megacrysts might thereby yield valuable insights into physical and chemical processes occurring during magma transport in the conduit. The petrology and geochemistry of the Erebus phonolites is well-characterised (e.g., Kyle et al., 1992; Kelly et al., 2008) and we have modelled the melt inclusion suite for the entire Erebus Lineage (Oppenheimer et al., 2011). The key question we pose here is, thus: what do the megacrysts tell us about magma supply and storage, volatile behaviour, and the interplay of conduit vs lava lake processes? To address this, we obtained highly spatially-resolved measurements of volatile contents of anorthoclase-hosted melt inclusions.

## Additional background results

Seven anorthoclase megacrysts were imaged by high resolution x-ray tomography in order to ensure that all melt inclusions were isolated from each others and the exterior (Figure 1).

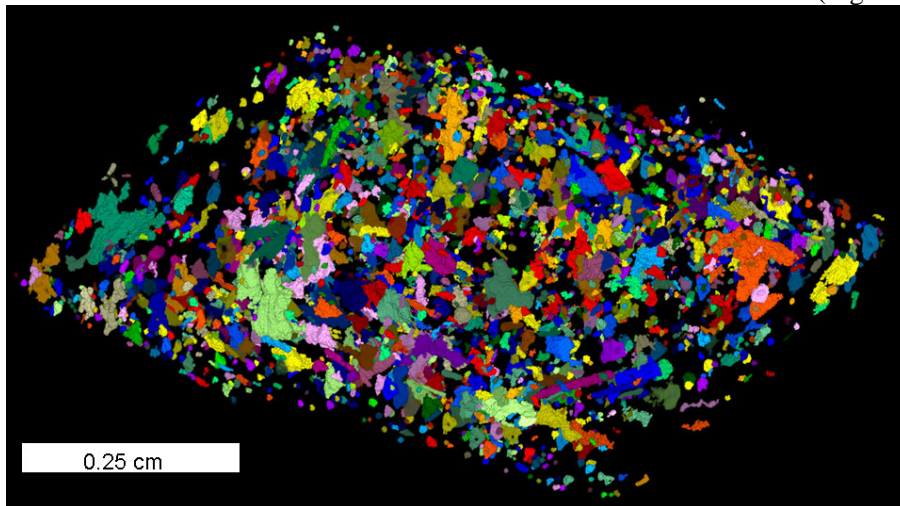


Figure 1: 3D tomographic image of melt inclusions within an 0.5 cm thick slice of an anorthoclase megacrystal (erupted in 2005). Each melt inclusion is colored using a particle analyzer algorithm which identify connection in a 3D network (the same color might be used for several melt inclusions). Voxel size is 6 $\mu$ m.

Megacrystals which were found to contain melt inclusions isolated from each other were sliced, polished and high resolution x-ray maps were acquired to reveal the crystal zonation (Figure 2b and c). Phase equilibrium experiments at a range of pressure from 1000 to 1 bar recreated the range of natural compositions suggesting a composition dependence to pressure (Figure 2a).

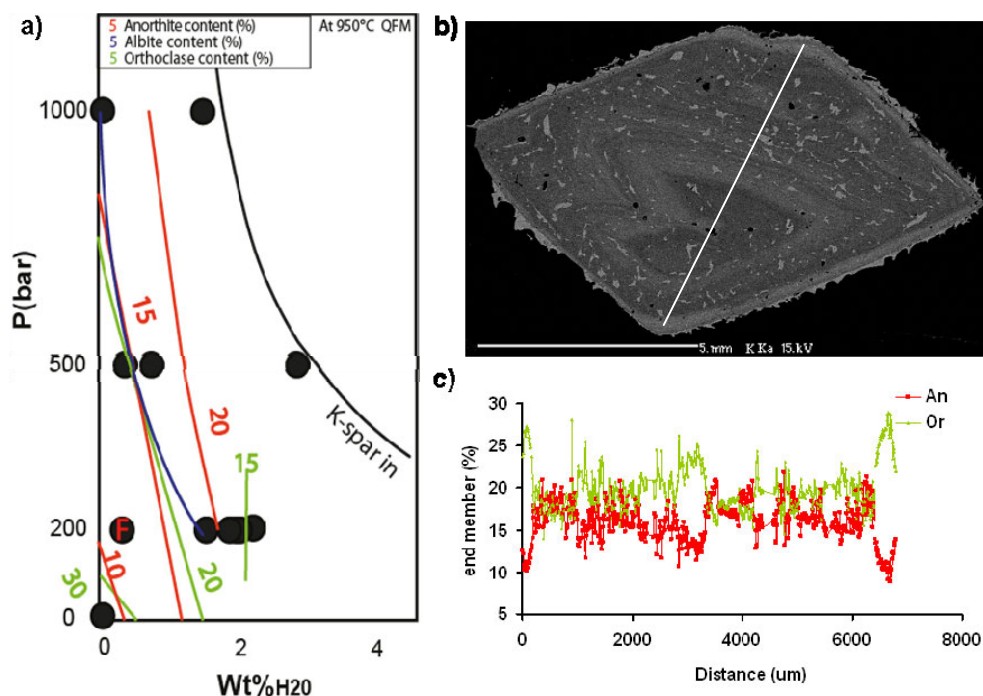


Figure 2: **a)** Isothermal/polybaric anorthoclase composition within Erebus phonolite at 950°C and  $\log(fO_2)$  near QFM for pressure up to 100 MPa. The black line shows the first appearance of potassium feldspar in the system. The blue line represent the 60% albite isopleth, the red lines represent the anorthite isopleths and the green lines the orthoclase isopleths. **b)** Potassium X-Ray maps of an anorthoclase section in which both zoning and melt inclusions are clearly visible. **c)** Electron microprobe transect (location show in figure 2b) of an anorthoclase crystal showing the chemical variation in term of anorthite (red line) and orthoclase (green line) end members.

In order to test the hypothesis that the anorthoclase compositional zoning is a direct record of the various pressure (and hence depth) at which they grew we measured the volatile content (H<sub>2</sub>O; CO<sub>2</sub>; SO<sub>2</sub>; Cl; F) of melt inclusions enclosed within each zone to model their (compositionally-dependent) saturation pressures, and thereby constrain their entrapment depths.

### Preliminary results

A total of about 75 anorthoclase-hosted melt inclusions were analysed from six megacrystals. Figure 3 shows the CO<sub>2</sub> content of 19 melt inclusion and 3 analysis of glass directly in contact with the rim of the megacrystal shown in Figure 2b plotted against the greyscale value of the pixel directly surrounding the inclusion in the potassium x-ray map. The greyscale value of the pixels is a proxy for the potassium content of the zone in which each melt inclusion is enclosed. Figure 3 shows a clear correlation between the CO<sub>2</sub> content of a melt inclusion and the potassium content of the anorthoclase zone enclosing it.

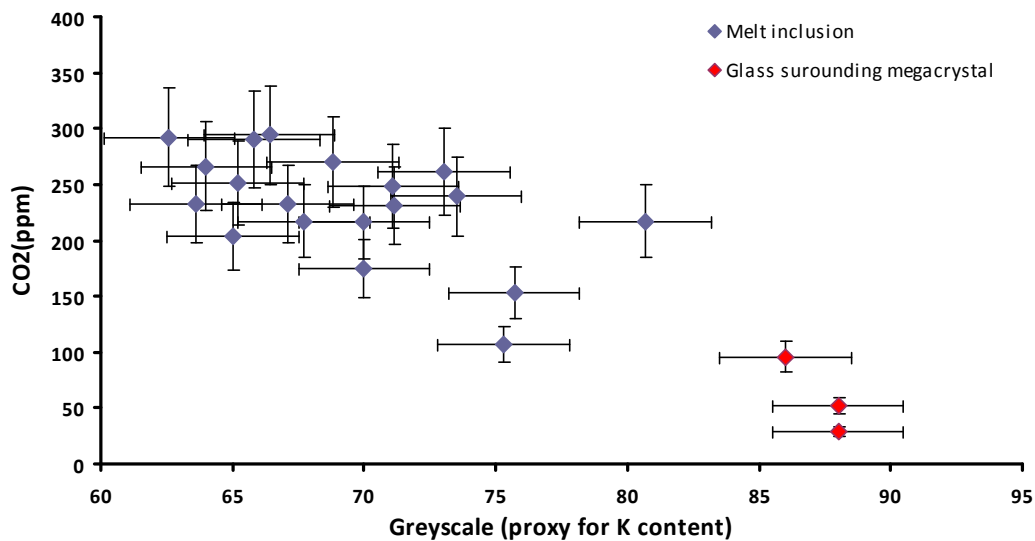


Figure 3: Scatter plot of the CO<sub>2</sub> content of 19 melt inclusions and 3 glasses determined by SIMS using the *ims1270* ion probe plotted against the average greyscale value of the pixel directly surrounding the inclusion in potassium x-ray map. The greyscale value of the pixels is a proxy for the potassium content of the zone in which each melt inclusion is enclosed. For the glasses the average composition of the closest pixels within the crystal were used.

The CO<sub>2</sub> content of each melt inclusion can be used to constrain its entrapment depth. Good models of the solubility of CO<sub>2</sub> in phonolitic melt however are still lacking. We therefore analysed 12 supra-liquidus phonolitic glass standards equilibrated at 2 and 3kbar (950°C; *f*O<sub>2</sub> near QFM) to get an idea of the entrapment depth of each inclusion (12 additional standards equilibrated at 1 and 0.5kbar are currently being analysed). The results are shown in Figure 4 and show that all melt inclusions analysed have been entrapped at pressure lower than 2kbar.

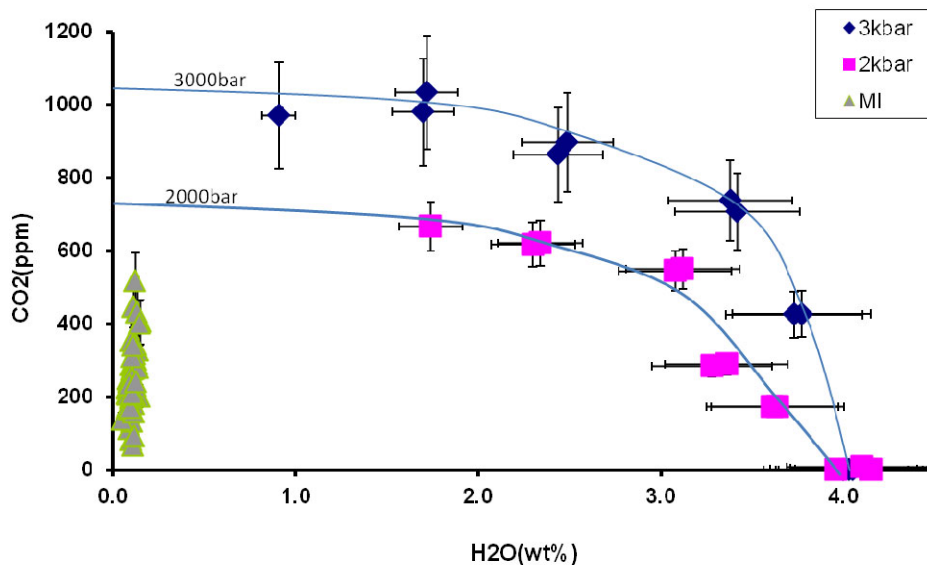


Figure 4: Scatter plot of the CO<sub>2</sub> and H<sub>2</sub>O content of 12 standard phonolite glass (each analysed twice) and 75 melt inclusions determined by SIMS using the *ims1270* and *ims4f* ion probe. Standard glasses define the 3000 and 2000 bar H<sub>2</sub>O-CO<sub>2</sub> fluid saturation isobars for Erebus phonolite.

## Conclusion

Analyses of the volatile content of anorthoclase megacrystal hosted melt inclusions showed a relationship between the entrapment depth of the melt inclusion and chemistry of their host zone. These findings corroborate previous experimental results in defining a relationship between the chemistry of a crystal zone and its growth pressure. This relation allows us to decode each crystal and track its history of circulation up and down the magmatic conduit and thereby test the hypothesis of a bi-directional exchange of material between the lava lake and a shallow magma body, which has become widely accepted in the literature (e.g., Kazahaya et al., 1994).

- Aster, R., et al., 2008. Moment tensor inversion of very long period seismic signals from Strombolian eruptions of Erebus Volcano. *J. Volcanol. Geotherm. Res.* 177, 635–647.
- Giggenbach, W.F., Kyle, P.R., Lyon, G., 1973. Present volcanic activity on Mt. Erebus, Ross Island, Antarctica. *Geology* 1, 135–136.
- Kazahaya, K., Shinohara, H., and Saito, G., 1994. Excessive degassing of Izu-Oshima volcano: magma convection in a conduit, *Bulletin of Volcanology*, 56, 207-216.
- Kelly, P.J., Kyle, P.R., et al., 2008. Geochemistry and mineralogy of the phonolite lava lake, Erebus volcano, Antarctica: 1972–2004 and comparison with older lavas. *J. Volcanol. Geotherm. Res.* 177, 589–605.
- Kyle, P.R., Moore, J.A., Thirlwall, M.F., 1992. Petrologic evolution of anorthoclase phonolite lavas at Mount Erebus, Ross Island, Antarctica, *J. Petrol.* 33, 849–875.
- Molina, I., Burgisser, A., Oppenheimer, C. 2012. Numerical simulations of convection in crystal-bearing magmas: A case study of the magmatic system at Erebus, Antarctica. *Journal of Geophysical Research*. doi:10.1029/2011JB008760
- Oppenheimer, C., Lomakina, A.S., Kyle, P.R., Kingsbury, N.G., and Boichu, M., 2009. Pulsatory magma supply to a phonolite lava lake: *Earth and Planetary Science Letters*, 284, 392-398.
- Oppenheimer, C., Moretti, R., Kyle, P., Eschenbacher, A., Lowenstern, J. & Hervig, R., 2011, Mantle to surface degassing of alkalic magmas at Erebus volcano, Antarctica, *Earth and Planetary Science Letters*, in press.
- Witham, F., 2011, Conduit convection, magma mixing, and melt inclusion trends at persistently degassing volcanoes. *Earth and Planetary Science Letters* 301, 345-352

# Constraining magma storage conditions at Uturuncu volcano, SW Bolivia

D. D. Muir<sup>1</sup>, J. D. Blundy<sup>1</sup> & A. C. Rust<sup>1</sup>

<sup>1</sup>School of Earth Sciences, University of Bristol, Wills Memorial Building, Queens Road, Bristol, BS2 8HE, UK

## Background

Uturuncu is an effusive composite volcano in the Bolivian Altiplano which has erupted dacites over a ~1 million year period. The last known eruption at Uturuncu was 270 ka<sup>[1]</sup> but recent uplift at the volcano detected with Interferometric Synthetic Aperture Radar suggests a renewal of activity. Magma intrusion in the mid- to upper crust is thought to be responsible for the ~80 km diameter deformation footprint calculated as 1-2 cm yr<sup>-1</sup> central uplift rate between 1992 and 2006<sup>[2]</sup>.

To better understand the sub-volcanic magma system we have investigated the petrology of natural dacite lavas and domes erupted at Uturuncu along with andesitic enclaves contained therein. We have analysed volatile compositions in melt inclusions in phenocrysts from natural samples from which minimum magma storage pressures can be calculated. In addition phase-equilibria experiments on synthetic dacite and natural andesite starting compositions from Uturuncu have been conducted to independently estimate magma storage conditions. By constraining the storage pressures of both dacite and andesite magmas we hope to be able to constrain the likely cause of deformation at Uturuncu.

## SIMS analyses

### 1) Melt inclusions

Concentrations of H<sub>2</sub>O and CO<sub>2</sub>, the most abundant volatiles in magma systems, within glass inclusions trapped in plagioclase phenocrysts from Uturuncu dacite lavas and domes have been analysed. The solubility of volatile species in silicic melts is strongly controlled by pressure. Assuming residual melts were volatile-saturated prior to eruption, minimum-trapping pressures can be calculated providing information on storage conditions where phenocrysts formed.

H<sub>2</sub>O contents of 3.2±0.7 wt% have been measured in 38 plagioclase-hosted melt inclusions and CO<sub>2</sub> is generally less than 160 ppm. Calculated minimum trapping pressures are between 50 and 119 MPa – much too shallow to be responsible for the deformation observed at Uturuncu. Melt inclusion trace element data have also been analysed and indicate the importance of isobaric crystallisation prior to eruption around ≤3 km below surface.

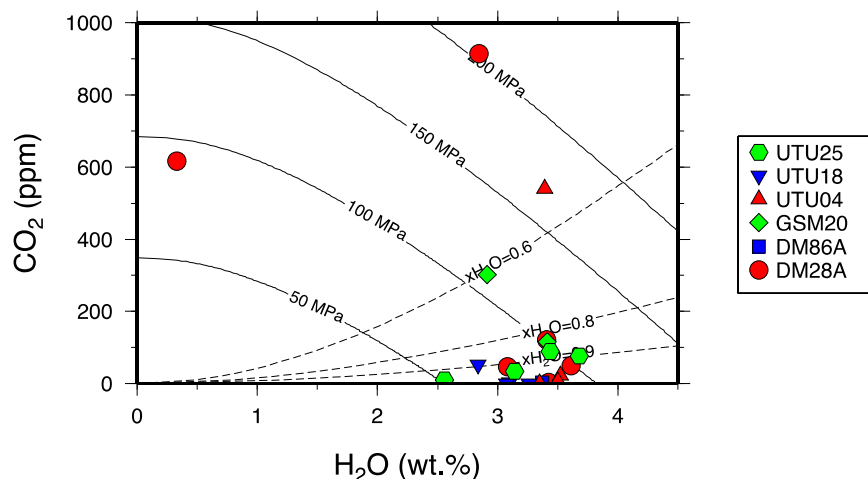


**Figure 1.** Measured H<sub>2</sub>O and CO<sub>2</sub> concentrations in plagioclase-hosted melt inclusions. Isobars (black solid lines) and volatile compositions (black dashed lines) were calculated using VolatileCalc<sup>[3]</sup>.

### 2) Dacite experiments

Melt inclusions are a useful tool for estimating pre-eruptive magma storage conditions but are prone to post-trapping modification by various processes. To constrain magma storage conditions more

robustly, phase-equilibria experiments using a typical Uturuncu dacite synthetic starting composition have been performed. Experiments were run H<sub>2</sub>O-saturated and glasses of run products have been analysed to determine the H<sub>2</sub>O solubility in typical high-K Uturuncu dacites at various pressures and temperatures. Measured H<sub>2</sub>O is between 3.1 and 6.4 wt.% and solubility increases with increasing pressure.

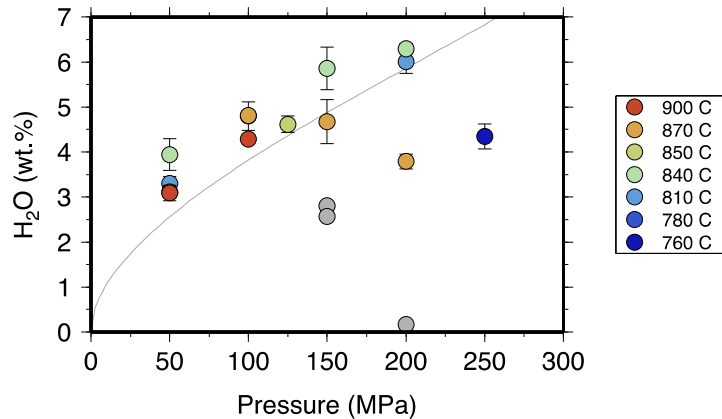


**Figure 2.** Dissolved H<sub>2</sub>O concentrations measured in residual rhyolitic melts from phase-equilibria experiments on typical Uturuncu dacite composition at various pressure-temperature conditions. Grey symbols are analyses thought to have been affected by mineral contamination. Calculated H<sub>2</sub>O solubility<sup>[3]</sup> for rhyolite melt at 870°C is shown by the grey line.

### 3) Andesite experiments

Phase equilibria experiments on natural andesite compositions from mafic enclaves in Uturuncu lavas are designed to constrain storage conditions of magmas that may be parental to dacites erupted at Uturuncu. Analysis and subsequent comparison of trace element concentrations in dacitic residual melt with those in whole-rock lava analyses enables us to test our model that dacites are formed by equilibrium crystallisation of andesites in mid-crustal storage regions. If deformation at Uturuncu does have a magmatic source it is more likely due to intrusion of andesitic magma at ~17 km below surface without concurrent inflation of shallow reservoirs where dacites are stored prior to eruption.

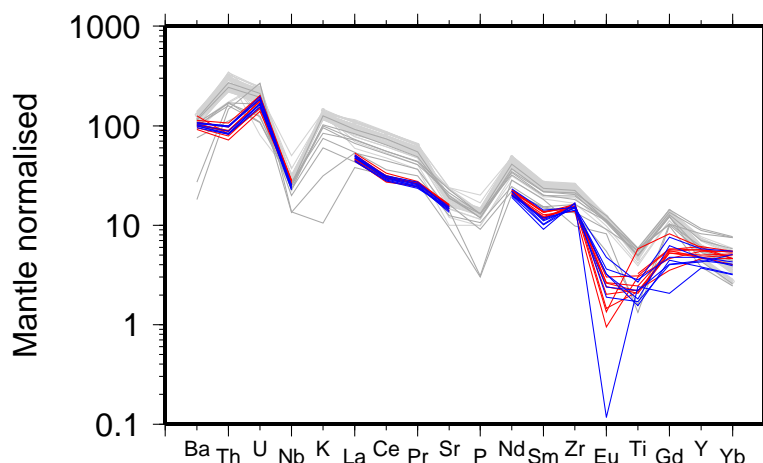


**Figure 3.** Volatile saturated (red) and undersaturated (blue) experimental glass trace element compositions from natural andesite starting composition normalised to primitive mantle. Natural whole-rock dacite (light grey) and andesite inclusion (dark grey) trace element compositions shown for comparison.

### References

- [1] Sparks et al. (2008) *American Journal of Science* **308**, 727-769
- [2] Pritchard and Simons (2002) *Nature* **418**, 167-171
- [3] Newman and Lowenstern (2002) *Computers and Geosciences* **28**, 597-604

# Skuggafjöll: A window into deep crystallisation, degassing and mixing in the Eastern Volcanic Zone of Iceland

D.A. Neave<sup>1</sup>, J. Maclennan<sup>1</sup>, M. Edmonds<sup>1</sup> & T. Thordarson<sup>2</sup>

<sup>1</sup>Department of Earth Sciences, University of Cambridge, Cambridge, CB2 3EQ, UK

<sup>2</sup>School of GeoSciences, University of Edinburgh, Edinburgh EH9 3JW, UK

## Objectives

Recent studies in the Eastern Volcanic Zone (EVZ) of Iceland have provided new insights into the nature of deep degassing and mixing processes in the plumbing systems of large basaltic fissure eruptions. For example, by using Nb as a proxy for undegassed CO<sub>2</sub> and assuming a CO<sub>2</sub>/Nb for primitive melts it is possible to estimate the total CO<sub>2</sub> budget for an eruption. However the environmentally impacting AD 1783 Laki eruption, which has been the focus of recent research is comparatively evolved in composition (Mg# = 42) and as a consequence the earliest phases of magmatic evolution may have been overprinted and lost. For example, olivine-hosted melt inclusions have low CO<sub>2</sub>/Nb ratios (<<300) which are consistent with the melt having degassed much of its CO<sub>2</sub> by the time of melt inclusions entrapment.

This project uses pillow basalt samples from the Skuggafjöll table mountain, which are amongst the most primitive basalts in the EVZ (Mg# = 54), in order to constrain early magmatic evolution and degassing processes better than at Laki. Specific project objectives are: (1) What was the primary CO<sub>2</sub> of the melt and the magmatic flux of CO<sub>2</sub> into the system? (2) What is the extent of CO<sub>2</sub> degassing prior to eruption and how does this relate to other magmatic processes such as crystallisation? (3) At what depth did these degassing and crystallisation processes take place?

## Approach

As of February 2013, one week of the two weeks of ion probe time awarded has been used. Out of a total of ~100 olivine-hosted melt inclusions to be analysed for major, trace and volatile elements, 60 have been measured so far. Olivines containing large, naturally quenched melt inclusions were picked from glassy pillow margins to minimise the effects of post-entrapment processes (**Figure 1**). Inclusions and glasses were analysed for CO<sub>2</sub>, H<sub>2</sub>O, F and selected trace elements (REEs, Nb and Zr) using a Cameca IMS-4f ion microprobe at the University of Edinburgh. Major elements, Cl and S were measured using a Cameca SX-100 electron microprobe at the University of Cambridge.

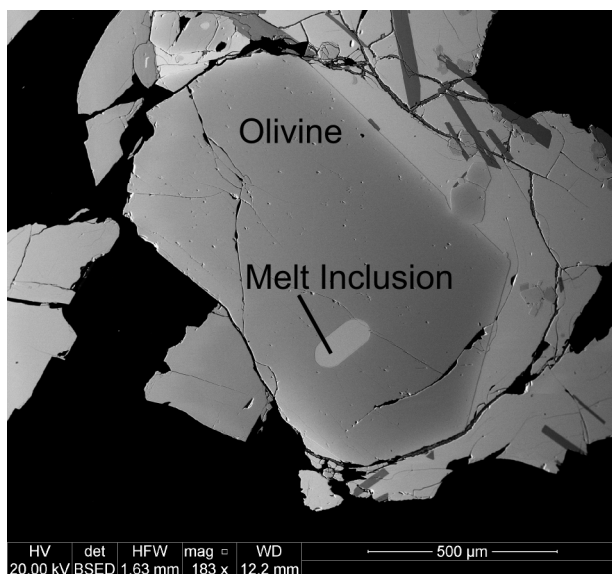


**Figure 1.** Backscattered scanning electron (BSE-SEM) image of an olivine macrocryst from Skuggafjöll showing a typical, glassy melt inclusion (>100 µm).

## Results

All of the olivine grains measured so far have very tightly constrained forsterite contents of Fo<sub>85-87</sub>, indicating that the large crystals selected during picking are primitive and suitable for investigating deep magmatic processes in primitive EVZ systems.

The major element compositions of melt inclusions indicate that post-entrapment crystallisation has been minimal (<5%). Trace element variability in melt inclusions is greater than analytical error for elements which can be determined with high precision such as Zr & Ce (**Figure 2**). Matrix glasses are significantly more enriched in trace elements than the melt inclusions and do not show variability greater than analytical error. Strong correlations are observed between incompatible trace element concentrations (e.g. Zr, Nb, La, Ce) and between trace element ratios (e.g. La/Yb).

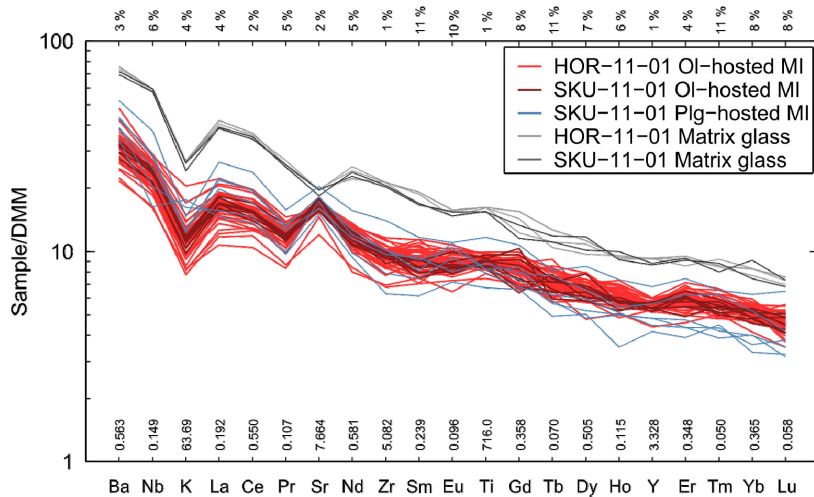


**Figure 2** Depleted MORB Mantle (DMM) normalised trace element spider diagram of Skuggafjöll melt inclusions and matrix glasses.  $1\sigma$  % relative errors are shown along the top and normalisation values along the bottom.

Both melt inclusions and matrix glasses contain  $\sim 0.38$  wt.%  $H_2O$  (**Figure 3**). This is consistent with rapid diffusive re-equilibration of  $H_2O$  during the course the eruption under ice during the last glacial period ( $>10$  ka). In contrast, the  $CO_2$  concentration of melt inclusions is highly variable and ranges from 200 to up to 1200 ppm (**Figure 3**).  $CO_2/Nb$  values reach up to 410, consistent with the the only other coincident study of volatiles and trace elements in Iceland (**Figure 4**)<sup>1</sup>.

$CO_2$  concentrations correlate negatively with trace element (**Figure 4**), in complete contrast with positive correlations in from previous ‘un-degassed’ datasets<sup>2</sup>. At face value this anti-correlation could be interpreted as a record of concurrent crystallisation and degassing. However negative correlations are also observed between  $CO_2$  and trace element ratios such as  $La/Yb$  (**Figure 4**). The most depleted, low  $La/Yb$  inclusions have the highest  $CO_2$  and the most enriched, high  $La/Yb$  inclusions the lowest. This is the first time that such an observation has been made and suggests that  $CO_2$  behaved differently in parental melts of different compositions during the formation of the Skuggafjöll magma. These observations may possibly be accounted for by mixing of variably degassed melts shortly prior to eruption.

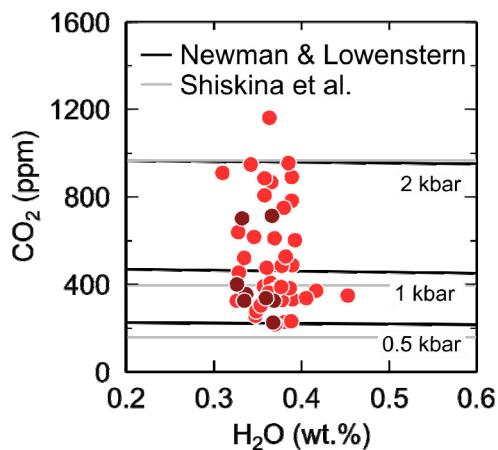


**Figure 3**  $H_2O$  and  $CO_2$  contents of Skuggafjöll melt inclusions. Isobars from two parameterisations of  $H_2O$ - $CO_2$  equilibrium are shown.

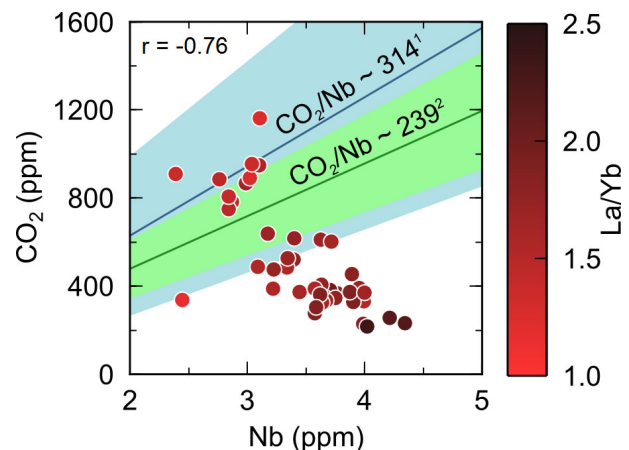


**Figure 4** Strong negative correlation of  $CO_2$  with Nb (expressed as  $r$ ). High  $CO_2$  and  $CO_2/Nb$  inclusions are associated with depleted, low  $La/Yb$ .  $CO_2/Nb$  from Iceland<sup>1</sup> and Siquieros<sup>2</sup> shown for comparison.

### Future directions

A further  $\sim 60$  inclusions will be measured later April 2013, including  $\sim 30$  from a smaller size fraction of olivines to extend the range host forsterite content to lower values. An abstract has been submitted to present this work IAVCEI 2013 in Kagoshima, Japan. This research will also be the subject of a publication to be submitted towards the end of 2013.

### References

- [1] Hauri E et al. (2002) *AGU, Spring Meeting* **V51D-03**
- [2] Saal A. E et al. (2002) *Nature* **419**, 451-455

# Constraining shear heating in mylonites using the Ti in quartz geothermometer

G. Pennacchioni<sup>1</sup>, G. D. Bromiley<sup>2</sup> & F. Nestola<sup>3</sup>

<sup>1</sup>Dipartimento di Geoscienze, University of Padova, Italy

<sup>2</sup>School of GeoSciences, University of Edinburgh, Edinburgh EH9 3JW, UK

## Background: shear heating of mylonites

The study of the Ti in quartz within sheared quartz veins from the Lake Edison granodioritic pluton (Sierra Nevada batholith, California) follows a previous study (conducted at the IMF) on sheared quartz veins from the tonalitic Adamello pluton (northern Italy) (Pennacchioni et al., 2010). In both plutons, quartz veins filled joints that had developed during the early stages of pluton cooling, and were deformed at relatively high temperature ( $> 450^{\circ}\text{C}$ ) during the cooling of the pluton at the base of the seismogenic crust. The Ti in quartz geothermometer is potentially a precise thermometer calibrated experimentally for conditions suitable for magmatic systems. However, it has also been suggested that Ti can equilibrate in quartz at the lower temperature conditions of mylonitic deformation and therefore can be a powerful tool to establish the ambient conditions of deformation. Recent experimental work by our group (PhD student Matt Hiscock) also conducted with the IMF demonstrates that grain boundary diffusion of Ti provides the most likely mechanism for fully re-equilibrating Ti in quartz at these lower temperatures. The aim of the current project is two-fold: 1) compare the ambient conditions of ductile deformation in the Sierra in the Adamello pluton (Pennacchioni et al., 2010) to develop a general model of structural evolution during pluton cooling; 2) establish which of the available calibrations on Ti in quartz (and the influence of pressure) is the most suitable to be used.

## Preliminary results

The results of the SIMS investigation conducted in Edinburgh in December 2012 on 14 different mylonitic quartz veins sampled along a transect of the LE pluton show Ti contents mostly in a range of 5-10 ppm. These contents are similar to the ones measured for the quartz mylonites of the Adamello and, therefore, suggest similar conditions of mylonitization in the two plutons. The precise estimate of the temperature of deformation depends on the specific Ti in quartz calibration, on the “assumed” Ti activity and pressure. For both the Adamello and the Sierra the lithostatic pressure during deformation is known<sup>2</sup> and the use of the more recent P-dependent calibrations<sup>3,4</sup> implies the assumption of a correct value for the  $a_{\text{TiO}_2}$ . We can constrain the Ti activity if an independent estimate of the temperature is possible for the mylonites. Detailed textural analysis of both the Adamello and Sierra quartz mylonites show a crystallographic preferred orientation (CPO) characterized by a strong Y-max of the c-axis. This texture only develops in quartz mylonites at  $T \geq 500^{\circ}\text{C}$ . Furthermore, granitoid mylonites associated with these quartz mylonites have a stable mineral assemblage consisting of recrystallized biotite, oligoclase and K-feldspar which also point to high temperatures ( $T > 450^{\circ}$ ). On-going work will establish the exact temperature of deformation, but the preliminary data indicate relatively high Ti activity in quartz mylonites and deformation conditions above  $450^{\circ}\text{C}$ .

## References

- [1] G. Pennacchioni et al. (2010) *Journal of Geophysical Research –Solid Earth* **115**, B12405
- [2] G. Pennacchioni (2005) *Journal of Structural Geology* **27**, 627-644
- [3] J.B. Thomas et al. (2010) *Contributions to Mineralogy and Petrology* **160**, 743-759
- [4] R. Huang and A. Audetat (2012) *Geochimica et Cosmochimica Acta* **84**, 75-89

PAGE INTENTIONALLY LEFT BLANK

# Timing and sources of voluminous low- $\delta^{18}\text{O}$ rhyolite magmas in the Snake River (Columbia River-Yellowstone LIP), USA: a combined oxygen isotope and U/Pb dating study on zircon

M.K. Reichow, T.R. Knott & M.J. Branney

Geology Dept., University of Leicester LE1 7RH, UK

## Introduction

A striking feature of large-volume rhyolite volcanism in the Snake River Plain (SRP), USA, is a very low- $\delta^{18}\text{O}$  (-1.8 to 3.9‰) signature [1,2]. The origin of this feature is controversial and may bear upon how copious rhyolite is generated at similar silicic LIPs elsewhere [4]. The rhyolites are A-type (high Ga/Al) and have been considered variously to be predominantly mantle or crustal derived [3,4,5]. The SRP has received scant attention in comparison to its better-known neighbours (Columbia River and Yellowstone) and fundamental questions remain about what controlled the unusual chemistry and eruptive behaviour [6]. The low- $\delta^{18}\text{O}$  signature may reflect: (1) wholesale melting of mid-crustal Cretaceous-Tertiary hydrothermally-altered granitoids [2]; (2) melting of hydrothermally altered intracaldera tuffs, down-dropped to 12 km [1]; or (3) large fluxes of meteoric water from the Miocene Lake Idaho involving subvolcanic depressurisation and ingestion during caldera-collapse [7].

**Objectives:** Volcanic rocks with low- $\delta^{18}\text{O}$  were once thought to be rare [8] but more frequent and voluminous occurrences are being reported. In the SRP their generation involved a major re-configuration of the continental crust. By combined oxygen isotope and U/Pb dating on zircons we are starting to reconstruct the evolution of intracrustal recycling and crust-mantle interaction through time, towards a model for the formation of voluminous low- $\delta^{18}\text{O}$  continental intraplate rhyolites. Single-crystal analysis is essential as multi-grain analyses would average any inter- or intracrystalline oxygen isotope and age differences. Considering  $\delta^{18}\text{O}$  and U/Pb data from the same zone within an individual zircon crystal permits the distinction of magmatic events (juvenile crustal growth) from reworking of pre-existing hydrothermally altered crust, or some combination of these [9]. Zircon is a common accessory mineral in these SRP rhyolites. Due to their resilience to alteration and melting, they provide better estimates of the oxygen isotope signature of the protoliths and the magmas than from currently available data.

**Results:** The majority of recovered zircons are euhedral tetragonal dipyrramids, 30 to 200  $\mu\text{m}$  long. CL imaging revealed that the majority are zoned and some contain inclusions of zircon and/or apatite.

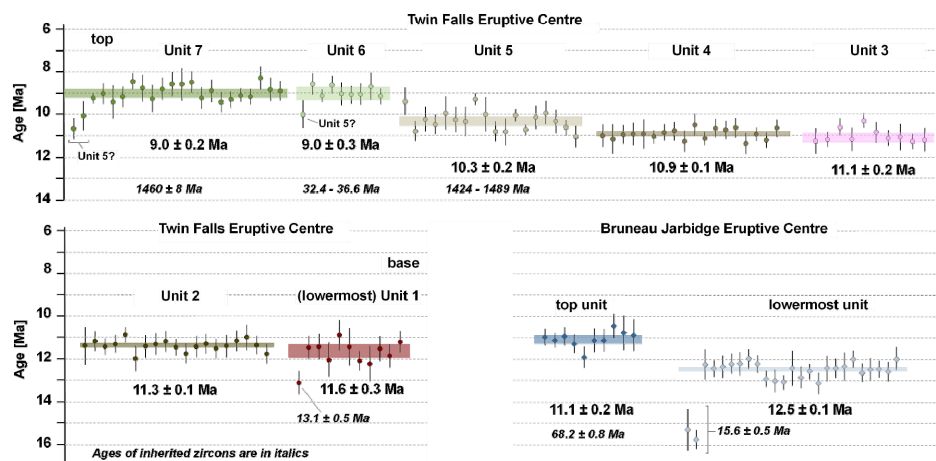
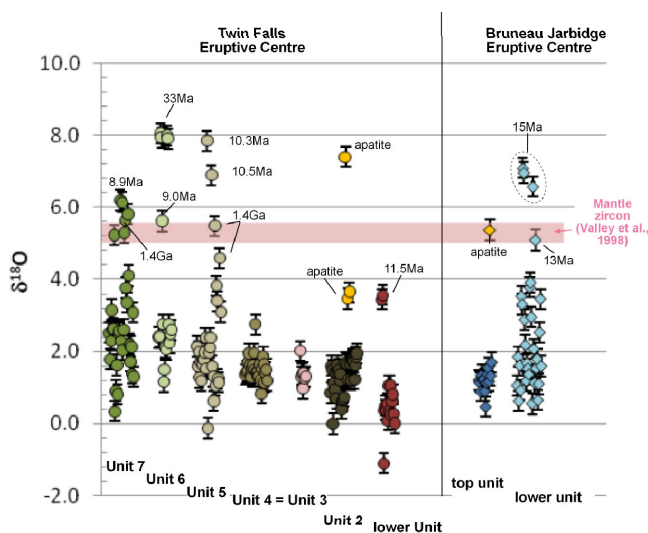


**Figure 1.**  $^{206}\text{Pb}/^{238}\text{U}$  crystallisation ages for zircon analyses. All uncertainties are  $2\sigma$  except for pre-Miocene ages. Unit weighted mean ages are indicated as coloured bars with the height of each bar representing the uncertainty.

**U/Pb age determinations:** We analysed 10 to 24 zircons from 9 ignimbrites from the Mid-Miocene Bruneau Jarbidge (2 samples) and Twin Falls (7 samples) centres, to document the initiation and end of explosive volcanism at each centre, which hitherto was not known. Where possible, U/Pb analyses were taken from cores and rims of individual zircons. The U/Pb zircon ages gave a spread from 1.4 Ga to 9.0 Ma. Older zircons, and a larger spread of ages are mostly in the younger units, of which four contain zircons with pre-Miocene ages falling into three groups: ages of ~1.4 Ga; 68 Ma; and 33 Ma (Fig. 1). Th/U ratios in these older zircons (from 1.3 to 2.5) differ from those in younger zircons (0.4 to 0.9). Only the 33 myr old zircons in Twin Falls Unit 6 represent old cores with a younger

overgrowth the same age as the unit: in this case, the oxygen isotope signature of the zircon core also differs from its overgrowth (see below). The older, pre-Miocene zircons probably represent protolith ages. This is supported by published whole rock-radiogenic isotope data, suggesting a strong influence of old crustal lithologies in the formation of the rocks [5]. Some zircons yield ages consistent with derivation from subjacent Mid-Miocene rhyolites (with similar Th/U ratios) from the same eruptive centres, presumably entrained in the magma chamber or during emplacement. The weighted mean zircon  $^{206}\text{Pb}/^{238}\text{U}$  ages range from 12.5 Ma to 11.1 Ma (Bruneau Jarbidge; duration 1.4 myrs) and 11.6 to 9.0 Ma (Twin Falls; duration 2.6 myrs ; Fig. 2). The two centres overlapped briefly. This is in contrast to interpretations based on  $^{40}\text{Ar}/^{39}\text{Ar}$  age data [11].

**Oxygen isotope data:** Over 200 oxygen isotope analyses were conducted. External errors of 5+ standard analyses within each block of data were typically better than 0.17‰ (1 SD). The data range from mantle-like to elevated (~8)  $\delta^{18}\text{O}$  ratios, but 91% lie below mantle-like ratios (<5.6; Fig. 3). Despite the variation in  $\delta^{18}\text{O}$  ratios within an individual eruption, a general increase in  $\delta^{18}\text{O}$  over time is observed. This is in contrast to reported [1] oxygen data from the 2 Ma Yellowstone volcanic field where initial volcanism has mantle  $\delta^{18}\text{O}$  ratios and these decrease with time. Mantle or higher ratios are observed in all pre-Miocene zircons.  $\delta^{18}\text{O}$  ratios were generally low, with cores higher than the rims, with some exceptions (e.g. Twin Falls Unit 5). Some same-age zircons within a single unit displayed different  $\delta^{18}\text{O}$  ratios, so a clear correlation between the age of zircon and  $\delta^{18}\text{O}$  ratios is not apparent. Two zircons (Twin Falls unit 7) had a mantle-like  $\delta^{18}\text{O}$  of the inherited cores and low  $\delta^{18}\text{O}$  ratios from the overgrown rim, but indistinguishable U/Pb ages. Despite the overall trend of increasing  $\delta^{18}\text{O}$  ratios, the single-crystal data are more complex than studies using multi-grain or whole-rock oxygen data have revealed [1,2].



Displayed different  $\delta^{18}\text{O}$  ratios, so a clear correlation between the age of zircon and  $\delta^{18}\text{O}$  ratios is not apparent. Two zircons (Twin Falls unit 7) had a mantle-like  $\delta^{18}\text{O}$  of the inherited cores and low  $\delta^{18}\text{O}$  ratios from the overgrown rim, but indistinguishable U/Pb ages. Despite the overall trend of increasing  $\delta^{18}\text{O}$  ratios, the single-crystal data are more complex than studies using multi-grain or whole-rock oxygen data have revealed [1,2].

**Figure 2.** Oxygen isotope zircon values for volcanic rocks of the Bruneau Jarbidge and Twin Falls eruptive centres, SRP. Note progressive increase in  $\delta^{18}\text{O}$  towards younger eruption units. Apatite occurs as inclusion within zircon (Mantle zircon value after [10]).

**Summary** Volcanic activity at Bruneau Jarbidge lasted 1.4 myrs, and at Twin Falls 2.6 myrs. Zircon ages provide evidence for inheritance from Proterozoic, Cretaceous and Oligocene crust. Zircon oxygen data are very low, and increased with time, whereas the inherited zircons all have mantle-like values. These data are in stark contrast to the proposed model 2 by [1]. The range of inherited zircon ages also makes wholesale melting of Cretaceous-Tertiary hydrothermally-altered granitoids (model 1) as the sole source for the low oxygen signature questionable. Based on our data we advocate that a more complex scenario is required in which more than one mechanism operated. This warrants further studies preferentially on individual zircon by the ion-microprobe analyses.

## References

- [1] Bindeman et al. (2007) *Geology* **35**, 10191–1022
- [2] Boroughs et al. (2005) *Geology* **33**, 821–824
- [3] Eby (1990) *Lithos* **26**, 115–134
- [4] Whalen et al. (1987) *Contributions to Mineralogy and Petrology* **95**, 407–419
- [5] Nash et al. (2006) *Earth and Planetary Science Letters* **247**, 143–156
- [6] Andrews and Branney (2011) *Bulletin of the Geological Society of America* **123**, 725–743
- [7] Branney et al. (2008) *Bulletin of Volcanology* **70**, 293–314
- [8] Taylor (1986) *Review in Mineralogy* **16**, 273–316
- [9] Kemp et al. (2006) *Science* **315**, 980–983
- [10] Valley et al. (1998) *Contributions to Mineralogy and Petrology* **132**, 371–389
- [11] Bonnicksen et al. (2008) *Bulletin of Volcanology* **70**, 315–342

# Interpreting degassing paths in crystallising magmas: constraints from experiments on Mount St. Helens rhyodacite

J. Riker<sup>1</sup>, J. Blundy<sup>1</sup> & A. Rust<sup>1</sup>

<sup>1</sup>School of Earth Sciences, University of Bristol, Bristol BS8 1RJ, UK

## Motivation

Degassing and concomitant crystallization play an important role in volcanic systems due to their influence on the physical properties of magmas. However, the ephemeral nature of volatile components like H<sub>2</sub>O and CO<sub>2</sub> means the behaviour of volcanic gases during magma storage and ascent is notoriously difficult to interpret. Moreover, magmas may experience a variety of degassing scenarios during their transport through the crust, not limited to simple ascent-driven decompression, each leading to crystallization in different ways [1]. To this end, we have undertaken an experimental study to show how the petrologic record preserved in co-existing melts and crystals can provide constraints on the composition, quantity, and transport of vapour in magmatic systems.

## Approach

We have run a series of high-temperature, high-pressure experiments designed to investigate the effect of degassing path on equilibrium crystallization of a synthetic Mount St. Helens rhyodacite (Sugar Bowl composition). Run pressures simulate magma storage depths ranging from the near-surface to the mid-crust (25 to 450 MPa), and all samples were saturated with binary H<sub>2</sub>O-CO<sub>2</sub> fluids across a range of compositions – water-rich to water-poor. This set of experiments allows us to examine how phase stability, phase abundance (crystallinity), and phase compositions vary as a function of two key variables: pressure and fluid composition. Pressure is known from the experimental setup, but fluid composition must be calculated from measured melt volatile contents. Due to the crystal- and bubble-rich nature of our experimental run products, SIMS is the only suitable technique for H<sub>2</sub>O and CO<sub>2</sub> determinations.

Over the past year, we have analysed 42 experimental glasses for H<sub>2</sub>O and CO<sub>2</sub> at the NERC Ion Microprobe Facility. The majority of samples were run in March and April on the Cameca 4f as <sup>1</sup>H/<sup>30</sup>Si and <sup>12</sup>C/<sup>30</sup>Si. A subset of water-rich samples run as (OH)<sup>30</sup>Si on the Cameca 1270 yielded

H<sub>2</sub>O contents in conflict with independent measurements by KFT; these are currently being reanalysed on the 4f using an extended range of rhyolite glass standards. Preliminary comparison of 4f and 1270 data suggest that the <sup>1</sup>H/<sup>30</sup>Si calibration curve, as measured on the 4f, is linear in rhyolitic glasses to water contents of up to 11 wt%, while the (OH)<sup>30</sup>Si calibration curve is strongly non-linear at water contents >4-5 wt%. Based on these observations, we would caution against the use of (OH)<sup>30</sup>Si for analysis of hydrous glasses barring further development of the method.

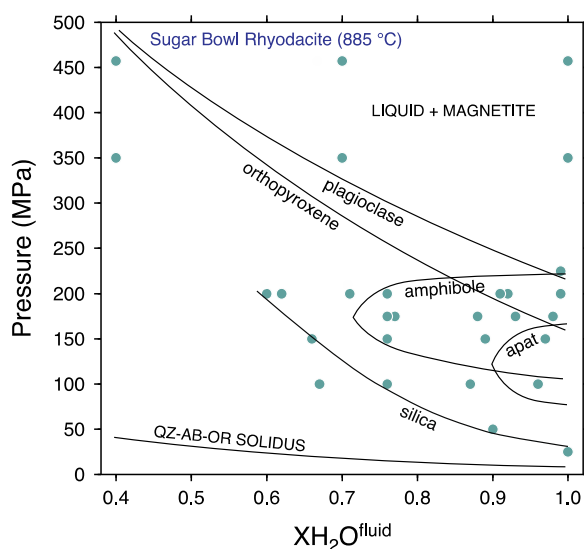


**Figure 1.** Phase diagram for the Sugar Bowl rhyodacite at 885 °C. Fluid composition is expressed as the mol fraction of water in a two-component fluid ( $X_{H_2O}^f$ ).  $X_{H_2O}^f$  is calculated from the H<sub>2</sub>O and CO<sub>2</sub> contents of experimental glasses, measured by SIMS, using a compositionally-dependent fluid partitioning model [2].

## Results

We have used data acquired at the IMF for two main purposes. In the first instance, measured glass H<sub>2</sub>O and CO<sub>2</sub> contents were used to calculate the equilibrium fluid composition in each run. Combining this information with run pressures and the observed phase assemblages, we have constructed a phase diagram for the Sugar Bowl rhyodacite in pressure–fluid composition space (Fig. 1). This phase diagram

emphasizes the strong dependence of mineral stability on melt water content at isothermal conditions. As a second application of SIMS data, H<sub>2</sub>O measurements have been used to parameterize key attributes of the crystallizing system, namely phase proportions and the anorthite content of plagioclase, as functions of the H<sub>2</sub>O content of the co-existing melt.

Together these data enable us to develop a simple, isothermal model with which we can specify equilibrium crystallinity and plagioclase composition, melt H<sub>2</sub>O and CO<sub>2</sub> content, the stable phase assemblage, and the proportions of major phases at any point within our experimental parameter space (Fig. 2). By projecting degassing paths onto our phase diagram, we are able to model the evolution of our experimental system along four endmember degassing ‘trajectories’: water-saturated degassing, closed-system degassing, isobaric vapour fluxing, and vapour-buffered ascent. While melt water content preserves no unique record of the degassing history of a melt (due to its controlling influence on crystallization and crystal-melt equilibria), our model shows how melt CO<sub>2</sub> content, when plotted against some index of crystallinity (for example melt K<sub>2</sub>O content, or an incompatible trace element), can be a sensitive indicator of degassing path – even in the absence of reliable water data. At present,

we are working to extend our interpretation to suites of CO<sub>2</sub> and trace element data from natural Mount St. Helens glasses, to provide insight into the mechanisms of gas generation and transport at the volcano.

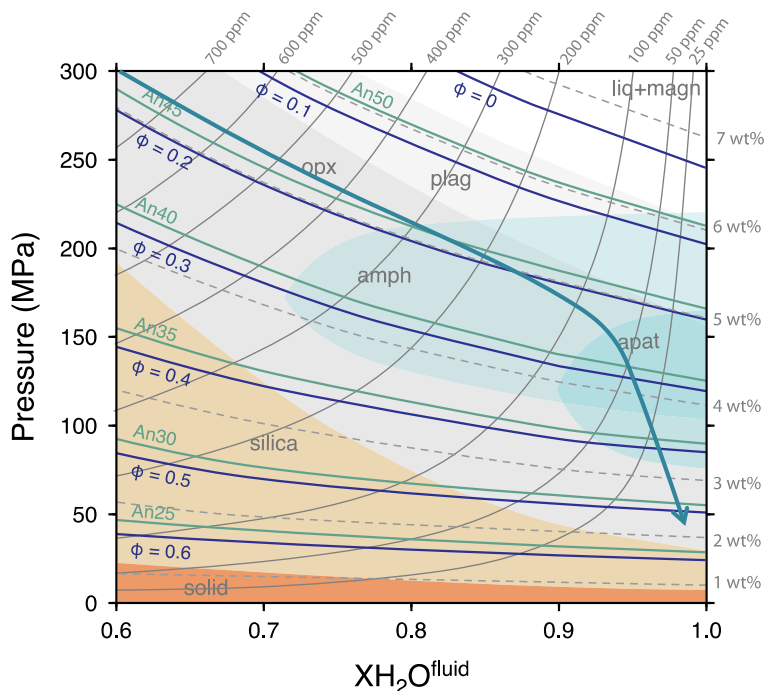


**Figure 2.** Isothermal degassing model for the Sugar Bowl rhyodacite. Contours give equilibrium crystallinity as mass fraction (dark blue lines), plagioclase anorthite content as mol% (green lines), modeled H<sub>2</sub>O and CO<sub>2</sub> solubilities (in wt% and ppm, respectively) [2], and mineral stability fields for plagioclase (plag), titanomagnetite (magn), orthopyroxene (opx), amphibole (amph), apatite (apat), and silica. Blue arrow is a projected closed-system degassing path.

### Presentations and Publications

The data obtained during our 2013 visits has been presented at two scientific conferences [3,4]. A manuscript incorporating these data is also in preparation for submission to Contributions to Mineralogy and Petrology.

### References

- [1] Blundy et al. (2010) Earth and Planetary Science Letters **290**, 289-301
- [2] Papale et al. (2006) Chemical Geology **229**, 78-95
- [3] Riker et al. (2012) American Geophysical Union Fall Meeting, San Francisco, U.S.A.
- [4] Riker et al. (2013) Volcanic and Magmatic Studies Group Annual Meeting, Bristol, U.K.

# Melting of natural MORB at subduction zone conditions

J. Blundy<sup>1</sup>, S. Skora<sup>1</sup> & L. Carter<sup>1,2</sup>

<sup>1</sup>School of Earth Sciences, University of Bristol, Bristol BS8 1RJ, UK

<sup>2</sup>Department of Earth Sciences, Rice University, Houston, Texas 77005, USA

**Introduction:** In subduction zones, the descending oceanic plate is gradually heated, releasing fluids via dehydration reaction or partial melting of the oceanic plate itself. These trace element enriched fluids and/or melts trigger melting in the overlying mantle wedge by lowering its melting point, imparting a characteristic geochemical signature onto arc magmas. Arc geochemists have proposed that at least two different fluid components play a role in generating the arc signature: 1) a sediment melt component with low Ba/Th and high La/Sm<sub>PUM N</sub> values (mimicking its source) and 2) a fluid component derived from the altered oceanic crust (AOC) with high Ba/Th and low La/Sm<sub>PUM N</sub> values. Ba/Th enrichment over the source value is thereby explained by the highly fluid mobile behaviour of Ba over Th in fluids (as opposed to hydrous melts where Th can be quite mobile).

Although mid-ocean ridge basalt (MORB), AOC and sediment melting were the focus of many experimental studies in the past, surprisingly, almost none of the studies were conducted with trace element concentrations thought to be realistic for any of these units. We have found in past studies (on sediment melting) that doping can lead to quite unexpected results and data so obtained may not be applicable to nature [1,2]. In addition, Ba, Th, La and Sm concentrations should be sensitive to the phase assemblage and therefore not necessarily mimic source values. This is due to the fact that these elements are controlled and potentially fractionated by minerals and accessory phases that are supposed to be stable at sub-arc depth (e.g. La and Th is fractionated from Sm by garnet ( $D_{La,Th} \ll D_{Sm}$ ) in sediment and basalt, monazite ( $D_{La} \approx D_{Sm} \ll D_{Th}$ ) in sediment, and allanite ( $D_{La} \gg D_{Sm} \gg D_{Th}$ ) in basalt. We also found that Ba/Th enrichment is not replicated in AOC sub-solids experimental studies, because Ba is very compatible in phengite. Combined, this has prompted us to re-investigate the trace element signal of partial melts of basalts, using natural, undoped compositions.

**Experiments and results:** Two representative basaltic lithologies were picked: a pristine MORB sample from the Kolbeinsey ridge (N of Iceland) and an AOC sample from the DSDP leg 46 (Mid Atlantic, ~20°N). Experiments were conducted at 3 GPa over a range of temperatures (800-1000°C), with 12-15 wt% of water added on top of structurally-bound water (total water content  $\approx$  15 wt%). The high H<sub>2</sub>O content is designed to simulate fluxing by serpentine-derived fluids in the slab. In agreement with previous studies, we find that the solidus temperature is much lower for altered oceanic crust ( $T_{solidus} < 800^\circ\text{C}$  at 3 GPa) that is enriched in K (approx. 0.3 wt%) when compared to K-poor, pristine MORB (approx. 0.03 wt%;  $800 < T_{solidus} < 850^\circ\text{C}$ ). Silicate phases co-existing with hydrous glasses include: garnet, clinopyroxene and minor amounts of kyanite (AOC), Fe-Ti oxide, rutile, as well as epidote in all runs conducted at  $T < 1000^\circ\text{C}$ . Trace amounts of quartz are only present at sub-solidus conditions (pristine, K-poor MORB only). Such a phase assemblage is largely in agreement with previous studies, as well as with natural examples of exhumed UHP rocks. New is the presence of epidote over allanite, which we attribute to the undoped nature of our starting material.

**Discussion:**  $D_{glass-bulk\ solids}$  partition coefficients were calculated from the mass balance equation (Fig. 1a, b). Our pristine MORB data is further compared to Kessel et al. ([3]: K-free MORB), and altered MORB data is compared to Klimm et al. ([4]: K-bearing MORB). Both these studies used variably doped starting materials. It is apparent from Fig. 1 that elements that are incompatible (e.g. Cs, Ba, Rb, Sr) and elements that are partitioning-controlled (e.g. HREE: garnets) compare well to the other studies. Elements that are controlled by accessory phases (e.g. LREE&Th: allanite/monazite/epidote) compare less well, because bulk partition coefficients are sensitive to doping levels. This is because high doping levels leads to an increase in  $X_{accessory\ phase}$  in the bulk solids, keeping the (accessory phase) buffered element in the melt constant. Most importantly, we have found that LREE&Th is not controlled by allanite as was suggested by doped experiments. Although this appears to be a detail at first (because of epidote-allanite solid solution), it must be noted that the behaviour of LREE+Th is distinctly different. If allanite is present, LREE are solubility controlled; if epidote is present, LREE are partitioning-controlled, seriously restricting its concentrations in slab fluids (Fig. 1c). For example,

$\Sigma$ LREE of undoped MORB/AOC derived melts are around 0.5-5 ppm (800-900°C), which is significantly less when compared to doped, allanite-bearing experiments (50-170 ppm [4]). (Thorium concentrations are also seriously different in both cases: 0.01-0.1 ppm in our experiments as opposed to 26-122 ppm in allanite-bearing experiments ([4])).

Hence it can be concluded that LREE+Th enrichments in arc lavas are solely due to LREE+Th transfer from the sedimentary portion. MORB and AOC only really contribute some of the highly incompatible elements such as Cs, Ba, Rb and Sr, as well as a little bit of Zr and Hf. Our finding that epidotes exist over allanites in subducted basalts has serious consequences for the H<sub>2</sub>O/Ce slab top thermometer of Plank et al. [5] that requires allanite-buffered Ce concentrations, and shows once more that application of doped experiments to nature can lead to an erroneous picture.

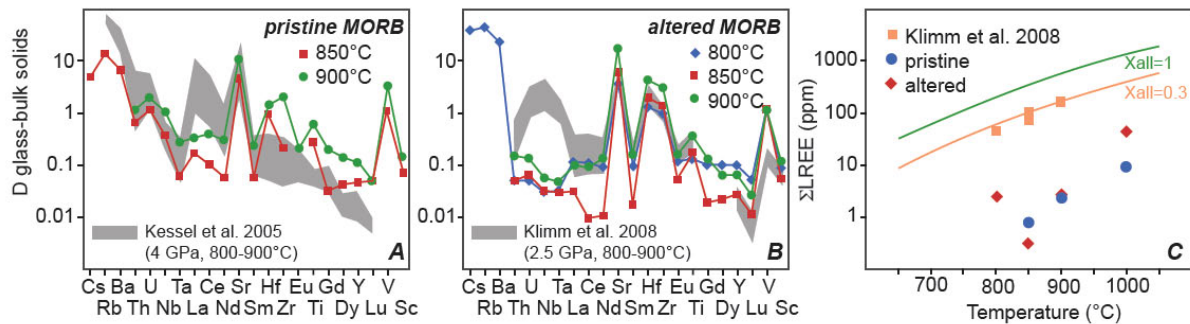


Fig. 1: Calculated  $D_{\text{glass-bulk solids}}$  partition coefficients A: pristine MORB (compared to K-free MORB); B: altered MORB (compared to K-bearing MORB); C: LREE calculated using the allanite solubility model of Klimm et al. (2005), compared to our data (= epidote bearing MORB).

Our new trace element data also shows that in order to replicate high Ba/Th ratios measured in arc lavas, the basaltic crust must melt so that phengite, the main host for Ba, disappears via the melting reaction: phengite + clinopyroxene + quartz + H<sub>2</sub>O = garnet + hydrous melt ( $T_{\text{solidus}} @ 3 \text{ GPa} \sim 750^\circ\text{C}$ ). Thorium concentrations are seriously restricted by the presence of epidote, further, contributing to high Ba/Th in partial melts. Once epidote is melted-out in between 900-1000°C, Ba/Th ratios approach bulk values because all Ba&Th is now contained in the melt. Thus the ‘fluid’ phase transpires to be a hydrous melt, placing constraints on minimum slab top temperatures (= wet solidus).

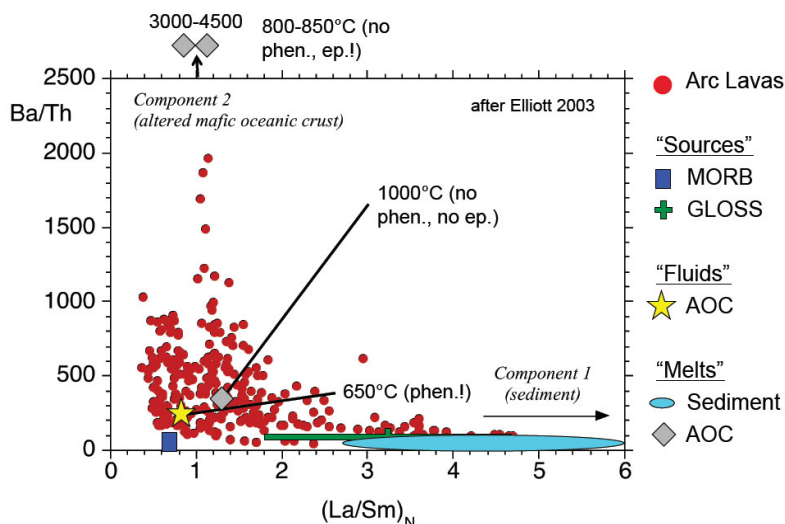


Fig. 2: Ba/Th and  $(\text{La}/\text{Sm})_{\text{PUM N}}$  values of primitive arc lavas, sources (MORB + sediment (given as GLOSS here: global subducting sediment)) as well as fluids and partial melts in equilibrium with these slab lithologies. Sediment melt data come from our undoped experiments (manuscript in preparation); AOC fluid data is from Green and Adam [6]; AOC melt data is from this study. Only a selection of data is given for clarity. This diagram shows that in order to achieve high Ba/Th ratios, phengite, the main host for Ba, must melt-out. Epidote is also required in order to keep Th concentrations low.

## References

- [1] S. Skora & J.D. Blundy, *J. Petrol.* **51** (2010), 2211-2243.
- [2] S. Skora & J.D. Blundy, *EPSL* **321-322** (2012), 104-114.
- [3] R. Kessel, M.W. Schmidt, P. Ulmer & T. Pettke, *Science* **437** (2005), 724-727.
- [4] K. Klimm, J.D. Blundy & T.H. Green, *J. Petrol.* **49** (2008), 523-553.
- [5] T. Plank, L.B. Cooper & C.E. Manning, *Nature Geosci.* **2** (2009) 611- 614.
- [6] T.H. Green & J. Adam, *Eur. J. Mineral.* **15** (2003), 815-830.

# Magma storage and differentiation beneath Grenada (Lesser Antilles)

C.C.Stamper<sup>1</sup>, J.D.Blundy<sup>1</sup>, E.Melekhova<sup>1</sup> & R.J.Arculus<sup>2</sup>

<sup>1</sup>Department of Earth Sciences, University of Bristol, Bristol, BS8 1RJ, UK

<sup>2</sup>Research School of Earth Sciences, The Australian National University, Canberra 0200, Australia

## Background

The igneous cumulate suite of the volcanic island of Grenada, Lesser Antilles is notable for its petrologic diversity, comprising wehrlites, hornblendites, clinopyroxenites and a variety of gabbros. Whilst the textures testify to a relatively simple crystallisation history, the impressive array of assemblages from this island arc volcano reflects a wide range of magmatic storage conditions. The ultimate goal of this project is to replicate the various cumulate assemblages by conducting equilibrium experiments on parental basalts under a range of volatile ( $H_2O$ ,  $CO_2$ ) contents, temperatures, pressures and  $fO_2$ , and so elucidate the conditions of magma storage and differentiation beneath Grenada. Experiments have focussed on determining the topology of the parental basalt liquidus and the near-liquidus phase relations. Experiments were carried out in the pressure range 0.0001-1.7 GPa using 1 atm furnace, TZM pressure vessel and piston cylinder apparatus employing a double capsule technique<sup>1</sup>; run products were ubiquitously glassy and contained a high melt fraction ( $f > 0.60$ ).

## Purpose of SIMS analysis

The purpose of SIMS analysis in this project was to accurately determine the dissolved volatile contents in experimental run products. This was a continuation of work carried out in 2011, where the first half of the experimental series was analysed. Equilibrium experiments were carried out using three different water contents, so it was important to verify that these conditions had been maintained throughout experimental runs. In addition, other volatiles species such as  $CO_2$  (as carbon) and boron have the potential to diffuse into the noble metal capsules and can influence phase relations. If they were present, it was essential to quantify the amount present and modify the design of future experiments.

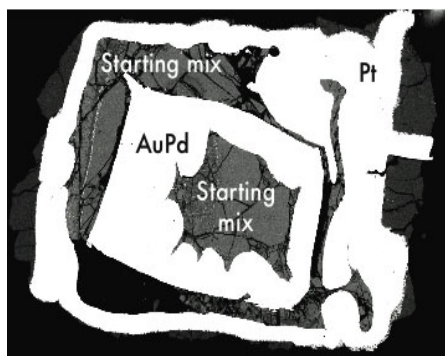


**Figure 1. (a)** BSE image of a piston cylinder run product comprising inner and outer capsule. White areas are noble metal, greyscale gives position of glass and crystals. Horizontal scale = 6mm.

## Results (incorporating data from 2011)

The inner and outer capsule glasses of 37 experimental run products were analysed for  $H_2O$ ,  $CO_2$  and B. Starting materials contained three different water contents (nominally anhydrous, 3.0 wt % and  $H_2O$ -saturated) and were initially free of  $CO_2$  and B. The double capsule design was proven to be effective at preventing B flux into the inner capsule regardless of whether boron nitride was included in the assembly design: the maximum outer capsule B content was 2640ppm but did not exceed 200ppm in inner capsule glasses. However, the same was not found to hold for  $CO_2$ . The piston cylinder experiments contained  $<1.38$  wt%  $CO_2$  in the inner capsule, showing that carbon ingress was a significant problem. In contrast the TZM glasses contained only  $<365$ ppm  $CO_2$ . This information allowed us to isolate the source of carbon to be the graphite furnace and modify the design of future experiments.  $H_2O$  content of the  $H_2O$ -undersaturated experiments ranged between 1.9 – 4.3 wt % with a mean value of 3.1 wt %; anhydrous experiments yielded glasses with  $<0.3$  wt %  $H_2O$ . That the appropriate  $H_2O$  content was maintained throughout the duration of the experimental run facilitated

the quantification of the effect of pressure and temperature on the topology of the basalt liquidus and delineation of the near-liquidus phase relations.

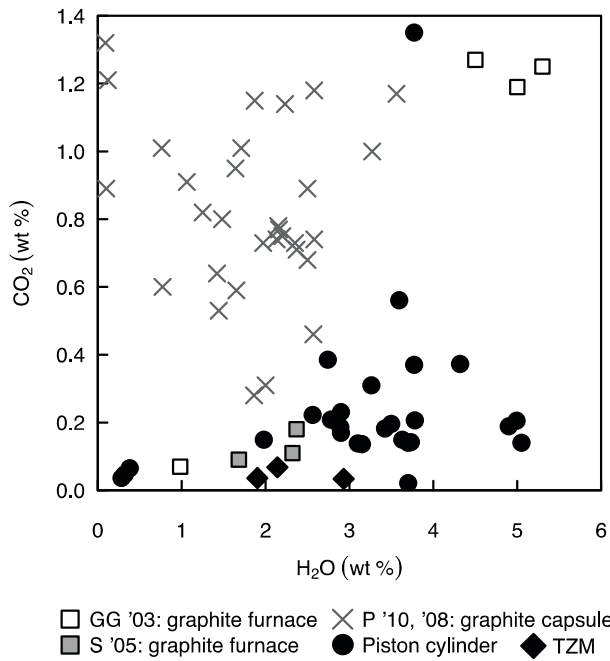


**Figure 2. (a)** Volatile contents of experimental glasses from nominally CO<sub>2</sub>-free systems. Black symbols depict CO<sub>2</sub> and H<sub>2</sub>O of glasses from piston cylinder and TZM experiments in this study as measured by SIMS. Literature data is from other piston cylinder experiments (P '10, '08 = Pilet et al. (2008), Pilet et al. (2010); S '05 = Sisson (2005); GG '03 = Gaetani et al. (2003)). There is a weak positive correlation between the two volatile species, suggestive of a coupled diffusion mechanism. CO<sub>2</sub> is elevated when graphite capsules are used in addition to a graphite furnace.

## References

- [1] LJ Hall et al. (2004) Mineral. Mag, **68**, 75-81.

# Superdeep diamonds preserve record of ancient carbon subduction

A. Thomson<sup>1</sup>, M. Walter<sup>1</sup>, S. Kohn<sup>1</sup>, G. Bulanova<sup>1</sup>, C. Smith<sup>1</sup> & D. Araujo<sup>2</sup>

<sup>1</sup>School of Earth Sciences, University of Bristol, Bristol, BS8 1RJ, UK

<sup>2</sup>Instituto de Geociências, Universidade de Brasília, CEP 70910-900 Brasília, DF, Brazil

## Introduction

The Juina region of Brazil is home to a field of Cretaceous alkaline kimberlite deposits that erupted into the Rio Negro-Juruena Mobile Belt, on the southwest edge of the Amazon Craton. One of the region's idiosyncrasies is its unexplained ability to significantly oversample diamonds originating at sub-lithospheric depths in the earth compared with most other parts of the world where diamonds originate in the lithospheric mantle [1]. These sub-lithospheric (or 'superdeep') diamonds can be recognised using mineral inclusions trapped within the diamonds through association with experimentally determined phase stabilities. Such samples are of great significance to mantle petrologists as they provide direct information about the chemical and physical processes that are occurring in the deepest recesses of our planet. Alongside analysis of the mineral inclusions, study of the diamond hosts can provide significant insight into the environment and manner in which they formed.

In this study we measured the carbon isotopic composition of several superdeep diamonds from the Juina region of Brazil that contain previously studied mineral inclusions indicating growth in the sub-lithospheric mantle from subducted protoliths. By studying both the carbon isotope distribution of multiple diamonds from individual kimberlite pipes and intra-diamond isotopic variability, the source of carbon for diamond growth and the growth medium of the diamonds can be identified.

Superdeep diamonds from the Juina-5 and Collier-4 kimberlite pipes were analysed for  $\delta^{13}\text{C}$  composition using multiple 15-20 $\mu\text{m}$  sized spot analyses in each diamond. The location of analyses was referenced using cathodoluminescence (CL) images of the stones. This allowed inspection of any core to rim variability. Uncertainty in measurements was estimated using regularly repeated standard measurements giving an error of  $\pm 0.21\%$  PDB for all four days of analysis.

## Intra-diamond Heterogeneity

We observe that individual diamonds display significant heterogeneity in their isotopic composition, with shifts of up to 15‰ across diamonds of 1-2mm in size. Previous work has shown that the direction of isotopic evolution during diamond growth depends on the oxidation state of the fluid medium that is precipitating diamond [2]. If the diamond becomes isotopically heavier from core to rim it can be judged to have fractionated from oxidising species (e.g.  $\text{CO}_2$  or carbonate melt), whereas if the opposite is true growth occurred from a reducing fluid (e.g.  $\text{CH}_4$ ). In this study diamonds evolving isotopically in both directions are observed (fig. 1). This can be attributed to diamond growth from a mixture of carbon species. However it is also observed that where there are abrupt changes in CL response there is an equivalent response in  $\delta^{13}\text{C}$ . This might suggest multiple growth events from distinct fluids at different periods in a stone's history.

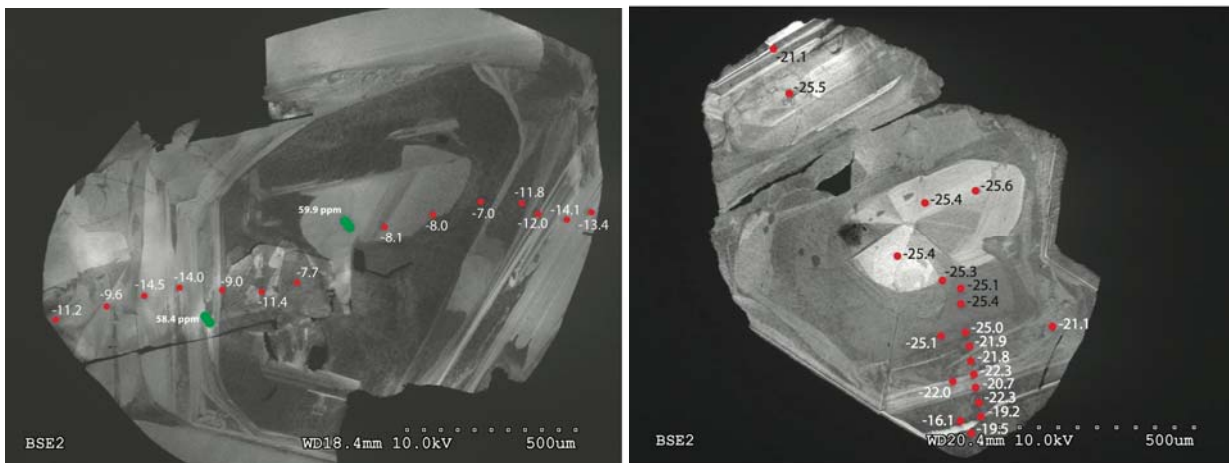


**Figure 1.** Grey-scale CL images for two diamonds with analysed carbon isotopic compositions marked with annotated red dots. (a) Diamond RC1-9B from the Collier-4 kimberlite showing isotopic composition becoming lighter from core to rim. (b) Diamond Ju5-115 from Juina-5 kimberlite pipe that displays opposite trend in  $\delta^{13}\text{C}$ .

## Carbon Isotope Distributions

Thirty-five Juina-5 and ten Collier-4 diamonds were analysed and results combined with previous analyses [3], allowing definition of the  $\delta^{13}\text{C}$  distributions of the two kimberlite pipes and comparison with the global distribution [4] (figure 2). The global distribution is heavily centred on  $-5\text{‰}$ , a feature attributed to the mantle carbon source being sampled. It is clear from figure 2 that the distributions of the two diamond suites are significantly different from the global distribution, with Juina-5 especially sampling a light carbon component centred on  $-25\text{‰}$ . The Collier-4 distribution is so far based upon fewer analyses than that of Juina-5 and shows a spread distribution across a range  $-25$  to  $-5\text{‰}$  with a mode around  $-9\text{‰}$ , but still with few data reaching mantle-like values.

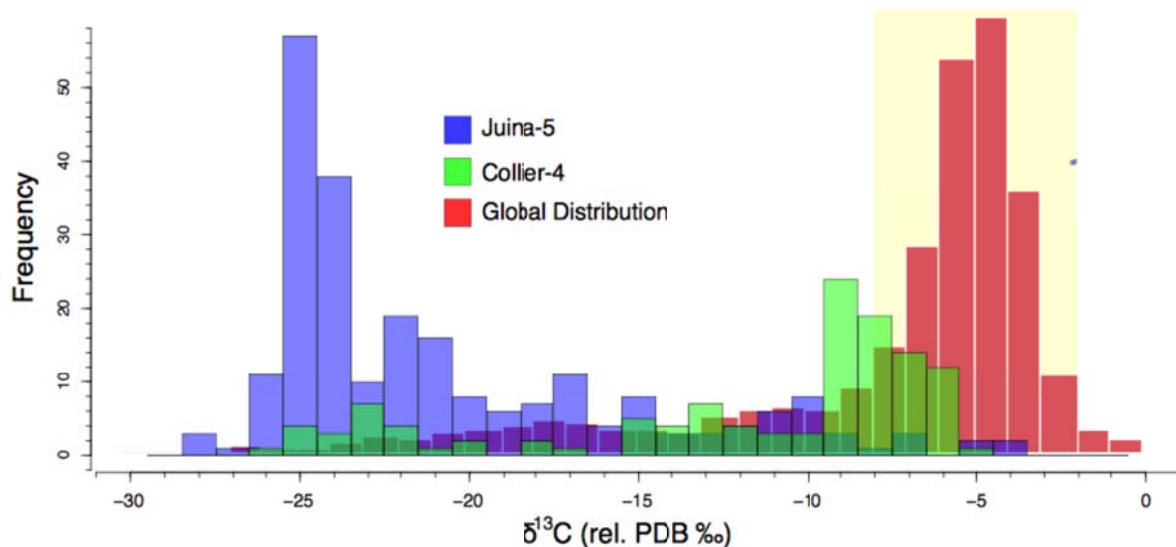


**Figure 2.** Histograms showing the carbon isotopic distributions of diamonds from Juina-5 (this study) and Collier-4 (this study and [3]) compared with the global distribution [4]. Mantle carbon is thought to lie at  $-5\text{‰}$ .

## Subducted Light Carbon Source

The cause of isotopically light diamonds is one that is still rather controversial. There are currently three main theories for its origin: (1) sampling of primordial heterogeneity; (2) isotopic fractionation during open-system diamond growth; (3) sampling of subducted light carbon source. In recent years (1) has essentially been ruled out as a possible cause of light carbon due to the constant mantle mixing by subduction and convection over time. In this study we can also discard (2), as it isn't possible to create a reservoir of  $-25\text{‰}$  carbon by fractionation of mantle material [5] that could produce these diamonds.

The distribution of carbon in the subducting oceanic crust has been determined by study of ODP drill cores from several locations across the sea floor. It has been discovered that the carbon entering the subduction zone as part of a slab exists as a bimodal distribution of carbonate ( $\delta^{13}\text{C} \sim 0\text{‰}$ ) from seawater interaction and organic carbon ( $\delta^{13}\text{C} \sim -25\text{‰}$ ) from hydrothermal alteration [6]. The bulk input has a composition of  $-5\text{‰}$  determined by mass balance. We suggest that the superdeep diamonds of the Juina region must be preferentially sampling the isotopically light organic carbon component that is part of the subducting assemblage. In this situation it can be concluded that these superdeep diamonds each preserve a record of the entire tectonic cycle, from crust formation at the mid-ocean ridge to subduction into the sub-lithospheric mantle and return to the earth's surface in alkaline volcanism.

## References

- [1] Harte, B. (2010). *Mineralogical Magazine* **74**, 189-215.
- [2] Deines (1980). *Geochimica et Cosmochimica Acta* **44**, 943-961.
- [3] Bulanova *et al.* (2010). *Contributions to Mineralogy and Petrology* **160**, 489-510.
- [4] Cartigny (2005). *Elements* **1**, 79-84.
- [5] Smart *et al.* (2011). *Geochimica et Cosmochimica Acta* **75**, 6027-6047.
- [6] Shilobreeva *et al.* (2011). *Geochimica et Cosmochimica Acta* **75**, 2237-2255.

# Quantifying the dynamics of calcite cement growth with oil emplacement and the evolution of pore chemistry

D.Thorpe<sup>1</sup> & R. Wood<sup>1</sup>

<sup>1</sup>School of GeoSciences, University of Edinburgh, Edinburgh EH9 3JW, UK

## Abstract

The pore space evolution of calcite reservoirs can be understood by analysing the  $\delta^{18}\text{O}_{\text{VPDB}}$  of calcite cements. This approach has shown that the water leg of the field has been occluded by early burial cement phases and was fully occluded before late burial cementation occurred. Porosity was preserved in the oil leg due to oil charge, which retarded cementation, whereas in the water leg full effective porosity occlusion was observed. This method will make it possible to better understand the porosity evolution of carbonate reservoirs, from this a new porosity-depth curve can be produced which will then be incorporated into basin models.

## Introduction

The elemental chemistry of calcite is affected by many factors and is difficult to interpret, but the controls of stable isotope composition are better understood. Calcite precipitated during burial will experience rising temperatures with increasing depth, leading to progressively lower  $\delta^{18}\text{O}_{\text{VPDB}}$  values. The  $^{18}\text{O}$  evolution of formation waters is variable but commonly becomes greater due to calcite dissolution/re-precipitation reactions. Although these effects may cancel one another out, many analyzed late calcites show decreasing  $^{18}\text{O}_{\text{VPDB}}$  values related to increasing temperature during burial [1]. In this analysis the  $^{18}\text{O}_{\text{VPDB}}$  concentration of calcite cements has been used to help understand the temperature at which a calcite CL zone precipitated, helping us to discern pore space evolution.

## Results

Cathode Luminescence (CL) of calcite cements reveals that 11 zones are present in the oil leg and transition zone, and 6 CL zones in the water leg. Results show that cement groups also have a distinctive isotopic signature: early marine cements range from -1 to -4.5 ‰; early burial cements from -4.5 to -8.0 ‰ and late burial cements from -8.0 to -13.5 ‰.

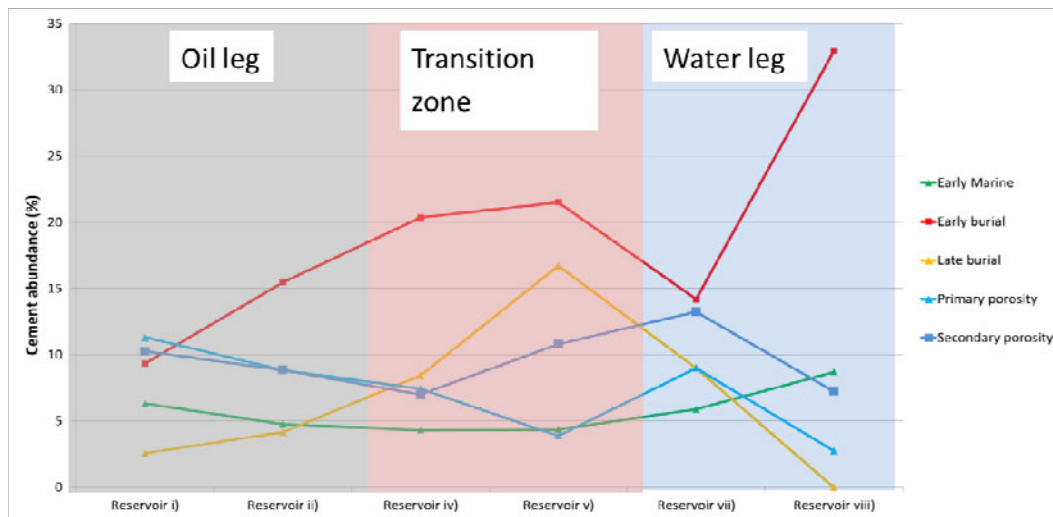


Figure 1. Distribution of cements in relation to stratigraphic position.

The volume of cement for each of these groups was quantified in 51 thin sections by image analysis and point counting techniques within the water leg, transition zone, and oil leg (Fig. 1). The volumes of cement in the upper reservoirs are lower than in the lower reservoirs and water leg. Early burial cements fully occlude the effective pore space (mainly intergranular and intercrystalline + vuggy porosity) in the water leg (viii), and there is a progressive decrease in late stage burial cement volume from the transition zone reservoirs (iv and v) to the oil leg reservoirs (i and ii). These cement volumes

are independent of primary porosity (as indicated by inter-granular porosity) and secondary porosity (vuggy and inter-crystalline porosity) (Fig. 1). This suggests that oil charge greatly retards cementation in the oil reservoirs but does not cause cementation to cease, leading to a progressive increase in late stage burial cement volume down the structure.

The field is located on a passive margin and so during burial the field will experience rising temperatures, leading to progressively lower  $\delta^{18}\text{O}_{\text{VPDB}}$  concentrations in the younger CL zones; this is observed from CL zone 1 to 10 (Fig. 2). A more positive  $\delta^{18}\text{O}_{\text{VPDB}}$  signature is observed in CL zone 11, suggesting that the zone formed at lower temperatures and is likely related to the uplift of the field anticlinal structure.

The water leg has a more negative  $\delta^{18}\text{O}_{\text{VPDB}}$  concentration than the same CL zone in the oil leg (Fig. 2). This is related to the depth difference between the top and bottom of the structure and the corresponding increase in temperature.

Cement growth in the water leg ceased before the oil leg and transition zone (Fig. 2). The effective porosity in the water leg was fully occluded by CL zone 6 and so cementation ceased, whereas in the oil leg cementation continued. Oil charge likely caused the preservation of porosity in the oil leg so allowing for continued cementation.

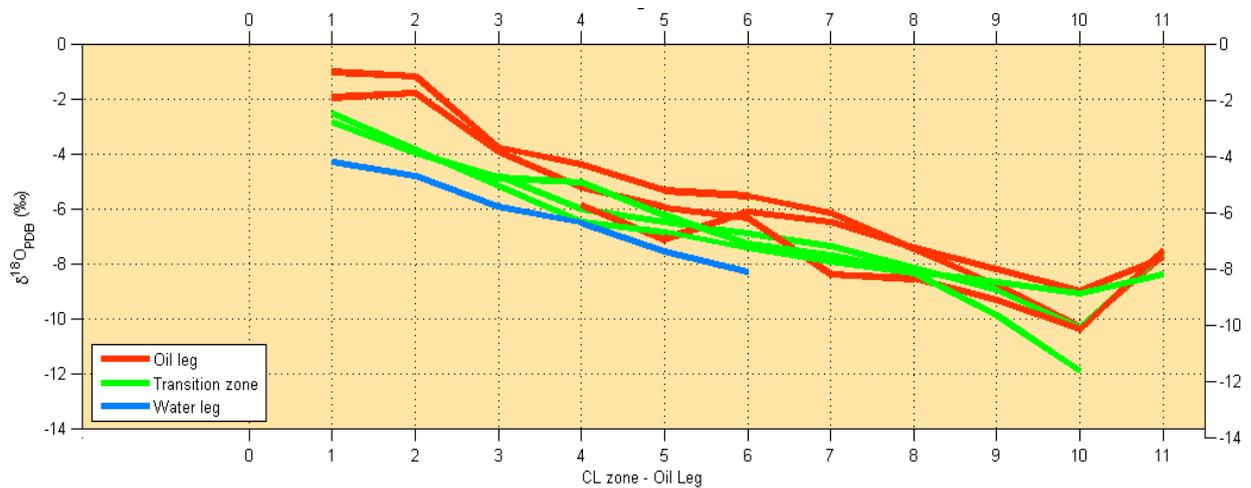


**Figure 2.** CL zone  $\delta^{18}\text{O}_{\text{VPDB}}$  signature in the oil (red lines), transition (green lines) and water legs (red line) of the field

## References

[1] Cox, P.A., Wood, R., Dickson, J.A.D et al, 2010, Dynamics of cementation in response to oil charge: Evidence from a Cretaceous carbonate field, U.A.E. *Sedimentary Geology*, 228: 246-254

# Constraining conodont $\delta^{18}\text{O}$ for Palaeozoic marine palaeothermometry

J.R. Wheeley<sup>1</sup>, M.P. Smith<sup>2</sup> & I. Boomer<sup>1</sup>

<sup>1</sup>School of Geography, Earth and Environmental Sciences, University of Birmingham, Birmingham B15 2TT, UK

<sup>2</sup>Oxford University Museum of Natural History, Parks Road, Oxford OX1 3PW, UK

## Introduction

Traditionally, geological studies of past seawater temperature variability have had to use bulk samples of conodont elements ('teeth') processed through high temperature reduction of silver phosphate from conodont apatite. Recent advances have shown the value of analyzing single conodont elements (by ion microprobe), but there are still occasions when bulk analyses must be performed. It is therefore essential that isotopic variability both within and between conodont taxa is understood if the results of these mixed samples are to be meaningfully interpreted. In addition, the analysis of individual conodont elements offers the potential simultaneously to assess the environmental preferences of individual conodont species, to test models of conodont ecology, and to examine the feasibility of using conodonts as water mass indicators in Palaeozoic oceans.

Although researchers utilizing conodont oxygen isotopes for sea water temperature reconstruction through high temperature reduction of silver phosphate ( $\text{Ag}_3\text{PO}_4$ ) are moving towards bulk samples composed of single species [e.g. 1], there are still occasions where mixed species samples are required to obtain enough material for analyses [e.g. 2, 3]. The effects of such mixing are believed by some to have statistically insignificant impact on results [e.g. 4], but there have been relatively few tests of this assertion and, in consequence, the oxygen isotope range within conodont faunas is poorly understood. Thermally stratified water columns in Ordovician marine settings would be expected to lead to pelagic and nekto-benthic taxa having apatitic elements with different isotopic values that reflect variation in the physical properties of individual water masses and decreasing water temperature with depth. However, when assessing stratigraphic variability in the temperature of ancient oceans using bulk analyses, variations in the abundance of species with differing bathymetric ecology and thus differing isotopic compositions may lead to the misinterpretation of relative cooling or warming trends. This has been tested in this study by analyzing conodont taxa within a single conodont sample in order to establish the impact of species variability due to ecology on faunal isotopic range and variability. The sample chosen is a well-preserved limestone bed from the Floian (Lower Ordovician) of Newfoundland, Canada (Figure 1), from a rarely preserved shelf-edge setting that contains both pelagic and nekto-benthic conodonts of significantly different hypothesised bathymetries [5].

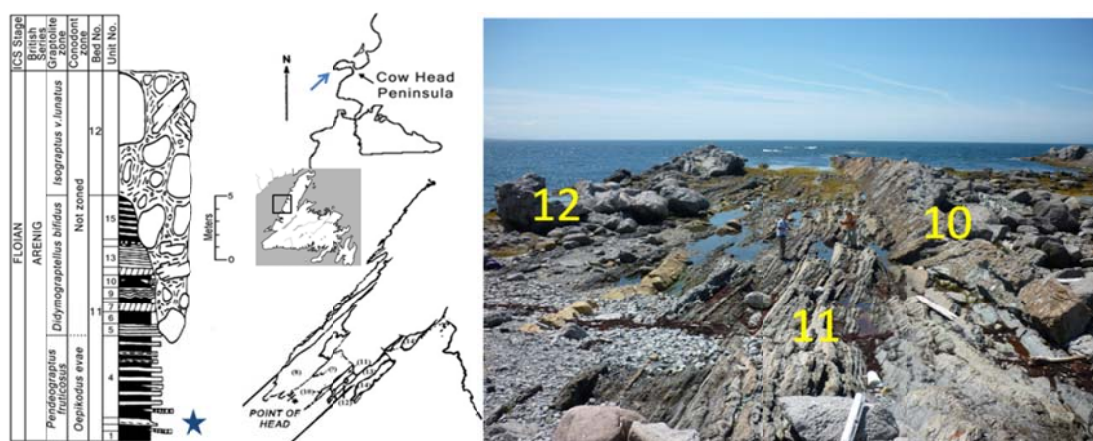


**Figure 1.** Location of conodont sample used in the study. Left: maps and sedimentary log of the Point of Head Section, Cow Head Peninsula, western Newfoundland – star marks the sampling horizon (maps and section adapted from [6]). Right: field photograph of sampling locality (lowest bed 11).

## 2012 analyses

Analyses of conodonts were undertaken on the Cameca 1270 in August 2012 using our protocols for the ion microprobe analysis of conodonts [7]. Building on our 2011 analyses, we have investigated multiple conodont element types from individual species and have also expanded the number of species included in the study from 5 to 9 (Figure 2). The inter-species variability of 2‰ (based on mean values for taxa) in the Ordovician sample is comparable with the magnitude reported between some species of a mid-Ordovician (Darriwilian) sample analysed previously [7]. One interpretation is that this isotopic offset (between *Bergstroemognathus extensus* and *Drepanodus planus*) reflects the

different water temperature that these conodonts inhabited in life. Similarly, the intraspecific range in  $\delta^{18}\text{O}$  (up to 2.5‰ in *Oepikodus evae*) could result either from a life habit that spanned a greater extent of the water column, and thus a broader temperature gradient, than taxa with a narrower intraspecific range of values (e.g. *B. extensus*). Alternatively, it may represent an issue concerning differential taphonomy and diagenesis or variable analyses from different conodont hard tissues.

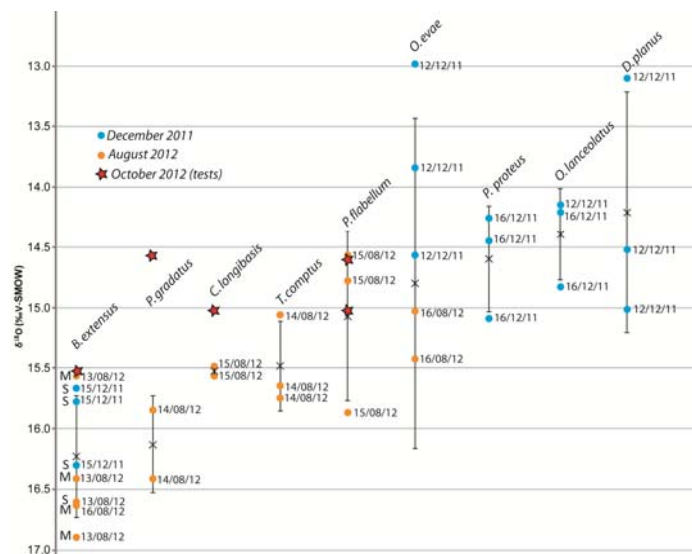


**Figure 2.** Intra- and inter-species variability in conodont oxygen isotopes from our 2011 and 2012 analyses along with some ‘tests’. ‘S’ and ‘M’ adjacent to *Bergstroemognathus extensus* label different element types.

Modelling of our 2011 and 2012 results using weighted averages to assess the impact of variation in mixed species samples through a hypothetical stratigraphy demonstrates that varying proportions of different taxa in bulk samples could lead to variation in mean average values and thus potential misinterpretation of cooling and warming (Figure 3).

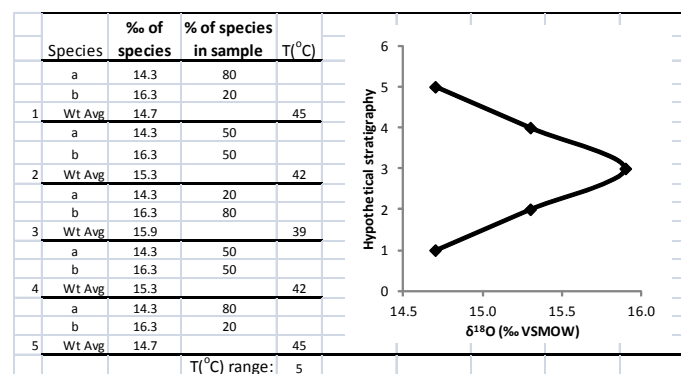


**Figure 3.** Artificial  $\delta^{18}\text{O}$  positive excursion generated through five samples composed of variable percentages of two taxa (a and b) with the 2‰ inter-species variability recognised in our study. Temperatures calculated using phosphate-temperature equation [8]. Note the temperature range generated through this process.

### Future work

Following the two rounds of assessing proofs of concept (IMF333/0508 & IMF414/1010), our results demonstrate that the ion microprobe determination of oxygen isotopes in conodont elements is a robust means of determining water temperature in Palaeozoic oceans, provided that strict protocols are observed [7]. In consequence, we are now in a position to utilise the technique to test for oceanic cooling and warming episodes and to begin, for the first time in Early Palaeozoic oceans, to disentangle water mass configurations and aquafacies distributions in epeiric seas.

### References

- [1] Rosenau *et al.* (2012), *P3*, **315-316**, 172-180. [2] Joachimski *et al.* (2012), *Geology*, **40**, 195-198. [3] Bo Chen *et al.* (2011), *P3*, **311**, 145-153. [4] Elrick *et al.* (in press) *Geology* [5] Ji & Barnes (1994), *J. Paleont.*, **68**, 1368-1383. [6] Won and Iams (in press), *Palaeoworld*. [7] Wheeley *et al.* (2012) *J. Geol. Soc. Lond.*, **169**, 239-250. [8] Kolodny *et al.* (1983) *EPSL*, **64**, 398-404.